Theses and Dissertations | 1. Thesis and Dissertation Collection, all items

2007-03

Fine pointing of military spacecraft

Sands, Timothy A.

Monterey California. Naval Postgraduate School

http://hdl.handle.net/10945/10261

NAVAL POSTGRADUATE SCHOOL

MONTEREY, CALIFORNIA

DISSERTATION

FINE POINTING OF MILITARY SPACECRAFT

by

Timothy A. Sands

March 2007

Dissertation Supervisor/Advisor: Brij N. Agrawal

Approved for public release, distribution is unlimited.

THIS PAGE INTENTIONALLY LEFT BLANK

REPORT DOCUMENTATION PAGE		*Form Approved OMB No. 0704-0188*
Public reporting burden for this collection of information is estimated to average 1 hour per response, including the time for reviewing instruction, searching existing data sources, gathering and maintaining the data needed, and completing and reviewing the collection of information. Send comments regarding this burden estimate or any other aspect of this collection of information, including suggestions for reducing this burden, to Washington headquarters Services, Directorate for Information Operations and Reports, 1215 Jefferson Davis Highway, Suite 1204, Arlington, VA 22202-4302, and to the Office of Management and Budget, Paperwork Reduction Project (0704-0188) Washington DC 20503.		

1. AGENCY USE ONLY *(Leave blank)*	2. REPORT DATE March 2007	3. REPORT TYPE AND DATES COVERED Dissertation	
4. TITLE AND SUBTITLE: Fine Pointing of Military Spacecraft		5. FUNDING NUMBERS	
6. AUTHOR: Timothy A. Sands			

7. PERFORMING ORGANIZATION NAME(S) AND ADDRESS(ES)
  Naval Postgraduate School
  Monterey, CA 93943-5000
		8. PERFORMING ORGANIZATION REPORT NUMBER	

9. SPONSORING / MONITORING AGENCY NAME(S) AND ADDRESS(ES) N/A		10. SPONSORING / MONITORING AGENCY REPORT NUMBER	
11. SUPPLEMENTARY NOTES The views expressed in this thesis are those of the author and do not reflect the official policy or position of the Department of Defense or the U.S. Government.			
12a. DISTRIBUTION / AVAILABILITY STATEMENT Approved for public release, distribution is unlimited.		12b. DISTRIBUTION CODE	

13. ABSTRACT

   In 1923, Herman Oberth, considered by some to be "the father of it all" for spaceflight, wrote a book called "Die Rakete zu den Planeträumen" (i.e., "Dreams of Planets") inspiring today's modern spaceflight. Amongst his suggestions was placing a telescope in space, so astronomical observations may be made without atmospheric distortion. Nearly a century later, the Hubble Space telescope is imaging distant stars with high accuracy. If Hubble were placed on the ground of the West Coast of the United States, it would able to target a small coin placed on the Lincoln memorial on the East Coast of the United States. This startling accuracy has become useful for military spacecraft missions as well even though the mission is much more challenging. Military spacecraft perform aggressive slew maneuvers to acquire targets, but the actuators are complicated by singularities that can often lead to loss of attitude control during aggressive maneuvers. After acquiring the target, the spacecraft must rapidly settle and track the target as the spacecraft races by overhead.

   This dissertation addresses these challenges by introducing a new optimized geometry for installation of the spacecraft actuators to minimize the impact of singularities. Methods are discussed to orient the direction of maximum slew capability in a desired direction. In addition to the optimal geometry, a new algorithm is presented that reduces those remaining singularities that could lead to loss of attitude control. A newly developed algorithm is proven to *fly through* the singularities without losing attitude control. The advancements introduced here increase aggressive maneuver performance aiding military spacecraft rapidly acquire earthly targets.

   After acquiring the target, several new, very simple adaptive control algorithms are introduced that adjust the control strategy based on tracking errors. If the spacecraft has trouble tracking a target, the control is adjusted to eliminate the tracking error. Using simplified techniques, target tracking accuracy is increased compared to current spacecraft control methods. While many promising, advanced techniques look good on paper, real-world factors like noisy signals and disturbances are often confounding. Most importantly, the claims made here are proven experimentally on a free-floating spacecraft simulator.

14. SUBJECT TERMS: Spacecraft attitude control, control moment gyroscope, singularity minimization, singularity reduction, singularity penetration, nonlinear adaptive control, acquisitions tracking and fine pointing			15. NUMBER OF PAGES 155
			16. PRICE CODE

17. SECURITY CLASSIFICATION OF REPORT
    Unclassified
	18. SECURITY CLASSIFICATION OF THIS PAGE
	    Unclassified
		19. SECURITY CLASSIFICATION OF ABSTRACT
		    Unclassified
			20. LIMITATION OF ABSTRACT
			    UL

NSN 7540-01-280-5500

Standard Form 298 (Rev. 2-89)
Prescribed by ANSI Std. 239-18

i

THIS PAGE INTENTIONALLY LEFT BLANK

FINE POINTING OF MILITARY SPACECRAFT

Timothy A. Sands
Major, United States Air Force
B.S., North Carolina State University, 1992
Certificate, University of California, Los Angeles, 1996
M.S., University of North Dakota, 2000
M.Eng., University of Colorado, 2006

Submitted in partial fulfillment of the
requirements for the degree of

DOCTOR OF PHILOSOPHY IN ASTRONAUTICAL ENGINEERING

from the

NAVAL POSTGRADUATE SCHOOL
March 2007

Author: _____
Timothy A. Sands

Approved by:

_____	_____
Brij N. Agrawal	Young S. Shin
Distinguished Professor MAE	Distinguished Professor MAE
Dissertation Supervisor	
_____	_____
Isaac Kaminer	Roberto Cristi
Professor of MAE	Professor of ECE
_____	
Marcello Romano	
Professor of MAE	

Approved by: _____
Anthony J. Healey, Chair, Department of MAE

Approved by: _____
Julie Filizetti, Associate Provost for Academic Affairs

iii

THIS PAGE INTENTIONALLY LEFT BLANK

ABSTRACT

In 1923, Herman Oberth, considered by some to be "the father of it all" for spaceflight, wrote a book called *"Die Rakete zu den Planeträumen"* (i.e., "Dreams of Planets") inspiring today's modern spaceflight. Amongst his suggestions was placing a telescope in space, so astronomical observations may be made without atmospheric distortion. Nearly a century later, the Hubble Space telescope is imaging distant stars with high accuracy. If Hubble were placed on the ground of the West Coast of the United States, it would able to target a small coin placed on the Lincoln memorial on the East Coast of the United States. This startling accuracy has become useful for military spacecraft missions as well even though the mission is much more challenging. Military spacecraft perform aggressive slew maneuvers to acquire targets, but the actuators are complicated by singularities that can often lead to loss of attitude control during aggressive maneuvers. After acquiring the target, the spacecraft must rapidly settle and track the target as the spacecraft races by overhead.

This dissertation addresses these challenges by introducing a new optimized geometry for installation of the spacecraft actuators to minimize the impact of singularities. Methods are discussed to orient the direction of maximum slew capability in a desired direction. In addition to the optimal geometry, a new algorithm is presented that reduces those remaining singularities that could lead to loss of attitude control. A newly developed algorithm is proven to *fly through* the singularities without losing attitude control. The advancements introduced here increase aggressive maneuver performance aiding military spacecraft rapidly acquire earthly targets.

After acquiring the target, several new, very simple adaptive control algorithms are introduced that adjust the control strategy based on tracking errors. If the spacecraft has trouble tracking a target, the control is adjusted to eliminate the tracking error. Using simplified techniques, target tracking accuracy is increased compared to current spacecraft control methods. While many promising, advanced techniques look good on paper, real-world factors like noisy signals and disturbances are often confounding. Most importantly, the claims made here are *proven* experimentally on a free-floating spacecraft simulator.

THIS PAGE INTENTIONALLY LEFT BLANK

TABLE OF CONTENTS

LIST OF FIGURES

LIST OF TABLES

THIS PAGE INTENTIONALLY LEFT BLANK

ACKNOWLEDGMENTS

Any success this document achieves is contributable more to those around me than to myself. Distinguished Professor Brij Agrawal has created such a world class facility of experimental laboratories, the highest quality research is assured. It cannot be overstated that my ideas were simply that…thoughts. With some analytical rigor, ideas may be presented as innovations, but it is much harder to argue with experimental results. Professor Agrawal's extensive industry experience was an invaluable tool that guided my efforts, while his goal-oriented attitude both assured me of graduation and simultaneously drove me to achieve the high graduation standard for research that contributes to the field of astronautical engineering. Smooth operation of his Spacecraft Research and Design Center (SRDC) labs is a result of his phalanx of high quality professors and engineers. Professor Roberto Cristi from the Department of Electrical and Computer Engineering adds a significant analytical skill to the SRDC. I am extremely grateful for his guidance and expertise in adaptive control and nonlinear systems stability. Dr. Kim, Jae-Jun fulfills the role of NRC Postdoc on the SRDC, and the operational lab equipment is attributable to his tireless efforts. Words cannot express how much his hard work meant to the eventual quality of this dissertation with the incorporation of experimental verification of suggested advanced concepts. In addition, Dr. Kim was a "sounding board" for my thoughts, and I appreciate his patience and diligence. Additional thanks and appreciation are extended to Professional Engineer Mike Doherty and Staff Engineer Matt Goldman for their efforts in the SRDC. Professor Marcello Romano served as a role model having recently completed his postdoc time at the Naval Postgraduate School establishing the dynamics equations of the experimental spacecraft simulator and initiating investigation of control moment gyroscope control. Perhaps unbeknownst to him, I found his advice invaluable. The recency of his research and his understanding of the likely pitfalls kept him one step ahead of me resulting in perfectly timely advice.

Distinguished Professor Young S. Shin reminded me that engineering is no different than any aspect of life in that your heart must be in it to achieve success. I appreciate his calm demeanor and kind etiquette even when asking the tough questions.

My wife Celine is the woman behind the man…the rock. Her steadfast devotion to my success has been invaluable in innumerable ways. She even attended my dissertation defense and rode the emotional rollercoaster with me. With the preface that school can often be challenging, the strongest statement may be made. In order to free my mind regarding her boredom while I spent long nights studying, she enrolled in school herself at the Monterey Peninsula college. Taking as many as 5 classes simultaneously, she walked a mile in my shoes spending many late nights studying herself. At no instance did I feel pressured to neglect schoolwork. On the contrary, she often asked for privacy to accomplish her challenging academic tasks. Her labors landed her on the Dean's List with near-perfect grades culminating in an Associates Degree *with honors*. She has my devotion, my thanks, and my congratulations. I am very proud of her.

I. INTRODUCTION

A. MOTIVATION

Military satellites face unique challenges performing their mission. The civilian Hubble Space Telescope[1] needs to point extremely accurately (within an accuracy of 0.007 arc-seconds = 0.034 *micro*-radians or 1.94 *micro*-degrees) to take pictures of distance objects. It achieves this level of accuracy by staring fixed in inertial space controlled by four reaction wheels. Large slews between targeted objects are performed by reaction wheels over as much as much as 9-20 minutes with considerable settling time permitted for target tracking [2]. Reaction wheels are low torque devices that provide torque by absorbing momentum by increasing/decreasing wheel rotation speed. Military spacecraft on the other hand may slew from one target to another several times in one orbital pass and cannot take 20 minutes to accomplish maneuvers. Military satellites must reconnoiter multiple points in a given orbital pass (as little as 10 minutes). Minimization of target acquisitions time is a critical requirement.

While current and future mission requirements are driving Hubble-like pointing accuracy, military operational requirements demand large angle, rapid slew maneuvers as quickly as possible and also require quick settling with minimal target tracking errors. Consider a military spacecraft simply taking pictures. After achieving a rapid target acquisition slew, blurry images will result if tracking errors are large.
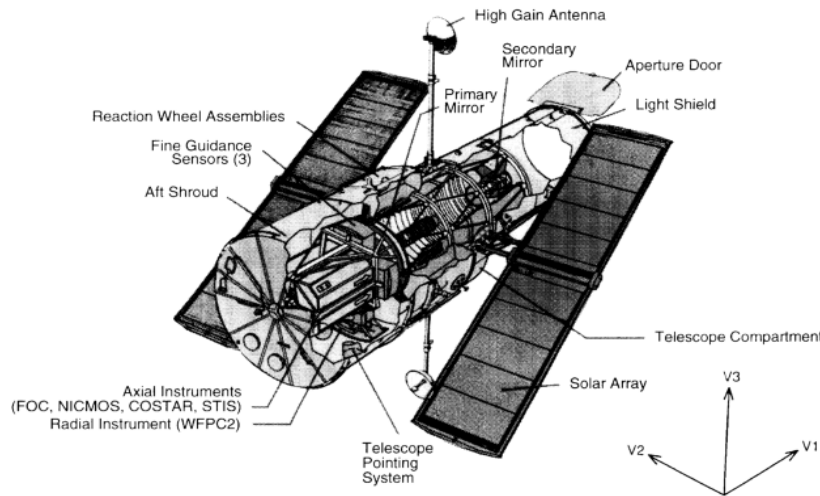
Figure 1 Hubble Space Telescope [2].

1

The military spacecraft mission of rapidly acquiring and accurately tracking a terrestrial or space-based target is often referred to as *acquisitions, tracking and pointing* (ATP). Civilian spacecraft are not typically designed for such missions, but military spacecraft often must perform these missions despite their shared design heritage. Even considering a rigid spacecraft, rapid maneuvers with quick settling time and fine target tracking are quite challenging. Systematically consider rapid slew maneuvers as one challenge and target tracking as a second challenge.

1.   Fast Target Acquisitions Maneuvers

The rapid slew maneuver often drives spacecraft to utilize high-torque actuators like thrusters and control moment gyroscopes (CMGs). While thrusters have finite fuel that is easily depleted, CMGs are momentum exchange devices that trade momentum back and forth with the spacecraft without exhaustion. Unlike the reaction wheel that spins up/down to deliver relatively low torque, the wheel spins in the CMG at a constant rate creating a large momentum vector. Momentum changes result when the spinning CMG wheel is gimbaled (single or double gimbal) generating rapid spacecraft reaction torques. Since angular momentum of the entire spacecraft system is conserved, changes in CMG momentum must result in corresponding changes in spacecraft momentum to maintain system equilibrium.

Despite desirable traits, CMGs suffer from mathematical singularities that severely limit the achievable torque with typical control algorithms risking loss of attitude control. Singularities may be physically defined as the inability to generate a desired, arbitrary torque (the *dilemma*). The mission demands inexhaustible, repeated rapid maneuvers in minimum time. This dictates the use of control moment gyroscopes, but singularities can result in complete loss of attitude control. While a minimum of three single-gimbaled CMGs (SGCMGs) are required for three-axis control, spacecraft designers currently use more than three SGCMGs to afford themselves extra degrees of freedom to implement singularity avoidance schemes in hopes of avoiding lost attitude control.

Additionally, consider that CMG rotor wheels must spin at all times, thus failures are very common. The International Space Station uses a four CMG array and

experienced its first CMG failure on June 8, 2002, after about 1.5 years of operation[3]. Despite this failure, the ISS must still insure safety during normal operations, Space Shuttle rendezvous, and repair operations.

With relatively sparse research using only three SGCMGs, post-failure attitude control with CMGs is very challenging. Most commonly, the singularity-free momentum space is determined for the given geometric installation of the CMGs. Momentum management dominates attitude control requiring engineers to keep maneuvers below the singularity-free threshold for safety's sake. Military missions must be prepared to operate with three SGCMGs despite the sparseness of research in the literature for three CMGs.

With this backdrop, this thesis entails current research to optimize the three CMG array to give maximum momentum for minimum time slew maneuvers. Furthermore the use of dissimilar skew angles (aka "mixed skew angles) permits us to place the direction of maximum momentum in desired directions. Virtually no research was found for CMGs using mixed skew angles. Finally, two new techniques are developed to reduce singularities remaining in the optimum geometry and even to penetrate the singularities without loss of attitude control. These new techniques have the potential to bestow worry-free aggressive maneuvering capability to military spacecraft.

The first volume of research presented in this thesis addresses minimum time slew maneuvers, but that only solves half of the problem. After slewing to the new target area in minimal time, military spacecraft must quickly settle and begin fine target tracking.

2. Fine Target Tracking

Target tracking is complicated by inaccuracies in estimated spacecraft inertia. Typical design techniques for controlling rigid spacecraft use an assumed inertia or an inertia experimentally determined on the ground. Consider the depicted satellite as a simple point of mass M and inertia J. If the inertia is known a *perfect* control torque $\tau_{control}$ is easily expressed for an inertial rotational maneuver per Newton's Law written for rotations (aka "Newton-Euler"): $\tau_{control}$ = (inertia) X (inertial rotational acceleration). For a desired inertial rotational acceleration, this is the "perfect feedforward" control. If the inertia were exact, *no tracking errors* would be incurred in the absence of external

3

disturbance torques. Since inertia is not exactly known, feedback control is also used to add control commands based on the *already-incurred* tracking error.
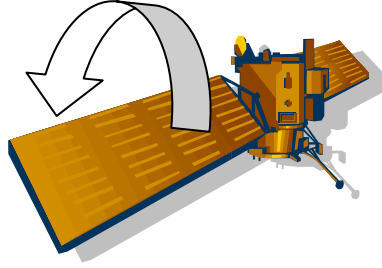
After a spacecraft reaches it's orbit, considerable time and effort are expended on system identification to obtain good values for inertia to aid future attitude control. Fuel expenditure during orbital insertion and during orbit maintenance in addition to gimbaled appendages make accurate inertia estimates a continual challenge for distant spacecraft. Nonetheless, more accurate inertia models yield better spacecraft control.

In the early 1990s, researchers introduced nonlinear adaptive control techniques to estimate on-orbit spacecraft inertia values using tracking errors. The updated inertia was used to formulate the controls and a reference trajectory was also utilized in both feedforward and feedback controls to further reduce tracking errors[43]. The method was completely derived *for three-dimensional rotational spacecraft maneuvers* and simulations demonstrated superior tracking *only* when compared to feedback control alone[44]. Comparisons were not made with combined classical feedforward plus feedback control (arguably the most common approach used today). The adaptive technique was formulated in the *inertial* reference frame and resulted in unwieldy calculations. For expensive spacecraft missions, computer memory is a precious commodity. Complicated algorithms that require high amounts of computer memory must provide comparable performance increase to justify consideration.

Shortly afterwards, a subsequent researcher *suggested* algorithmic simplification by formulating the technique in the *body* reference frame[46]. The method was derived for a three-dimensional example of *slip-translational* motion of the Space Shuttle (not *rotational spacecraft maneuvers*), and no comparative simulations were presented. This method seems quite promising for spacecraft attitude control (*rotational spacecraft maneuvers*) as it applies to acquisitions, tracking, and fine pointing. A substantial

development presented here derives the later method *in the body frame* for *spacecraft rotational maneuvers*. Simulations and experimental comparisons are made to proportional-derivative (PD) feedback alone, and combined classical feedforward-feedback control. Additionally, several improvements are suggested further improving performance. While the methods in the literature formulate both feedforward and feedback adaptive controls utilizing a reference trajectory, performance improvement is demonstrated using the reference trajectory only for the feedforward control maintaining typical PD feedback controls using the desired trajectory. It is further shown that estimation dynamics can be completely eliminated while maintaining significantly improved target tracking performance. Lastly, two algorithmic simplifications are introduced and compared in simulations and experiments.

Taken all together this dissertation entails some latest additions to ATP research demonstrating significant improvements to spacecraft slew maneuvers and tracking. Relatively greater improvements are achieved during slew maneuvers with further modest improvements during target tracking. Special attention is brought to the significance of considerable experimental work. Many promising advanced control techniques exist, but until they are proven to work experimentally program managers of space missions will be reluctant to utilize these advanced techniques.

Experimentation is difficult and can often frustrate the most seemingly simple algorithm. Real world systems (including spacecraft) are noisy and rarely behave exactly as predicted by simplified models. This thesis only contains research that has been experimentally verified on a free-floating spacecraft simulator. The proposed advanced control algorithms for target tracking and the control moment gyroscope developments for rapid slew will be proven effective with analytic argument followed by simulations and experimental verification.

B.   LITERATURE REVIEW
1.   Control Moment Gyroscopes for Rapid Slew Maneuvers

Despite singularity issues, CMG research began in 1960s for large satellites like SKYLAB (which used three dual gimbaled CMGs or DGCMGs)[7]. Computers of the time could not perform matrix inversion in real time. Simple systems that did not require

matrix inversion were an obvious choice. Otherwise algorithmically simple approximations must have been available for the system chosen. Singularity avoidance was researched a lot in the 1970s and 1980s.[8]-[14]
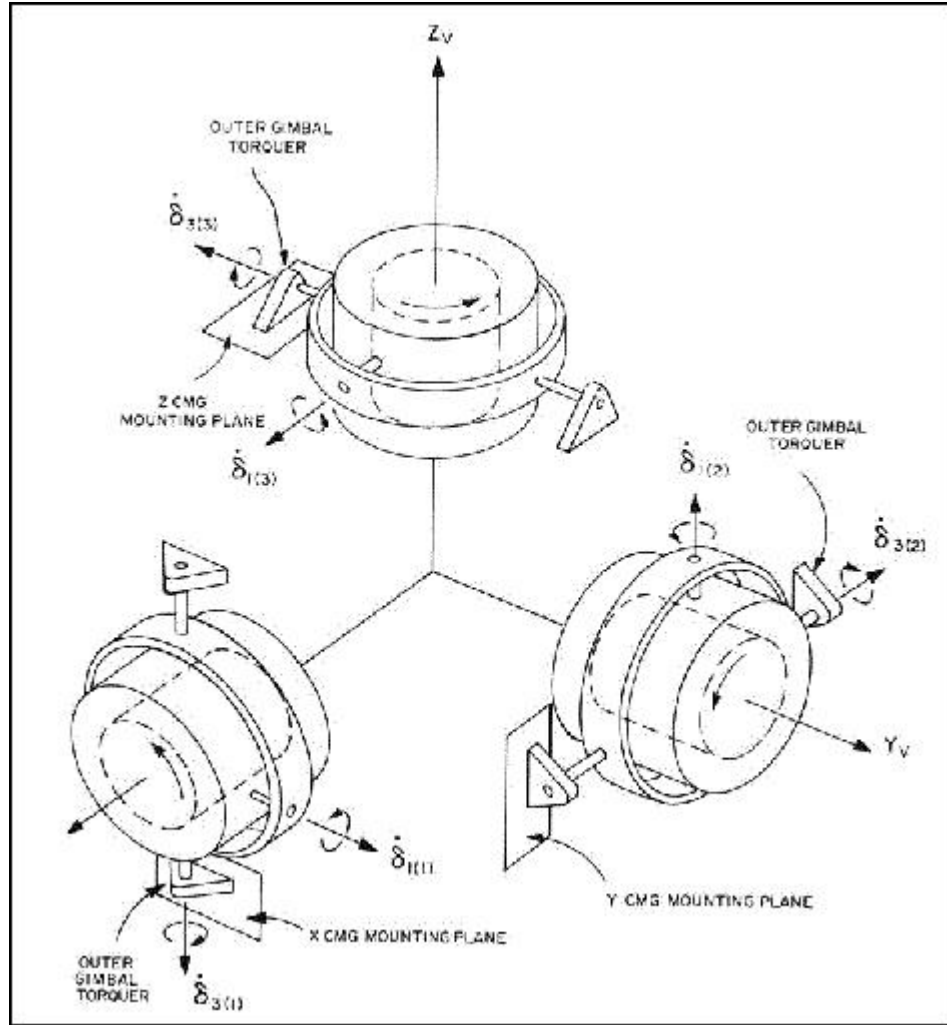
Figure 2 Skylab *Double Gimbaled* CMG mounting [5].

Singularity avoidance was typically done using a gradient method and double gimbaled CMGs[11],[12]. These gradient methods are not effective for Single Gimbaled CMGs (SGCMGs) like they are for Double Gimbaled CMGs (DGCMGs). Margulies was first to formulate a theory of singularity and control [13] including the geometric theory of singular surfaces, generalized solution of the output equation, null motion (using greater than three SGCMGs), and the possibility of singularity avoidance for general SGCMG systems. Also in 1978 Russian researcher Tokar published singularity

6

surface shape description, size of workspace, and considerations of gimbal limits[14]. Kurokawa identified that a system such as a pyramid type SGCMG system will contain an impassable singular surface and concluded systems with no less than 6 units provide adequate workspace free of impassable singular surfaces[15]. The MIR space station was designed for 6 SGCMG operations. This thesis will evaluate singularity-free operations using a mere three CMG array and continue to reduce singularities, then penetrate those remaining singularities.

Continued research aimed at improving results with less than 6 CMGs emphasized a 4 CMG pyramid[17]. Much research resulted in gradient methods that regard passability as a local problem that proved problematic [14],[16],[18]. Global optimization was also attempted but proved problematic in computer simulations[20]. Difficulties in global steering were also revealed in ref[21]. Reference [22] compared six different independently developed steering laws for pyramid type single gimbaled CMG systems. The study concluded that that exact inverse calculation was necessary (the exact inverse calculation will be used in this thesis). Other researchers addressed the inverted matrix itself adding components that make the matrix robust to inversion singularity [23],[24],[25] as extensions of the approach to minimize the error in generalized inverse Jacobian calculation [26]. These approaches introduce tracking error where necessary to avoid singularities by following a different momentum path (generating other-than-desired torque). The generalized singularity-robust inverse from ref [23] was initially utilized in this research for comparative purposes, and the results will be discussed.

This thesis will investigate exactly following the commanded path rather than a path that avoids singularities to minimize slew time. Momentum path planning is another approach used to attempt to avoid singularities that can also achieve optimization if you have knowledge of the command sequence in the near future [26],[34],[35]. Another method used to avoid singularities is to use null motion to first reorient the CMGs to desired gimbal positions that are not near singular configurations [36]. By definition, null motion is motion of the CMGs that result in a *net* zero torque. Null motion only exists when more than three SGCMGs are used. The extra degrees of freedom provided by a configuration with more than three SGCMGs are used to execute the null motion. Since this research is performed under the auspices of the Naval Postgraduate School's bifocal

relay spacecraft project, it is important to note most recently ref [30] reports on an analytical-numerical study of the complete symbolic expression of the equations of motion of a dual-body spacecraft, including standard singularity avoidance methods and analysis of robustness against inertia uncertainties. Both singularity avoidance and inertia uncertainty play pre-eminent roles in the research summarized in this dissertation.

Despite the massive amount of research done on CMGs, precision control with CMGs (especially only three SGCMGs) is still an unsolved problem [31],[33],[35].

2. Adaptive Spacecraft Control for Fine Target Tracking

Adaptive control techniques adapt control commands based upon errors tracking trajectories and/or estimation errors. *Direct* adaptive control techniques directly adapt the control signal without explicit estimation of system parameters. The control is reparameterized in terms of the parameters so that the estimates need not be translated into the control parameters after estimation [44]. On the other hand *indirect* adaptive control techniques indirectly adapt the control signal on the basis of estimates of the plant parameters. The plant parameters are explicitly estimated, then translated into the control separately [44]. The adaptation rule is derived in order to guarantee rapid elimination of tracking errors (the true objective) and global stability of the nonlinear closed loop system. Two fields of application of adaptive control is robotic manipulators and spacecraft maneuvers utilizing both approaches[38][39][40].

While some adaptive techniques concentrate on adaptation of the feedback control, others have been suggested to modify a feedforward control command retaining a typical feedback controller, such as Proportional-Derivative (PD). Anderson evaluated the filtered-x LMS algorithm with FIR estimation for adaptation of feedforward command signals[41]. Simpler adaptation rules have been used for adaptation of the control signal in the inertial reference frame[42]. *Hamiltonian Adaptive Control of Spacecraft* [43] presents such an inertial frame adaptive control. While the adaptation is simpler in general form, the resulting regression model used in the control signal requires several pages to express for three-dimensional spacecraft rotational maneuvers (included in the appendix). This key reference presents a starting point for the research presented here. Other references also utilizing the inertial frame[44] have been extended to include

attitude control system power tracking in the control signal[45], but still suffer from the algorithmic complexity that accompanies the inertial frame. The measured regression matrix of "knowns" is required in the control calculation, so this approach is computationally inappropriate for spacecraft rotational maneuvers. Subsequently, Slotine's 9-parameter estimation general approach [43] was *suggested* for implementation in the *body* reference frame by Fossen[46]. The method was derived for *slip translational motion* of the space shuttle, but neither simulated nor experimentally verified. Nonetheless, this method appears promising for practical implementation for three-dimensional spacecraft *rotational maneuvers*. Successful implementation could lead to improved target tracking accuracy with reduced tracking errors. System performance is enhanced by 1) updated inertia in the feedforward control signal, and 2) use of a reference trajectory that alters the desired trajectory in both feedforward and feedback using the tracking error. Adaptive controllers have become notorious since the 1960's and 1970s for instability. In 1966 Michael James Adams was killed when his X-15 aircraft was torn apart due to his adaptive control system[47],[48]. The X-15 entered a divergent spiral as the adaptive controller estimates diverged[49]. Accordingly, great efforts are exerted in this research to simplify the estimation and eventually eliminate estimation altogether.

The 9-parameter Slotine-Fossen approach will be derived for 3-dimensional spacecraft *rotational maneuvers*. Estimation requirements will be reduced with new 6-parameter and 3-parameter regression models. Finally a modification to the approach demonstrates improved performance maintaining simplified regression models by not using the reference trajectory in the feedback signal. Finally, elimination of estimation will be achieved without sacrificing tracking performance. After promising simulations, experimental verification is performed on a free-floating, three-axis spacecraft simulator.

C. THESIS OVERVIEW

With this review of the literature, unique contributions in this thesis may be summarized:

1. Development of the optimal geometry for skewed arrays of *only three* single-gimbaled control moment gyroscopes resulting in maximum singularity-free momentum space,

2. the direction of maximized singularity-free momentum may be rotated to a desired direction utilizing mixed skew angles,

3. further singularity reduction using a new decoupled control steering technique,

4. development of a simple, yet effective singularity penetration method to deal with the residual singular states remaining in the momentum space

5. derivation of a 9-parameter adaptive control technique suggested in the literature for spacecraft rotational maneuvers including critical comparison to the most effective control methods currently used for spacecraft via simulations and experimentation,

6. parameter estimation reduction (6-parameter) resulting in equivalent, simpler adaptive control algorithms with inertia estimation

7. further parameter estimation reduction (with valid assumptions) leading to 3-parameter adaptive control,

8. introduction of a new alternative adaptive control algorithm further reducing target tracking errors (eliminate reference trajectory from the feedback instead using desired trajectory in a PD feedback architecture),

9. demonstration that estimation may be eliminated in the approaches studied simplifying the control algorithms.

A comprehensive theoretical development is now appropriate. Theoretical development is organized topically. The first topic to be addressed is high-torque, rapid

10

spacecraft slew acquisitions maneuvers. Afterwards, adaptive feedforward control for improved target tracking accuracy is presented. Both topics include simulations to illustrate the theory.

Afterwards, a detailed description of the experimental hardware is provided to allow duplication of the results presented here. With a full understanding of the hardware, experimental results are presented to verify the theory. The results of the simulations and experiments will be summarized to accumulate the combined impact of these new developments.

THIS PAGE INTENTIONALLY LEFT BLANK

II. ANALYTICAL DEVELOPMENT

A. INTRODUCTION

Theoretical development has been divided into two distinct areas based on subject matter: 1) acquisitions maneuvers utilizing control moment gyroscopes, and 2) target tracking maneuvers with adaptive feedforward control. Spacecraft attitude dynamics is the key foreknowledge presented first. This first section will reveal that a spacecraft performs rapid slew maneuvers by generating a change in angular momentum, $\mathbf{H}$. To minimize maneuver time, maximum momentum generation is required. Discussion continues in the second section with an understanding of how CMGs generate torque (equivalently momentum change, $\dot{\boldsymbol{H}}$) and includes an introduction of four new methods to maximize torque generation for rapid spacecraft slew maneuvers. Afterwards, adaptive control for fine target tracking maneuvers is described beginning with the basic Newton-Euler relationship for spacecraft attitude dynamics. Proposed improvements to existing techniques are suggested, so the theoretical development is firmly based in these existing techniques. Efforts are made to quickly summarize the theory of previous researchers then clearly indicate improved techniques.

B. SPACECRAFT ATTITUDE DYNAMICS AND CONTROL

Newton's Law is commonly known: the sum of forces acting on a body is proportional to its resultant acceleration, and the constant of proportionality is the body's mass. This applies to all three axes of motion for 3-dimensional space, so the law can also be stated as "the summed force vector [3x1] acting on a body is proportional to it's resultant acceleration vector [3x1], and the constant of proportionality is the body's mass matrix [3x3]". One crucial point is that this basic law of physics applies only in an inertial frame that is not in motion itself.

A similar law may be stated for rotational motion just as we have stated Newton's Law for translational motion. The rotational motion law is often referred to as Newton-Euler, and it may be paraphrased as: "the summed *torque* vector [3x1] acting on a body is proportional to it's resultant *angular* acceleration vector [3x1], and the constant of proportionality is the body's mass *inertia* matrix [3x3]." Newton-Euler also only applies

13

in a non-moving, inertial frame. Notice how Figure 3 depicts our situation. The equations needed to express the spacecraft's rotational motion are valid *relative to* the inertial frame (indicated by subscript "B/i" often assumed) and may be *expressed* in inertia coordinates ('**x**' used to indicate generalized inertial coordinates). The motion measurement *relative to* the inertial frame is taken from onboard sensors *expressed in* a body fixed frame ('**q**' used to indicate generalized body coordinates). It is stressed here that **q** does *not* refer to the inertial quaternion here. Generally, "**x**" will refer to quantities expressed in inertial coordinates and "**q**" will indicate expression in generalized body coordinates.

Another common manner to express these quantities is using both superscript and subscripts. Ref[17] pg. 340 is one such nomenclature where $\omega_B{}^{b/i}$ is used to describe angular velocity of the spacecraft body *with respect to* inertial *expressed in* body coordinates. The subscript in this reference refers to "expressed in" and the superscript refers to "with respect to," so: $\dot{\vec{H}} = \left\{\dfrac{d\vec{H}}{dt}\right\}_i = \left\{\dfrac{d\vec{H}}{dt}\right\}_B + \omega^{B/i} \times \vec{H}$ where $\vec{H} = \hat{J} \cdot \vec{\omega}$.

Still other references reverse the sub/superscript usage so that $\omega_{b/i}{}^B$ is used to describe the same angular velocity of the spacecraft body *with respect to* inertial *expressed in* body coordinates. All the various nomenclatures are emphasizing that differentiation of position must account for movement of a frame *relative to* the inertial frame, since Newton and Newton-Euler apply in the inertial frame. The complicated use of both superscripts & subscripts is not adopted here. In this document **q** refers to "expressed in" *non-specific* body coordinates (with ω as one example *specific* body coordinate for rate) and **x** refers to "expressed in" inertial coordinates. Since differentiation *with respect to* a frame remains important, subscript "B/i" is retained for this purpose. This permits easy translation of nomenclature between the two major topics investigated in this thesis: acquisitions maneuvers and tracking with adaptive control. The literature on large momentum spacecraft slew maneuvers often uses ω, while adaptive control literature is often uses $\dot{q}$ to express the same quantity. $\omega_{B/i}$ will indicate angular

velocity of the body *with respect to* inertial *expressed in* body coordinates (equivalently

$\dot{\boldsymbol{q}}_{B/i}$).

Note the applied torque T is a rate of change of angular momentum $\dot{\boldsymbol{H}}$ where angular momentum is the product of mass inertia and angular velocity:

$\sum \{\mathbf{T}\}_{B/i} = \{\dot{\mathbf{H}}\}_{B/i} = [\mathbf{J}]\{\ddot{\mathbf{x}}\}_{B/i}$.
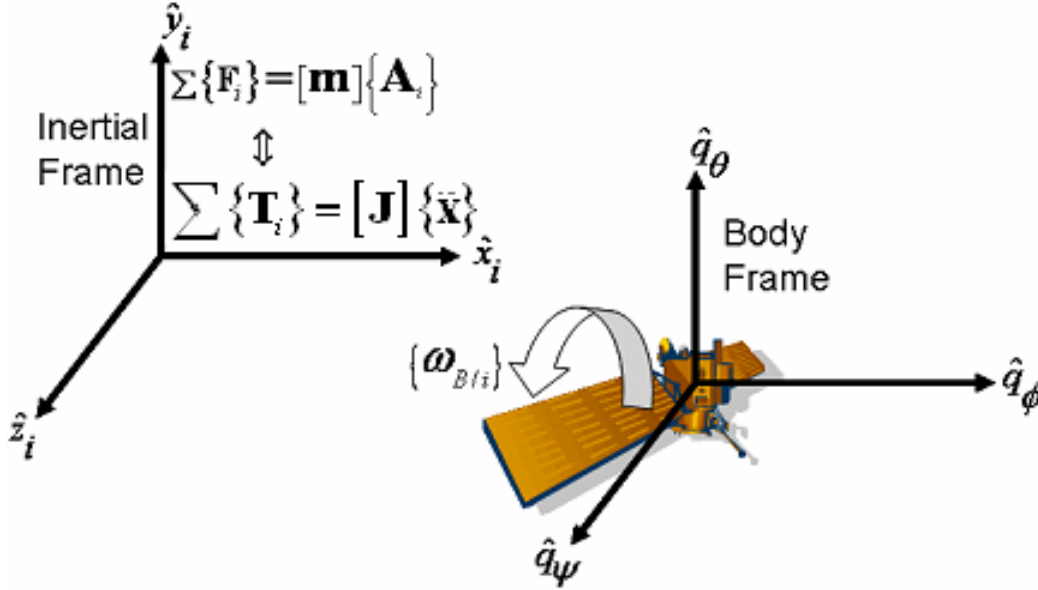
Figure 3 Spacecraft Dynamics and coordinate reference frames.

Motion equations may be expressed in body coordinates if the body coordinate *frame motion* is addressed relative to the inertial frame where motion of body frame relative to inertia is indicated by subscript 'B/i'.

$$[\mathbf{J}]\{\ddot{\mathbf{x}}\}_{B/i} = [\mathbf{J}]\{\dot{\boldsymbol{\omega}}\}_{B/i} + \{\boldsymbol{\omega}\}_{B/i} \times [\mathbf{J}]\{\boldsymbol{\omega}\}_{B/i} \qquad (1)$$

With this understanding, equations of motion of a spacecraft with no assumed control actuators are often written in body coordinates dropping subscripts in terms of the non-specific or specific body coordinates. In equation (2), note the [**C**] matrix is formed by replacing the cross product operation with matrix multiplication of a skew symmetric matrix. This procedure is performed later when defining a reference trajectory

(sectionII.0.00 for adaptive control and is a key substitutive step in the stability proof (sectionII.0.00 of the proposed, improved adaptive control algorithm.

$$\sum\{\mathbf{T}\}_{B/i} \Rightarrow \tau_B = \dot{\mathbf{H}} = [\mathbf{J}]\{\dot{\boldsymbol{\omega}}\} + \{\boldsymbol{\omega}\} \times [\mathbf{J}]\{\boldsymbol{\omega}\} = [\mathbf{J}]\{\ddot{\mathbf{q}}\} + \underbrace{\{\dot{\mathbf{q}}\} \times [\mathbf{J}]\{\dot{\mathbf{q}}\}}_{[\dot{C}]} \tag{2}$$

Control laws are written to command (**u**) a torque (or momentum rate) to accomplish a maneuver ($\dot{\mathbf{H}}_{cmg}$), and the command is sent from the control law to actuators to achieve the corresponding spacecraft system momentum rate $\dot{\mathbf{H}}$. Thus, frequently, τ (for torque in non-specific body coordinates), **u** (for command), and $\dot{\mathbf{H}}$ for momentum change are frequently expressing an identical magnitude. Getting back to the equations of motion expressed in body coordinates (equations 1,2), performing the multiplications reveals a nonlinear set of equations.

Define the angular velocity vector and its derivative:

$$\{\boldsymbol{\omega}\} = \begin{Bmatrix} \omega_x \\ \omega_y \\ \omega_z \end{Bmatrix} = \begin{Bmatrix} \dot{q}_x \\ \dot{q}_y \\ \dot{q}_z \end{Bmatrix} \quad \text{and} \quad \{\dot{\boldsymbol{\omega}}\} = \begin{Bmatrix} \dot{\omega}_x \\ \dot{\omega}_y \\ \dot{\omega}_z \end{Bmatrix} = \begin{Bmatrix} \ddot{q}_x \\ \ddot{q}_y \\ \ddot{q}_z \end{Bmatrix} \tag{3}$$

Define the [3x3] inertia matrix $\begin{bmatrix} J_{xx} & J_{xy} & J_{xz} \\ J_{yx} & J_{yy} & J_{yz} \\ J_{zx} & J_{zy} & J_{zz} \end{bmatrix}$ and multiply out equation 2:

$$\begin{Bmatrix} \tau_x \\ \tau_y \\ \tau_z \end{Bmatrix}_B = \begin{bmatrix} -H_y\omega_z + H_z\omega_y + J_{xx}\dot{\omega}_x + J_{xy}\dot{\omega}_y + J_{xz}\dot{\omega}_z \\ H_x\omega_z - H_z\omega_x + J_{yx}\dot{\omega}_x + J_{yy}\dot{\omega}_y + J_{yz}\dot{\omega}_z \\ -H_x\omega_y + H_y\omega_x + J_{zx}\dot{\omega}_x + J_{zy}\dot{\omega}_y + J_{zz}\dot{\omega}_z \end{bmatrix} \tag{4}$$

$$\begin{Bmatrix} \tau_x \\ \tau_y \\ \tau_z \end{Bmatrix}_B = \begin{bmatrix} \dot{\omega}_x & \dot{\omega}_y & \dot{\omega}_z & -\omega_y\omega_z & 0 & \omega_z\omega_y \\ \omega_x\omega_z & \dot{\omega}_x & 0 & \dot{\omega}_y & \dot{\omega}_z & -\omega_z\omega_x \\ -\omega_x\omega_y & 0 & \dot{\omega}_x & \omega_y\omega_x & \dot{\omega}_y & \dot{\omega}_z \end{bmatrix} \begin{Bmatrix} J_{xx} \\ J_{xy} \\ J_{xz} \\ J_{yy} \\ J_{yz} \\ J_{zz} \end{Bmatrix} = [\Phi]\{\Theta\} \tag{5}$$

16

Notice the x axis acceleration depends upon motion in other axes. The equations of motion are nonlinear and coupled due to off-diagonal inertia terms and the cross product operation. The equations may also be expressed in regression form as the product of a measurable matrix and a vector of unknown parameters to be estimated (eqn. 5). In instances where inertia off-diagonal terms are negligible (as in eqn. 6), motion axes remain coupled by the cross-product operation.

$$\begin{Bmatrix} \tau_x \\ \tau_y \\ \tau_z \end{Bmatrix}_B = \begin{bmatrix} -H_y\omega_z + H_z\omega_y + J_{xx}\dot{\omega}_x \\ H_x\omega_z - H_z\omega_x J_{yy}\dot{\omega}_y \\ -H_x\omega_y + H_y\omega_x + J_{zz}\dot{\omega}_z \end{bmatrix} \qquad (6)$$

Notice the equation may also be written as a product of a matrix and a vector comprised of 6 inertia components of a symmetric inertia matrix. This fact will be exploited later using adaptive control. Rotational transformation matrices may be used to translate coordinates, so that the inertial mathematical expressions (Newton, Newton-Euler, etc.) may be *expressed in* body coordinates. $[R]_{b2i}$ is nomenclature used to express a rotational transformation matrix that expresses an expression written in body coordinates into inertial coordinates. Later the two basic adaptive control techniques present in the literature are respectively formulated in inertial and body coordinates, so the rotational transformation matrix will play a major role in the procedures.

Lacking any external disturbance torques, equation (2) may be written in a manner that highlights the use of CMG actuators to generate a torque by momentum exchange:

$$\sum \{\mathbf{T}\}_{B/i} \Rightarrow u = \tau = -\left(\dot{\mathbf{H}}_{cmg} + \omega \times \mathbf{H}_{cmg}\right) \qquad (7)$$

In order to achieve a specified momentum change from an array of CMGs ($\dot{\boldsymbol{H}}_{cmg}$), a command must be submitted to the gimbal motor. Torque is related to rate of change of angular momentum via Newton-Euler, resulting in the mathematical relationship between gimbal commands and torque output called a CMG steering law. CMG steering laws for "i=1,2,3…" CMGs contain a matrix ([**A**]) of combinations of CMG skew angles, β_i and CMG gimbal angles, θ_i. Equation (9) shows this relationship

for i=1,2,3 CMGs normalized by one CMG's worth of momentum (*1H*). CMGs are inclined such that their gimbal planes form skew angles, β_i with respect to the xy plane as depicted in Figure 8. The [**A**] matrix (containing gimbal angles, θ_i and skew angles, β_i) must be inverted to find the required CMG gimbal rate command for commanded output torque per equation (12). Begin by writing equations for each momentum vector in xyz coordinates for 3 CMGs normalized by 1H.

$$\mathbf{H}_{CMG} = h_x\hat{\mathbf{x}} + h_y\hat{\mathbf{y}} + h_z\hat{\mathbf{z}} \tag{8}$$

$$\textbf{where} \quad \begin{array}{l} h_x = \cos\theta_3 - \cos\theta_1 + \cos\beta\sin\theta_2 \\ h_y = \cos\beta(\sin\theta_3 - \sin\theta_1) - \cos\theta_2 \\ h_z = \cos\beta(\sin\theta_1 + \sin\theta_2 + \sin\theta_3) \end{array} \tag{9}$$

$$\frac{\partial \mathbf{H}_{CMG}}{\partial\boldsymbol{\theta}} = \underbrace{\begin{bmatrix} \sin\theta_1 & \cos\beta\cos\theta_2 & -\sin\theta_3 \\ -\cos\beta\cos\theta_1 & \sin\theta_2 & \cos\beta\cos\theta_3 \\ \sin\beta\cos\theta_1 & \sin\beta\cos\theta_2 & \sin\beta\cos\theta_3 \end{bmatrix}}_{[\mathbf{A}]} \tag{10}$$

The Newton-Euler relation relates generated torque to the timed-rate of change of angular momentum of the spacecraft system. A CMG absorbs momentum, $\dot{\mathbf{H}}_{CMG}$ causing an equal and opposite change in momentum on the spacecraft. For 3 CMGs, the general relation for momentum change is:

$$\dot{\mathbf{H}}_{CMG} = \frac{\partial\mathbf{H}_{CMG}}{\partial\boldsymbol{\theta}}\frac{\partial\boldsymbol{\theta}}{\partial t} = \frac{\partial\mathbf{H}_{CMG}}{\partial\boldsymbol{\theta}}\dot{\boldsymbol{\theta}} = [\mathbf{A}]\{\dot{\boldsymbol{\theta}}\} \tag{11}$$

$$[\mathbf{A}]^{-1}\dot{\mathbf{H}}_{CMG} = [\mathbf{A}]^{-1}[\mathbf{A}]\{\dot{\boldsymbol{\theta}}\} = \{\dot{\boldsymbol{\theta}}\} \tag{12}$$

Notice we invert the [**A**] matrix, so that we may use the required momentum change commanded by a control law to calculate the corresponding CMG steering commands. For this reason, the equation is referred to as a CMG control steering law. *Singular inversion of [A] results in singular conditions that can result in loss of spacecraft attitude control.*
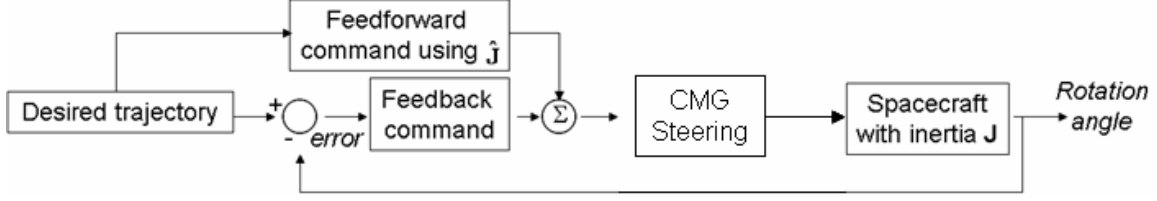
Figure 4 CMG steering relationship with a feedback controller.

For some combinations of gimbal and skew angles, the [**A**] matrix columns can become linearly dependent. At these combinations of skew and gimbal angles, the determinant of the [**A**] matrix becomes zero leading to singular inversion.

$$\det[\mathbf{A}]=\sin\beta\left\{\sin\theta_2\left[\sin(\theta_1+\theta_3)\right]+\cos\beta\cos\theta_2\left[\sin(\theta_3-\theta_1)+2\cos\theta_1\cos\theta_3\cos\beta\right]\right\} \qquad (13)$$

C.   ACQUISITIONS MANEUVERS

1.   Introduction

Rapid spacecraft reorientation often drives design engineers to consider use of Control Moment Gyroscopes (CMGs). CMGs are momentum exchange devices that exhibit extreme torque magnification (i.e. for a small amount of torque input to the CMG gimbal motors, a large resultant output torque is achieved). Typical output torques are on the order of hundreds to thousands of times the torque output of reaction wheels, another kind of momentum exchange attitude control actuator.   A CMG contains a constantly rotating (high speed) wheel that generates a strong momentum vector. The momentum vector is gimbaled by small gimbal motors resulting in a momentum change (i.e. torque per eqn. 11).   Reaction wheels must spin up to the required speed to generate the commanded torque (taking some spin up time). For CMGs however, the high torque application is instantaneous.

For maximum speed, minimum-time spacecraft acquisitions maneuvers, maximum spacecraft angular momentum generation is required. Since the total system angular momentum in conserved, maximum CMG momentum is implied. Control laws are used to command CMG gimbal steering to generate this angular momentum.

19

Unfortunately, certain combinations of gimbal angles and skew angles result in singular states where the system of CMGs cannot generate the commanded torque despite the non-saturated state of the CMG array.

Arguably, the most common configuration for a skewed array of 4 CMGs is the "pyramid" array where the 4 CMGs are skewed at an angle of $\beta=54.73^O$ resulting in an "optimal spherical" max momentum capability [17]. The desire for such a configuration is often stated as an equivalent, *maximized* momentum capability in all directions based on the {++++} or {----} 0H & 4H saturation singularities (Figure 5) where all four CMGs are pointing in the same direction when a singularity occurs (also called saturation in this case). The typical design approach may be succinctly stated: 1) Optimize spherical momentum, then 2) minimize impact of singularities. The approach adopted in this paper will reverse the traditional approach as follows: 1) Minimize singularities, and then 2) maximize spherical momentum. Surprisingly, the result turns out quite differently.
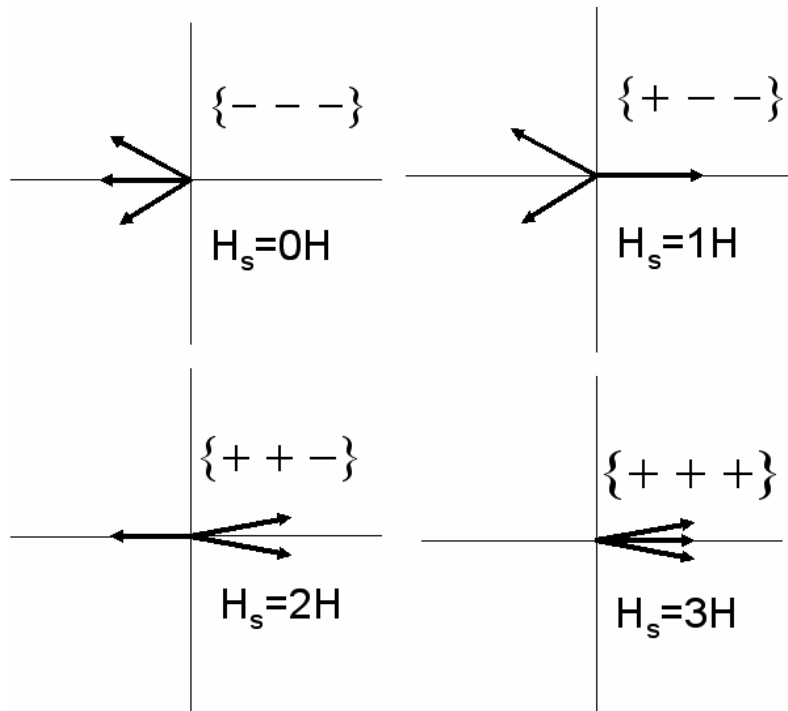
Figure 5 3/4 CMG Singularity nomenclature.

Individual CMG momentum directions (positive-right convention) for a 3/4 CMG skewed array in a singular configuration of gimbal angles.

20
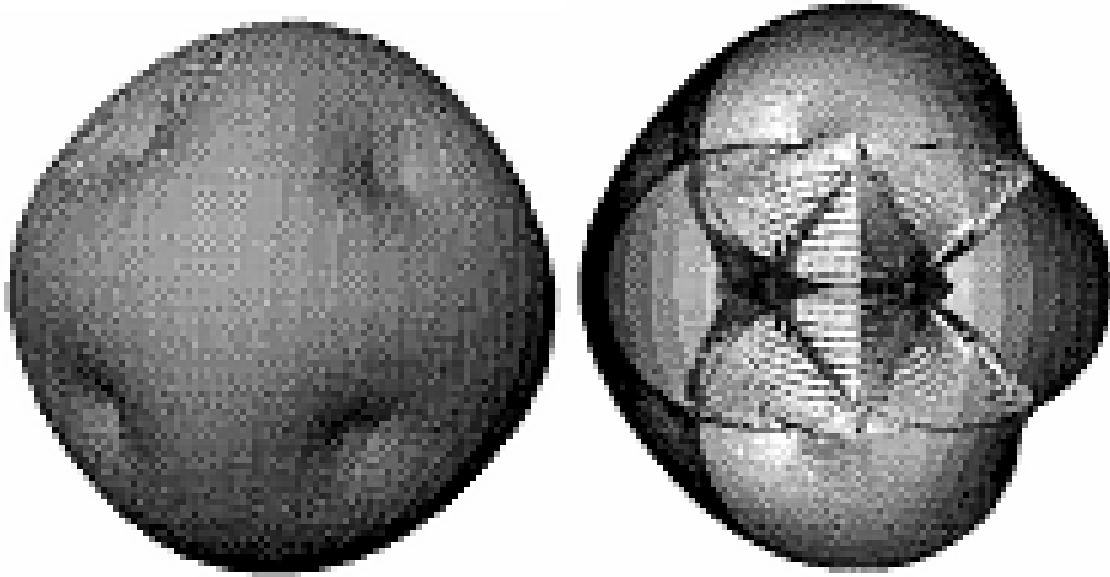
Figure 6 Singular surfaces.

Left: External (4H & 0H) singularity surfaces typically used to define the "optimal spherical" skew angle, Right: Internal (1H & 2H) singularities generate errors & potential instability as momentum trajectory strikes one of these surfaces. [6]
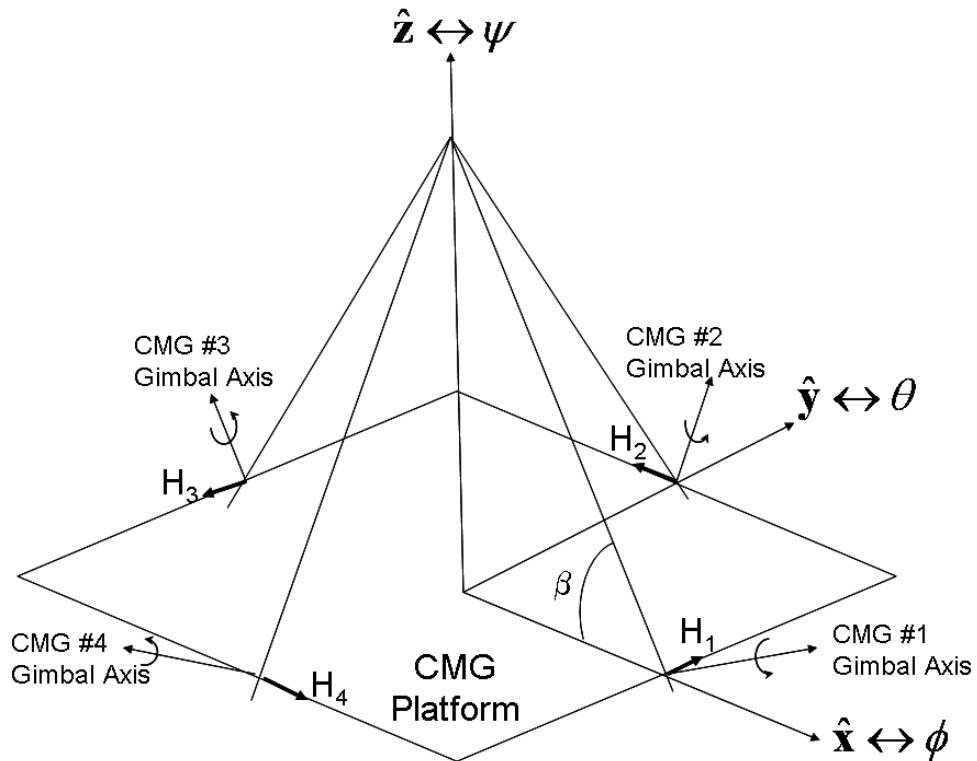
Figure 7 Four CMG array.

CMGs skewed at angle, β. Gimbal rotations obey right hand rule.

Unique contributions in *this portion* of the thesis may be summarized:

1.   Development of the optimal geometry for skewed arrays of only three single-gimbaled control moment gyroscopes resulting in maximum singularity-free momentum space,

2.   momentum space rotation to place maximum singularity-free momentum in desired direction

3.   further singularity reduction using a new decoupled control steering technique,

4.   development of a simple, yet effective singularity penetration method to deal with the residual singular states remaining in the momentum space

2.   The ¾ Skewed CMG Array

The 3/4 CMG array modifies the commonly studied 4 CMG skewed pyramid. A minimum of 3 CMGs are required for 3-axis control, and the fourth is used for singularity avoidance. With the 3/4 array, only 3 CMGs are utilized for active attitude control with the fourth CMG held in reserve for robust failure properties. Experimental verification will be provided in later sections utilizing a spacecraft testbed with a 3/4 CMG array containing a balance mass in the place of the fourth CMG (Figure 8).
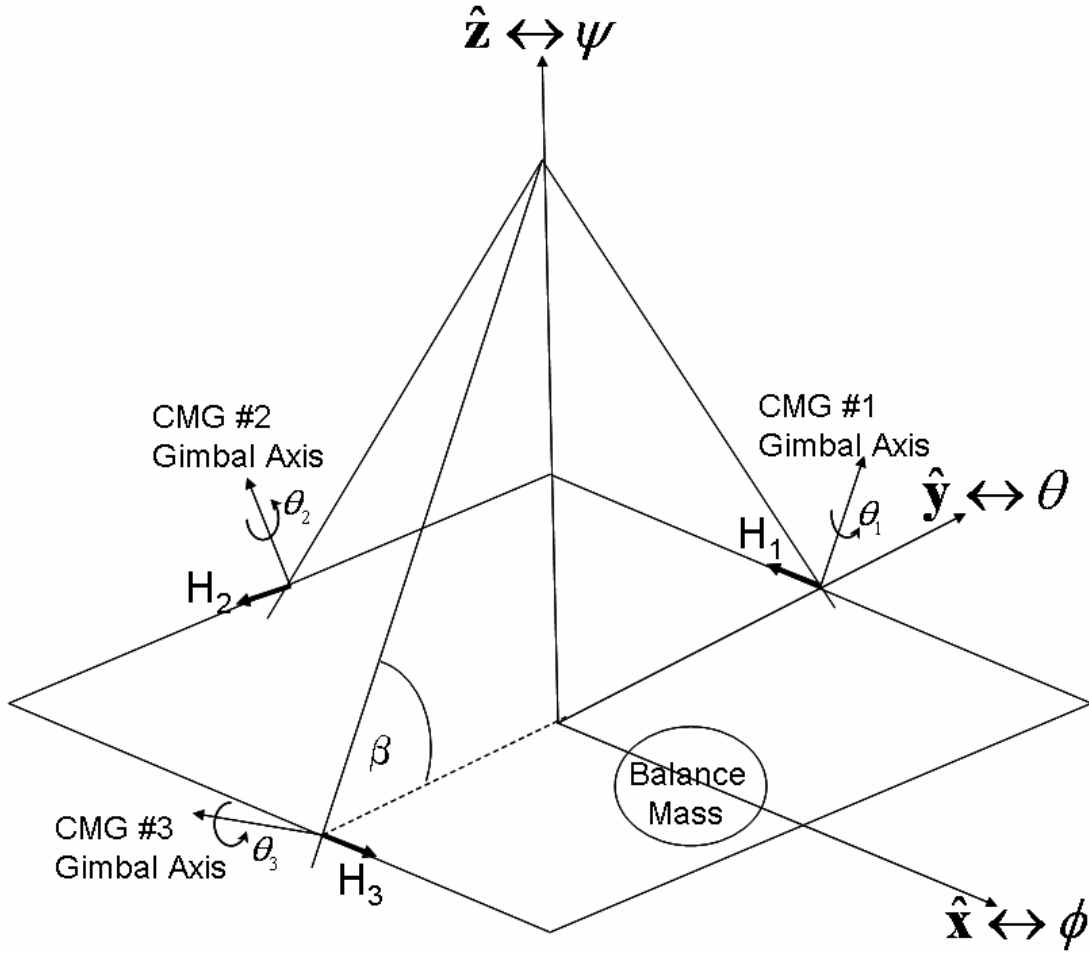
Figure 8 3/4 Skewed CMG array.

This is the configuration utilized in this study with balance mass in place of one CMG station.

Many of the cited references approach CMG singularity avoidance by modifying the [**A**] matrix itself to make it invertible without singularities. The approach taken by the author is to first optimize the array geometry itself for the maximum *singularity-free* momentum space specifically for a 3/4 skewed array. Since gimbal angles can vary independently, the primary design task is to choose the skew angle that provides the greatest singularity-free momentum. With all three CMGs skewed at the "optimal *singularity-free*" skew angle the 3/4 CMG array can operate at momentum values less than the singularity-free threshold without any kind of singularity avoidance scheme. Further, utilization of mixed skew angles can rotate the CMG array's capability to maximize momentum in any preferred direction, again singularity-free. Yaw is the preferred direction in this study. A direct comparison with the traditional "optimal

spherical" skew angle will demonstrate the dramatic improvement in torque capability of the CMG array. Analytical derivation via linear algebra is followed by a heuristic, geometric analysis approach and later validated experimentally.

3. Optimum Geometry Maximum Singularity-Free Momentum

Singular combinations of gimbal angles and skew angles can be determined analytically by examining the determinant of the [**A**] matrix. When the determinant goes to zero, the matrix has linearly dependent columns resulting in singular inversion. There are six cases (with multiple sub-cases) that result in a singular [**A**] matrix with $\beta_i = \beta$ for $i = 1, 2, 3$.

Case 1: $\sin\beta = 0$

Case 2: $\sin(\theta_1 + \theta_3) = \sin(\theta_3 - \theta_1) + 2\cos\theta_1\cos\theta_3\cos\beta = 0$

Case 3: $\sin\theta_2 \left[\sin(\theta_1 + \theta_3) \right] + \cos\beta\cos\theta_2 \left[\sin(\theta_3 - \theta_1) + 2\cos\theta_1\cos\theta_3\cos\beta \right] = 0$

Case 4: $\sin\theta_2 = \cos\beta\cos\theta_2 = 0$

Case 5: $\sin(\theta_1 + \theta_3) = \cos\beta\cos\theta_2 = 0$

Case 6: $\sin\theta_2 = \sin(\theta_3 - \theta_1) + 2\cos\theta_1\cos\theta_3\cos\beta = 0$

Nontrivial cases may be analyzed as follows. In general, for a given skew angle, each case produces gimbal angle combinations that result in det[**A**]=0. These gimbal combinations may be used to calculate the resultant momentum at the singular condition (labeled "singular momentum," $\mathbf{H}_S$ in the code provided in the appendix). Minimum singular momentum values may then be plotted for iterated skew angles $0^O < \beta \le 90^O$. Having established the minimum value of momentum at singular combinations of gimbal angles, singularity is avoided provided the momentum is less that in these values depicted in Figure 10. Thus the result is the maximum singularity-free momentum space. Figure 10 reveals that maximum singularity-free momentum space is greatest (1H) for ninety degree skew angles.
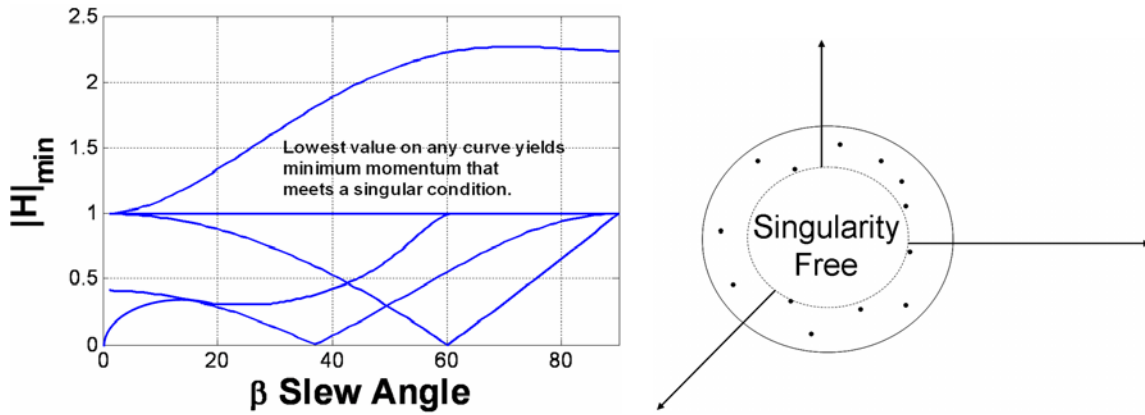
Figure 9 Skew angle optimization method.

Note each case (1-6) listed above has multiple sub-cases that cause that singular case to be met. Sub-cases were plotted and some of them are presented in Figure 9 for demonstration of the method. Each curve in Figure 9 does not represent a case (1-6) directly.
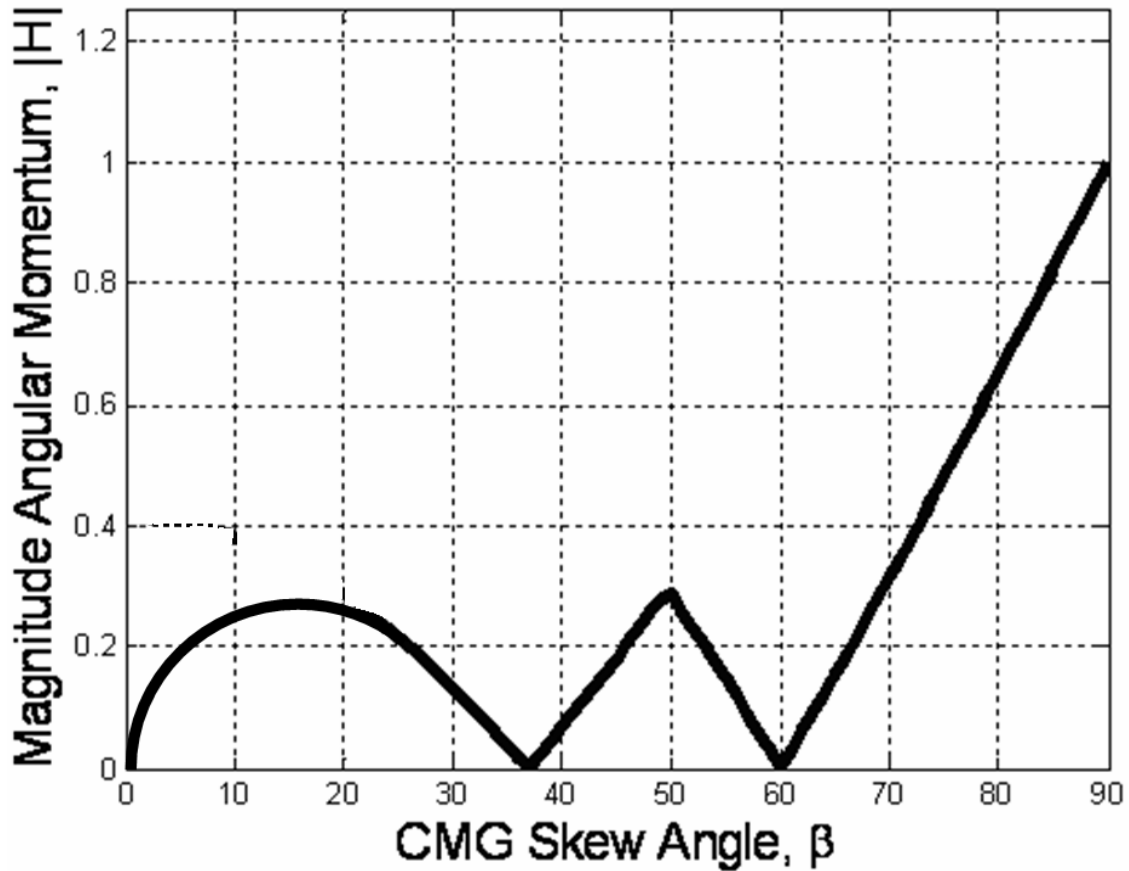
Figure 10 CONTRIBUTION #1: Skew angle optimization results.

Analytical demonstration that maximum singularity-free normalized momentum is obtained with a skew angle of $\beta=90^{o}$.
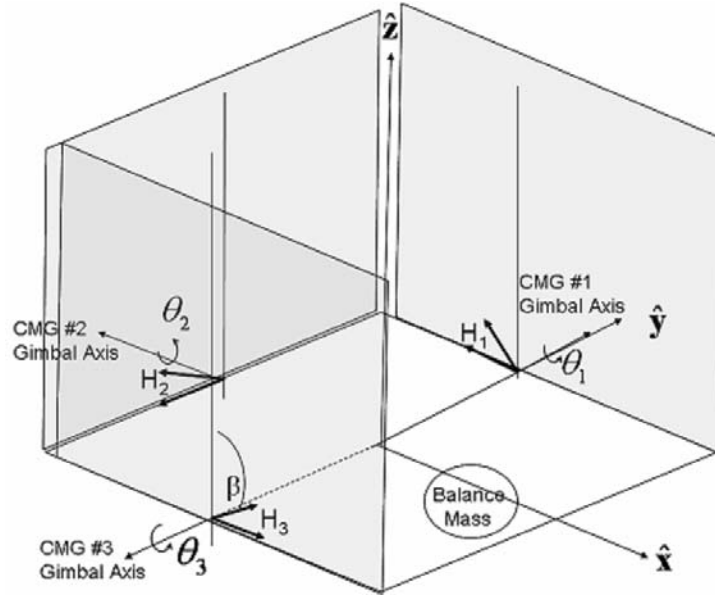
Figure 11 Optimal singularity-free 3/4 CMG configuration.

3/4 CMG skewed array momentum cutting planes with $\beta=90^\circ$.

Recall the nomenclature that one CMGs maximum momentum is designated 1H. A ubiquitous CMG installation geometry is the *four* CMG skewed pyramid with CMGs skewed at 54.73° to the local horizontal. As we see, this extensively studied skew angle yields 0.15H momentum before reaching a singular state for three CMGs. To avoid singularities to maintain attitude control, spacecraft control torque is limited to less than 0.15H. Thus utilizing the skew angle optimized for spherical maximum momentum with four SGCMGs, *only 15%* of one CMG's torque is achievable singularity free utilizing three SGCMGs. Using the new skew angle of $\beta=90^\circ$, 1.0H is achievable singularity-free in any direction. That's a 567% increase in singularity-free momentum.

a.   *Heuristic Analysis*

The preceding analytical analysis reveals singularity free operations <1H in all directions by implication. While useful, the analytical analysis certainly does not yield much intuition to guide the attitude control engineer to design safe momentum trajectories through the momentum space. Are there directions that can exceed 1H singularity-free?

Recent advances in computer processors speeds make a heuristic approach easily accomplished. Consider rotating a vector 360° creating a CMG gimbal "cutting"

plane (discretized at some interval). Then rotate the gimbal plane 360° creating a lattice of discrete points forming a solid, filled sphere. This discretized lattice provides points to analyze CMG array momentum. This is easily done in embedded loops of computer code. Each discrete point corresponds to a set of three coordinates or equivalently three gimbal angles. At each discrete point, singularity/non-singularity of [**A**] is established. *At singular points*, the normalized magnitude of angular momentum may be calculated. A point may be plotted at the magnitude of the momentum in the singular direction. This results in a three dimensional singularity map granting *easy* intuition for maneuvering in the momentum space. Singular surfaces result from several kinds of singularities: 0H, 1H, 2H, and 3H depicted in Figure 5. Typically, skew angle is determined by the outer, saturation singular surface alone (0H & 3H in this case of a 3/4 CMG array). In order to find the maximum *singularity-free* skew angle, the analysis absolutely must also account for the 1H and 2H internal singularities.

It may be noted here that the often used "optimal spherical" skew angle ($\beta=54.73^o$) that results in equivalent momentum in all directions is derived utilizing the 0H {----} & 4H {++++} singular surface (Figure 5) of a 4 CMG skewed array. The 4H singular surface is the saturation surface that results from all 4 CMGs pointing in the same direction, and it's corresponding saturation surface for the 3/4 array is the 0H & 3H singular surfaces. In the case of a 3/4 CMG array the singular surfaces are depicted in Figure 12 for the often used "optimal spherical" momentum skew angle ($\beta=54.73^o$).
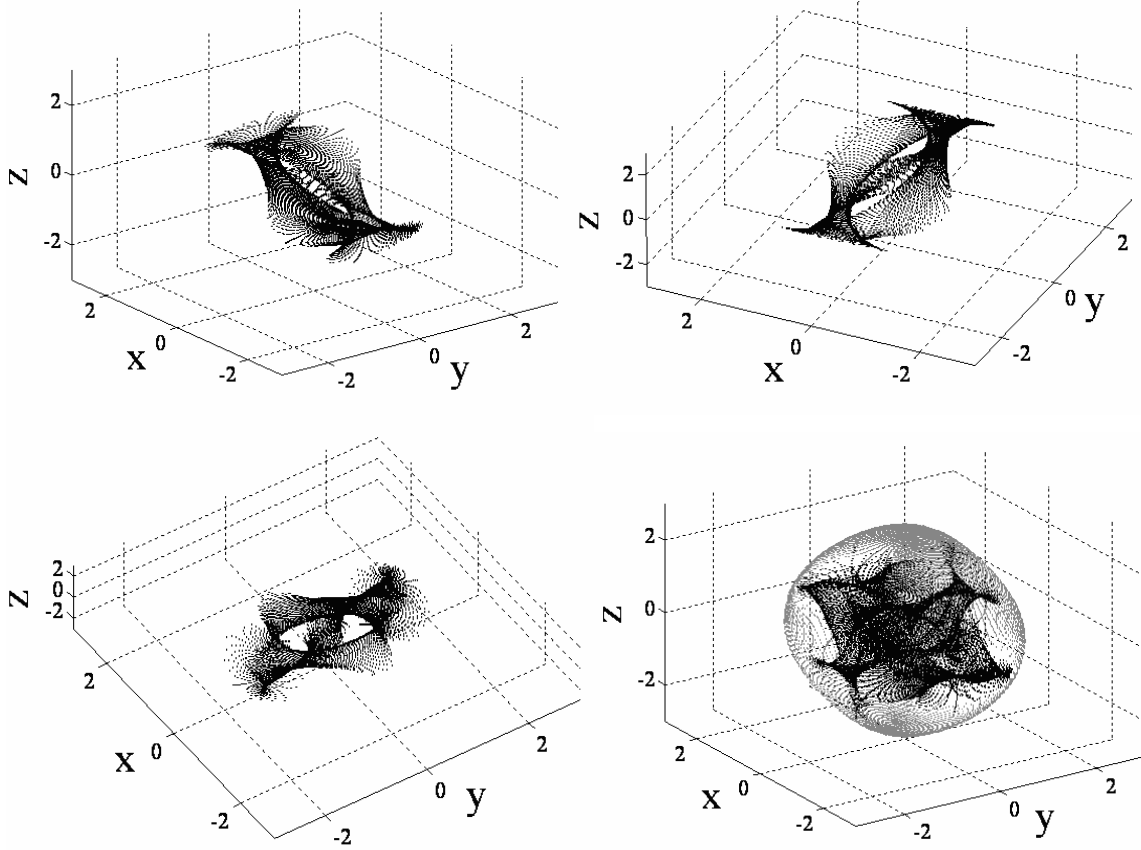
Figure 12 Optimal singularity-free 3/4 CMG singular surfaces.

Singular surfaces for 3/4 CMG skewed array at "optimal spherical " momentum skew angle $\beta=54.73^\circ$. Top: 1H & 2H surfaces, Bottom left: 1H & 2H surface; Bottom right=1H & 2H surfaces inside 0H & 3H surfaces.

Note the spherical nature of the external, saturation singular surface {+++} typified by the ubiquitous 4 CMG pyramid array skewed at $\beta=54.73^O$ is nearly maintained in the 3/4 array. The internal 1H and 2H singularities are quite a problem, since they occupy a large portion of the momentum space. The combined singularity hypersurface makes it difficult to see a clear momentum path away from the origin (0,0,0). This is quite important, since CMGs must spin up at a zero-momentum gimbal angle configuration lest they impart massive torques onto the spacecraft. $\{\theta_1,\theta_2,\theta_3\}=\{0,0,0\}$ is one very common zero momentum spin-up configuration. The typical design methodology might use the shape of the 3H outer momentum surface {+++} to define $\beta=54.73^O$ as the "optimal spherical" momentum skew angle. The attitude

control engineer would be left with the daunting task of maneuvering in this crowded momentum space while trying to avoid any point on the singular hypersurface. Striking a singular point results in (at least temporary) loss of attitude control. Also note the maximum momentum capability {+++} is less than 3H. Per Figure 10, the maximum *singularity-free* momentum capability using $\beta=54.73^o$ is 0.154868. If the skew angle were increased to ninety degrees, *singularity-free* momentum would be increased to 1.0. That analytical analysis can be reinforced with a heuristic analysis in the context of the momentum space singular hypersurface. Consider the singular hypersurfaces for heuristic, geometric observations.

Figure 13 Heuristic skew angle optimization.

Increasing β for a 3/4 CMG skewed array. β was varied in 5° increments from 0° to 90° identifying the trend represented here by three primary plots with 3H & 0H singular surface lightened to enable visualization of 1H & 2H singular surfaces: $\beta = 70^o$ presented here.

Previously, it has been established that a skew angle of ninety degrees results in a singularity-free momentum space of 1H for the 3/4 CMG array. Repeating the numerical, heuristic singularity analysis as skew angle increases is very revealing. Displayed in Figure 13-Figure 15 is the singular momentum space for a skew angle of 70, then 80, then 90 degrees. Notice how the 1H & 2H singular surfaces move away from the (0,0,0) momentum point and gradually converge into each other as skew angle increases to ninety degrees. Fewer singular surfaces is obviously beneficial, but the vacancy of the center of the momentum space is marvelous. More increments of skew angle are provided in the appendix, but these three primary increments (70°, 80°, 90°) are sufficient to reveal the trend visually.
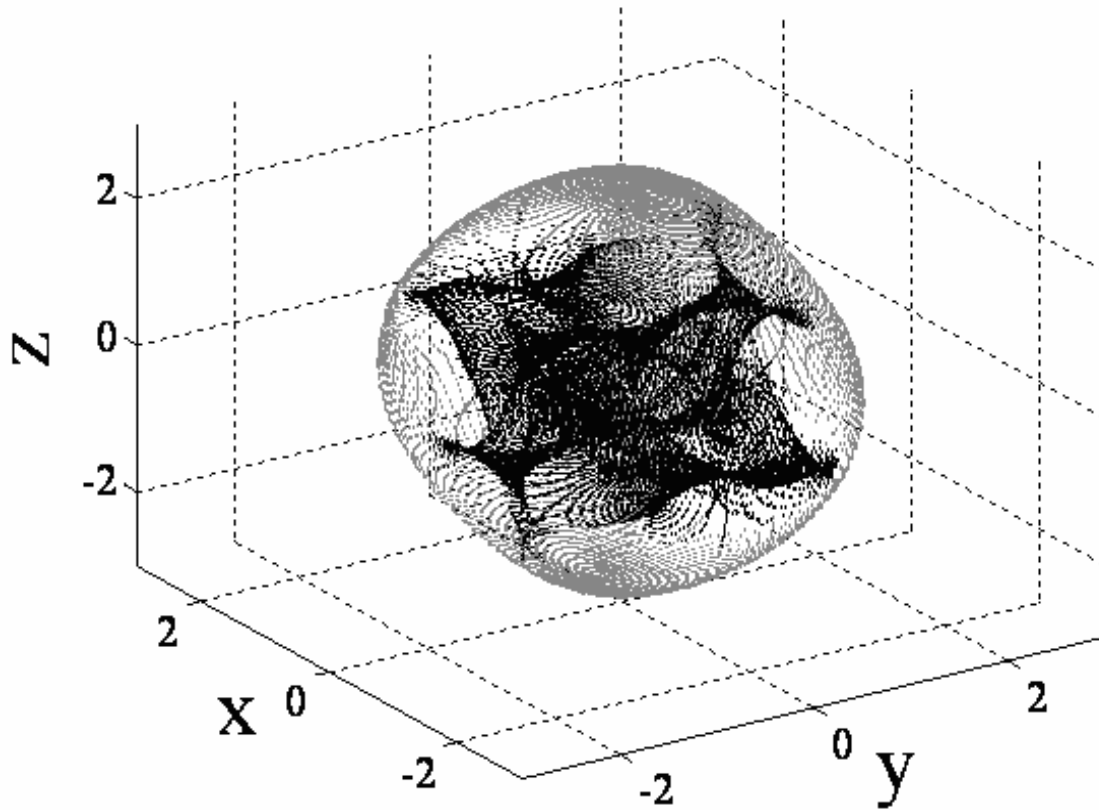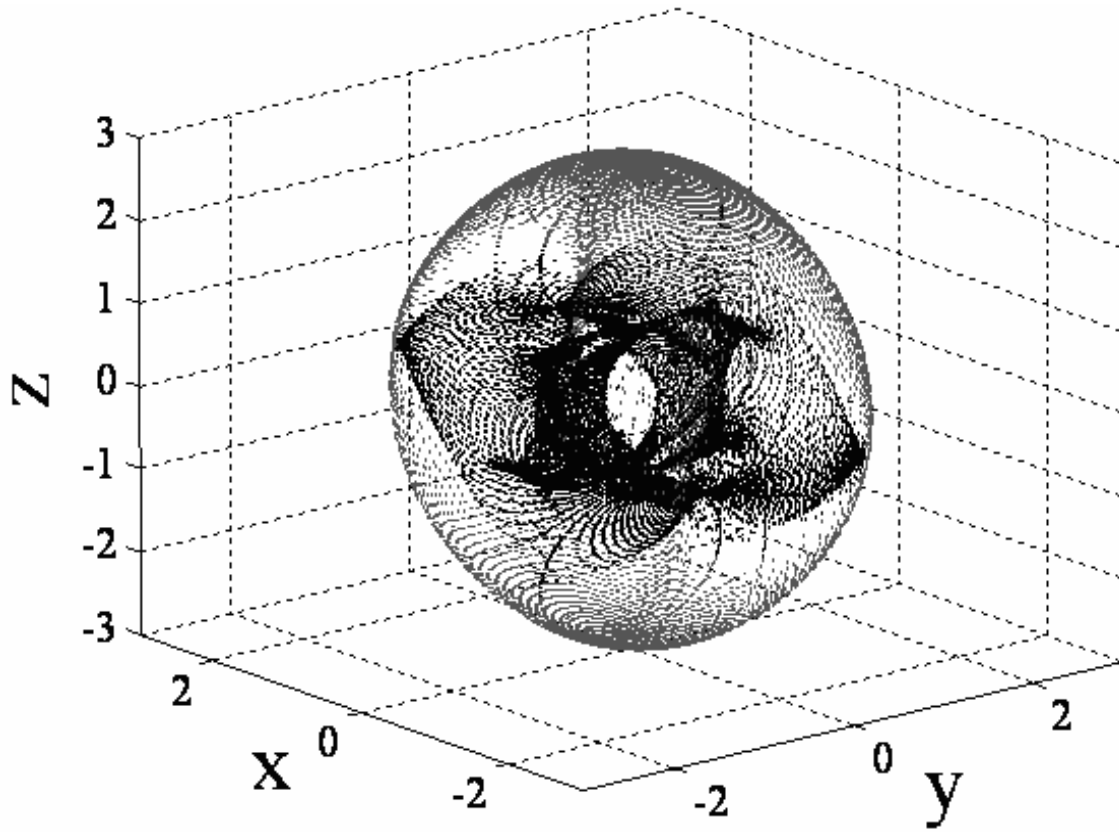

Figure 14 Heuristic skew angle optimization.

Increasing β for a 3/4 CMG skewed array. β was varied in 5° increments from 0° to 90° identifying the trend represented here by three primary plots with 3H & 0H singular surface lightened to enable visualization of 1H & 2H singular surfaces: $β=80^o$ presented here.
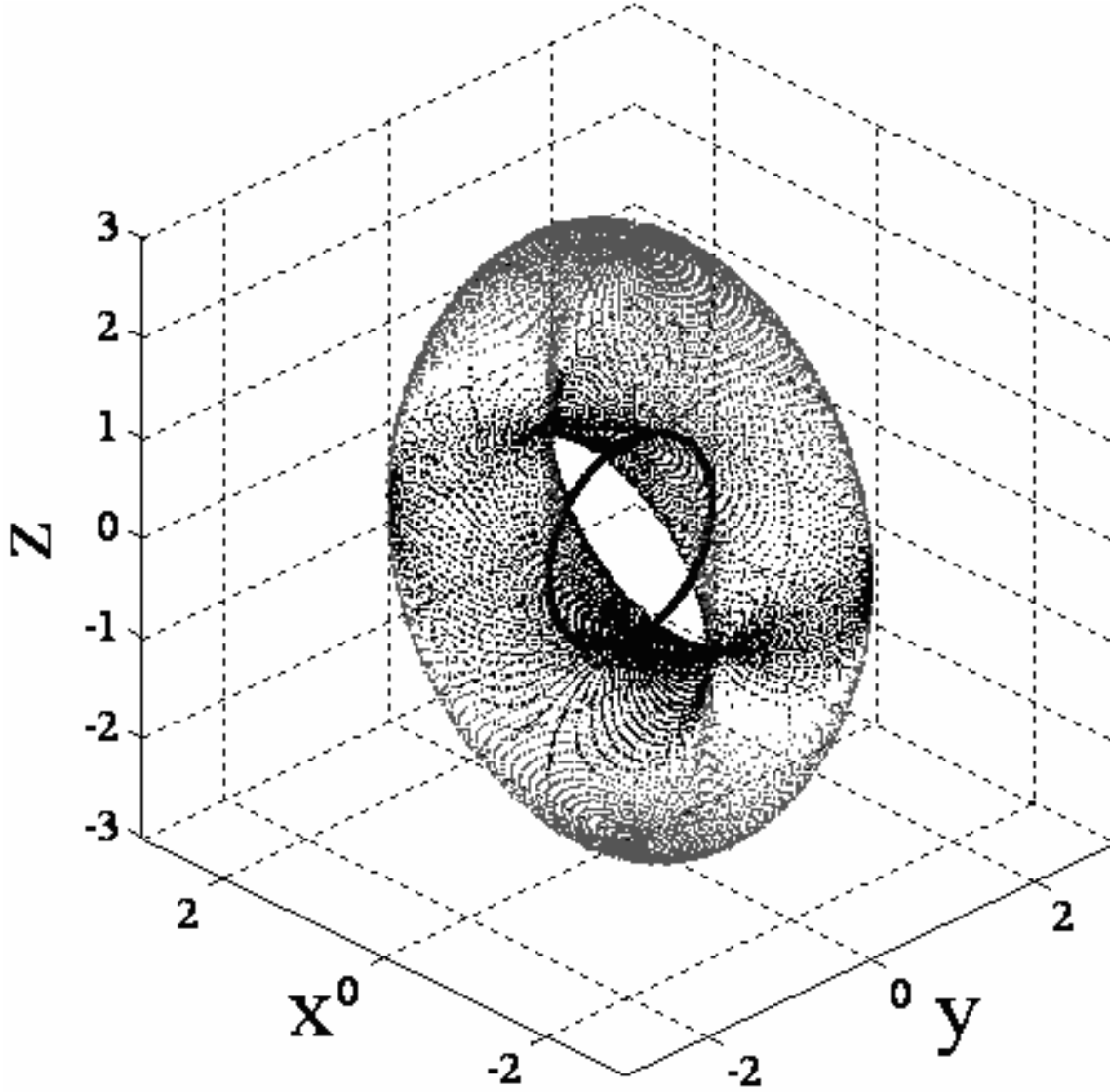
Figure 15 Heuristic skew angle optimization.

Increasing β for a 3/4 CMG skewed array. β was varied in 5° increments from 0° to 90° identifying the trend represented here by three primary plots with 3H & 0H singular surface lightened to enable visualization of 1H & 2H singular surfaces: $\beta = 90^o$ presented here.

The $\beta_i = \beta = 90^o$ result is a nearly-football shaped singularity-free momentum space with divergent ends instead of convergent football ends, minor radius of 1H and a major radius of 2H longitudinally. Experimental verification of this configuration is shown in a later section. Consider that a spacecraft's application may prefer the maximum momentum capability about the yaw ($\hat{\mathbf{z}}$) axis. The nearly-football shaped singularity-free momentum space can be rotated via mixed skew angles.

31

4. Maximized Momentum Reorientation with Mixed Skew Angles

Typically, skewed CMG arrays utilize identical skew angles for each CMG ($\beta_i = \beta$). By using mixed skew angles, the singularity-free "football" shaped space can be reoriented to place the maximum momentum direction in the yaw direction. Six possible momentum reorientations are possible by laying down momentum planes from ninety degrees to zero degrees as displayed in Figure 16 resulting in rotations of the momentum space depicted respectively in the following order per Table 1.

β_1	β_2	β_3
0°	90°	90°
90°	**0°**	**90°**
90°	90°	0°
0°	0°	90°
0°	90°	0°
90°	0°	0°

Table 1 Mixed skew angle combinations.

Six possible combinations of mixed skew angles laying one or two momentum cutting planes from 0° to 90°. Corresponding singular hypersurfaces are depicted in respective order in Figure 16.

Notice that three options for mixed skew angles result in the original momentum space rotated about $\hat{\mathbf{z}}$ such that $\hat{\mathbf{x}} \leftrightarrow \hat{\mathbf{y}}$, while two other options generate spherical momentum space filled with significant internal singularities. Notice the center of the momentum space is clogged with singular surfaces such that those two figures are blackened in the center. Our difficulty seeing the center is indicative of difficulties steering a momentum vector through that space without striking a singular surface for those two mixed skew angle combinations.
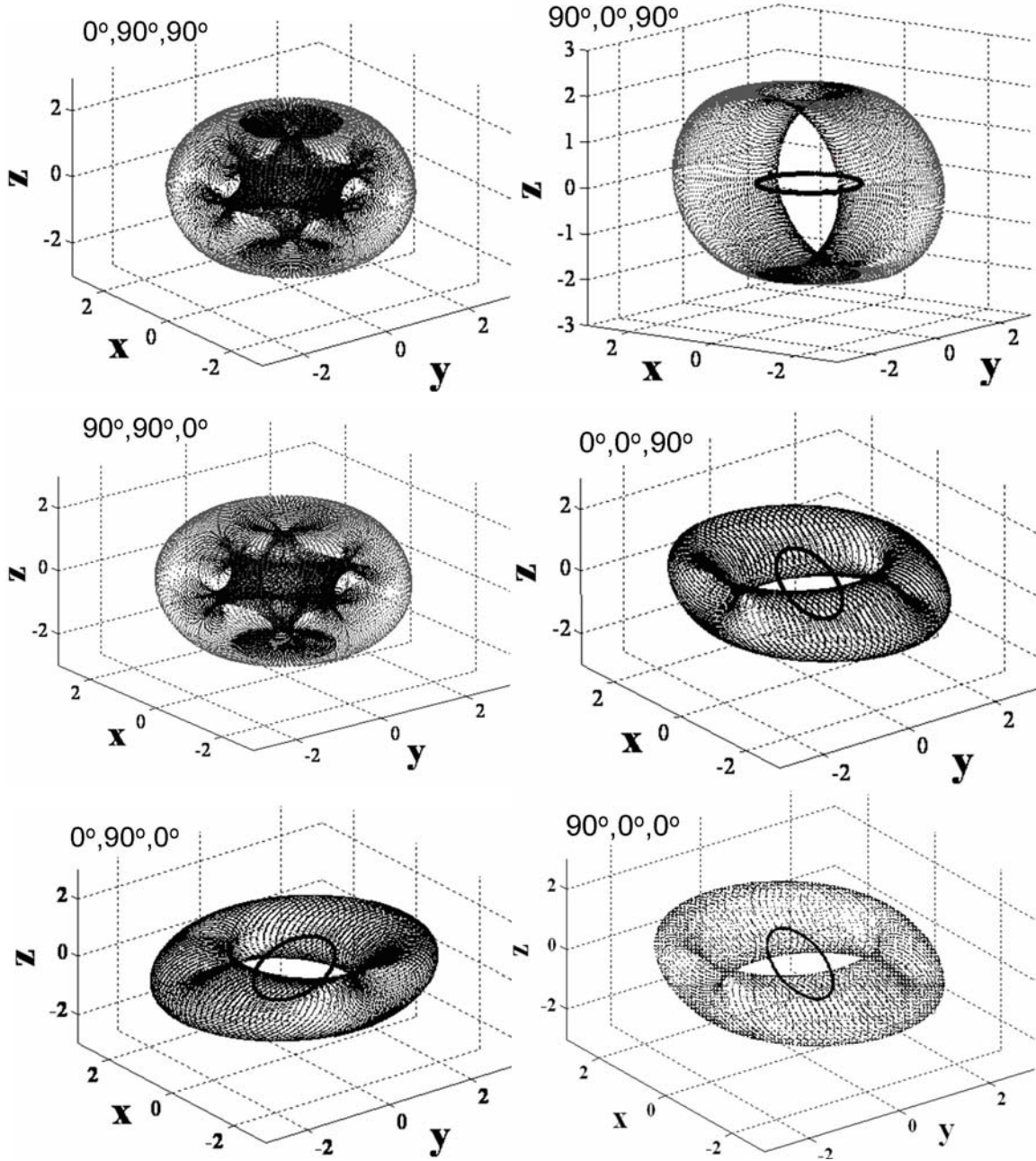
Figure 16 Mixed skew angle singular surfaces.

Singular hypersurfaces resulting from 6 possible combinations of mixed skew angles. Singular surfaces correspond to respective mixed skew angles per Table 1.

One successful reorientation $\{\beta_1,\beta_2,\beta_3\}=\{90^\circ,0^\circ,90^\circ\}$ is accomplished by simply sliding the second CMG from 90° to 0° resulting in yaw momentum maximization with the familiar internal singularity structure. Figure 17 depicts a 3/4 CMG array skewed at mixed skew angles $\beta_1=90^\circ$, $\beta_2=0^\circ$, $\beta_3=90^\circ$. CMG trajectories typically begin from zero

momentum states and $\{h_x, h_y, h_z\} = \{0,0,0\}$ is obviously one such state. Trajectories originating at $\{h_x, h_y, h_z\} = \{0,0,0\}$ have 1H spherical momentum capability and 2H momentum capability about yaw ($\hat{\mathbf{z}}$) singularity-free. Momentum trajectories that are initiated from points near (0,0,2) can traverse to (0,0,-2) resulting in -4H being stored in the CMG array producing +4H momentum change imparted to the spacecraft about yaw singularity free.
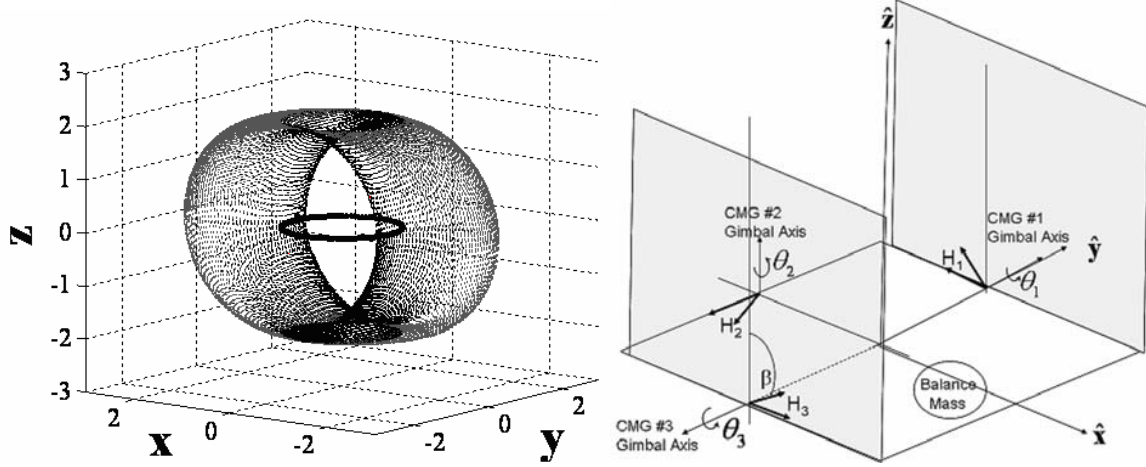
Figure 17 CONTRIBUTION #2: Momentum rotation with mixed skew angles. $\{\beta_1, \beta_2, \beta_3\} = \{90^O, 0^O, 90^O\}$ mixed skew angle momentum hypersurface and cutting planes depicted for a 3/4 CMG skewed array.

5.   Singularity Avoidance with Generalized SR Inverse

References [17],[23] use a modified form of the pseudoinverse to invert the [**A**] matrix. The pseudoinverse is typically used for the over-determined problem of 4 CMGs, but remains applicable to the determined problem of 3 CMGs, since the pseudoinverse is equivalent to the regular inverse for the determined problem. The modified pseudoinverse is called the Generalized Singularity-Robust Pseudoinverse (**A**[#]) according to:

$$\left[A^{\#}\right] = A^T \left(AA^T + \lambda I\right)^{-1} \tag{14}$$

Where λ is a positive scale factor automatically adjusted based on the det[**A**]. As det[**A**] approaches a singularity ($\det[A] \to 0$) λ is adjusted to artificially add components to

34

[**A**] to avoid singular inversion. Where $m = \sqrt{\det(AA^T)}$, using small constants for λ_o and m_o, the relation is as follows.

$$\lambda = \begin{cases} \lambda_0 (1 - m/m_o)^2 & m < m_o \\ 0 & m \geq m_o \end{cases} \tag{15}$$

Alternatively, a small constant may simply be used for λ. The basic point of the algorithm is to alter [**A**] such that singularity is avoided. SR Inverse is amongst the approaches for CMG singularity avoidance that modify the [**A**] matrix itself to make it invertible without singularities and will be attempted experimentally in this thesis. Note that increased tracking error is guaranteed, since we are adding arbitrary commands to avoid loss of attitude control due to singularities. Military spacecraft require fine pointing, an alternative approach that can follow the desired momentum trajectory despite singularities is appropriate. Consider readdressing the most fundamental mathematical step: the combination of the three coupled equations of motion into a system of equations represented in matrix form.

6. Singularity Reduction via Decoupled Control Steering

In this section, we derive a strategy dubbed decoupled control where we take advantage of the simplifications that arise from the optimum singularity free skew angle, $\beta = 90^o$. Substituting the [**A**] matrix with $\beta = 90^o$ into equation 2 yields:

$$\begin{Bmatrix} \dot{\theta}_1 \\ \dot{\theta}_2 \\ \dot{\theta}_3 \end{Bmatrix} = \begin{bmatrix} \sin\theta_1 & 0 & -\sin\theta_3 \\ 0 & \sin\theta_2 & 0 \\ \cos\theta_1 & \cos\theta_2 & \cos\theta_3 \end{bmatrix}^{-1} \begin{Bmatrix} \dot{h}_x \\ \dot{h}_Y \\ \dot{h}_Z \end{Bmatrix} \tag{16}$$

$$\Downarrow$$

$$\begin{Bmatrix} \dot{\theta}_1 \\ \dot{\theta}_2 \\ \dot{\theta}_3 \end{Bmatrix} = \begin{bmatrix} \dfrac{\cos\theta_3}{\cos\theta_1\sin\theta_3 + \sin\theta_1\cos\theta_3} & \dfrac{-\sin\theta_3}{(\cos\theta_1\sin\theta_3 + \sin\theta_1\cos\theta_3)\tan\theta_2} & \dfrac{\sin\theta_3}{\cos\theta_1\sin\theta_3 + \sin\theta_1\cos\theta_3} \\ 0 & \dfrac{1}{\sin\theta_2} & 0 \\ \dfrac{-\cos\theta_1}{\cos\theta_1\sin\theta_3 + \sin\theta_1\cos\theta_3} & \dfrac{-\sin\theta_1}{(\cos\theta_1\sin\theta_3 + \sin\theta_1\cos\theta_3)\tan\theta_2} & \dfrac{\sin\theta_1}{\cos\theta_1\sin\theta_3 + \sin\theta_1\cos\theta_3} \end{bmatrix} \begin{Bmatrix} \dot{h}_x \\ \dot{h}_Y \\ \dot{h}_Z \end{Bmatrix} \tag{17}$$

35

Note that y-momentum change equation has become decoupled from the x & z equations. Pitch momentum is determined completely by gimbal #2. The pitch equation may be separated from the matrix system of equations. The benefit is the elimination of singular gimbal commands for CMGs that are not in geometrically singular gimbal angle positions. Consider what happens if the first & third CMGs enter a combination of gimbal angles that satisfy $\cos\theta_1\sin\theta_3 + \sin\theta_1\cos\theta_3 = 0$. This would not result in singular commands to CMG gimbal # 2. CMG gimbal #2 would receive the following command:

$$\dot{\theta}_2 = \frac{1}{\sin\theta_2}\dot{h}_Y \tag{18}$$

The CMG would operate normally per it's decoupled steering logic.

$$\dot{\theta}_1 = \frac{\cos\theta_3}{\cos\theta_1\sin\theta_3 + \sin\theta_1\cos\theta_3}\dot{h}_x + \frac{-\sin\theta_3}{(\cos\theta_1\sin\theta_3 + \sin\theta_1\cos\theta_3)\tan\theta_2}\dot{h}_y + \frac{\sin\theta_3}{\cos\theta_1\sin\theta_3 + \sin\theta_1\cos\theta_3}\dot{h}_z$$

$$\dot{\theta}_2 = \frac{1}{\sin\theta_2}\dot{h}_Y$$

$$\dot{\theta}_3 = \frac{-\cos\theta_1}{\cos\theta_1\sin\theta_3 + \sin\theta_1\cos\theta_3}\dot{h}_x + \frac{-\sin\theta_1}{(\cos\theta_1\sin\theta_3 + \sin\theta_1\cos\theta_3)\tan\theta_2}\dot{h}_y + \frac{\sin\theta_1}{\cos\theta_1\sin\theta_3 + \sin\theta_1\cos\theta_3}\dot{h}_Z$$

Figure 18 CONTRIBUTION #3: Decoupled control steering commands.

7. Singularity Reduction Simulation

Large yaw maneuvers were simulated using typical coupled control and compared to the proposed decoupled control strategy. Firstly a $+50^\circ$ yaw maneuver is followed immediately by -50° yaw maneuver then regulation at zero. The results of both methods are displayed in Figure 19. Notice the coupled implementation of the Moore-Penrose pseudoinverse results in dramatic pitch commands each time the momentum trajectory strikes the singular surface.

On the contrary, notice how decoupled control smoothly traverses the singular surface with no pitch errors. Since analysis and simulation both indicate the proposed decoupled control technique should work, experimental verification was performed on free-floating spacecraft simulator (Figure 68-Figure 71).
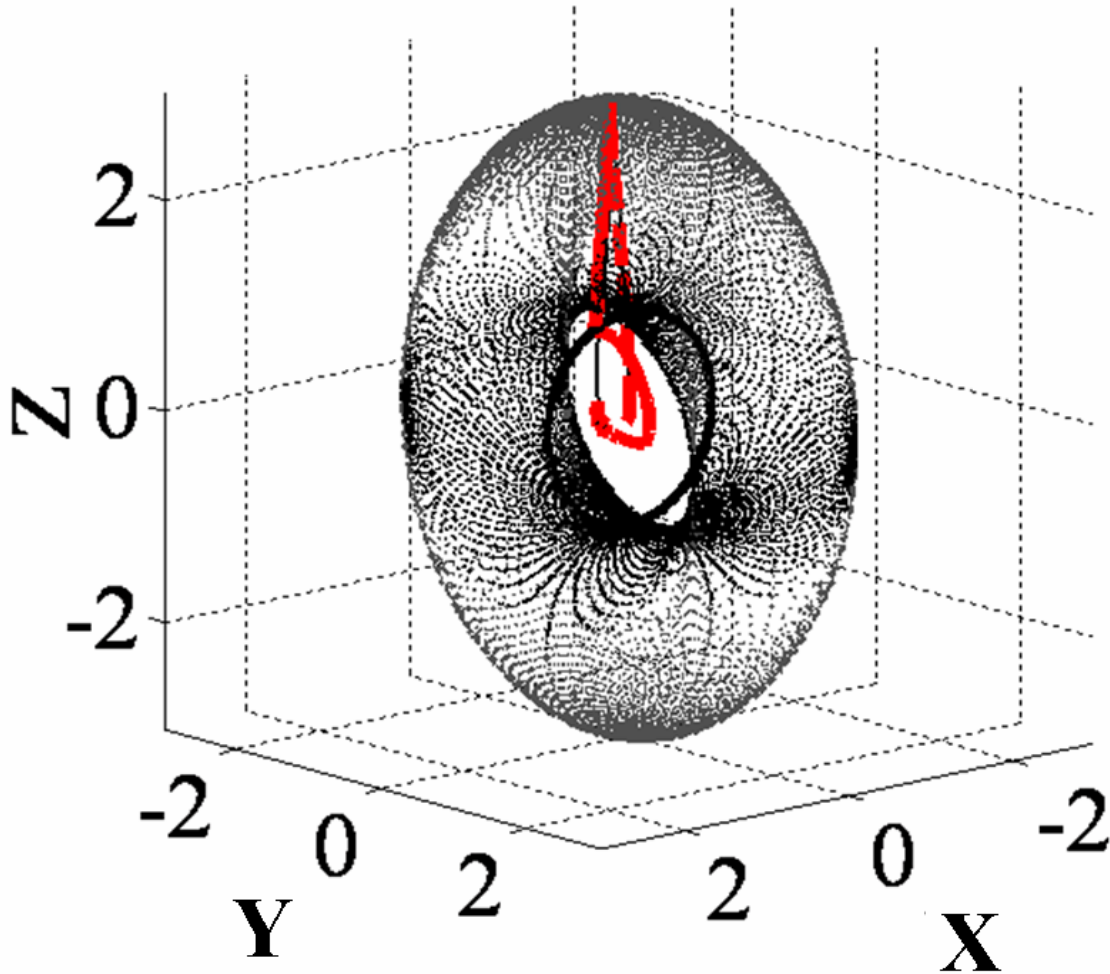
Figure 19 SIMULATION: Decoupled control steering.

Comparison of typical coupled control (thick-dashed) with to decoupled control (thin line). Notice small roll (x) errors each time the trajectory passes through the "doughnut" singularity surface and huge roll error when trajectory strikes the "ring" singular surface.

8.   Singularity Penetration Algorithm

Next, consider that singularity reduction as presented is restricted to geometric configurations (CMG skew angles) that permit control decoupling. Instead consider penetrating the singular surface without loss of attitude control. Attitude control is lost when the closed loop control law tries to invert a rank deficient [**A**] matrix. When the determinant reaches a critical low absolute value, the closed loop law may augmented to include a unit-delay activated at this critically low value. As the momentum trajectory approaches the singularity, increasingly high gimbal rates are required. When the unit-delay is switched on, the previous valid (non-singular) value is held until the singularity

has been penetrated. Then, the nominal closed-loop control (inversion of [**A**]) continues to control the spacecraft. In essence, we are "ignoring" the anomalous transient as we pass through the singularity, instead holding the last valid steering command value. Henceforth, the technique is referred to as SPUD: **s**ingularity **p**enetration w/ **u**nit **d**elay.
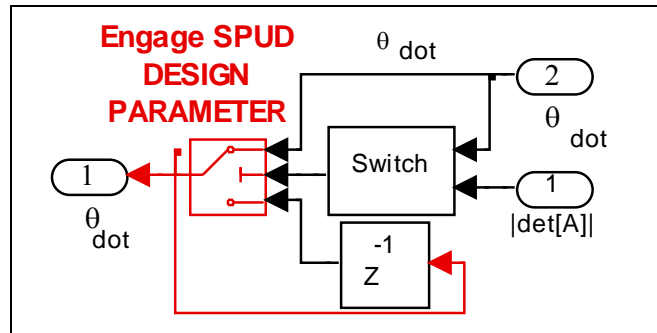
Figure 20 CONTRIBUTION #4: Singularity penetration algorithm.

9. Singularity Penetration Simulations

The following plots depict results of simulated 50° yaw maneuvers with and without SPUD permitting a longer maneuver time to reduce momentum to near 1H complicating singularity transgression. The fully coupled control is implemented here without the decoupled control scheme used earlier to reduce singularities. The simulations indicate that SPUD is effective even without reduced singularities via decoupled control, thus SPUD is more generically effective for other geometric configurations (CMG skew angles).

38

Figure 21 SIMULATION: Singularity penetration Euler angles.

Comparison of Euler angles for 50° yaw maneuver with & without singularity penetration with unit delay (SPUD);

Figure 22 SIMULATION: Singularity penetration tracking errors.

 Comparison of Euler angle tracking errors for 50° yaw maneuver with & without singularity penetration with unit delay (SPUD);

39

Figure 23 SIMULATION: Singularity penetration.

Comparison of det[A] and normalized momentum magnitude for 50° yaw maneuver with & without singularity penetration with unit delay (SPUD)

Figure 24 SIMULATION: Singularity penetration.

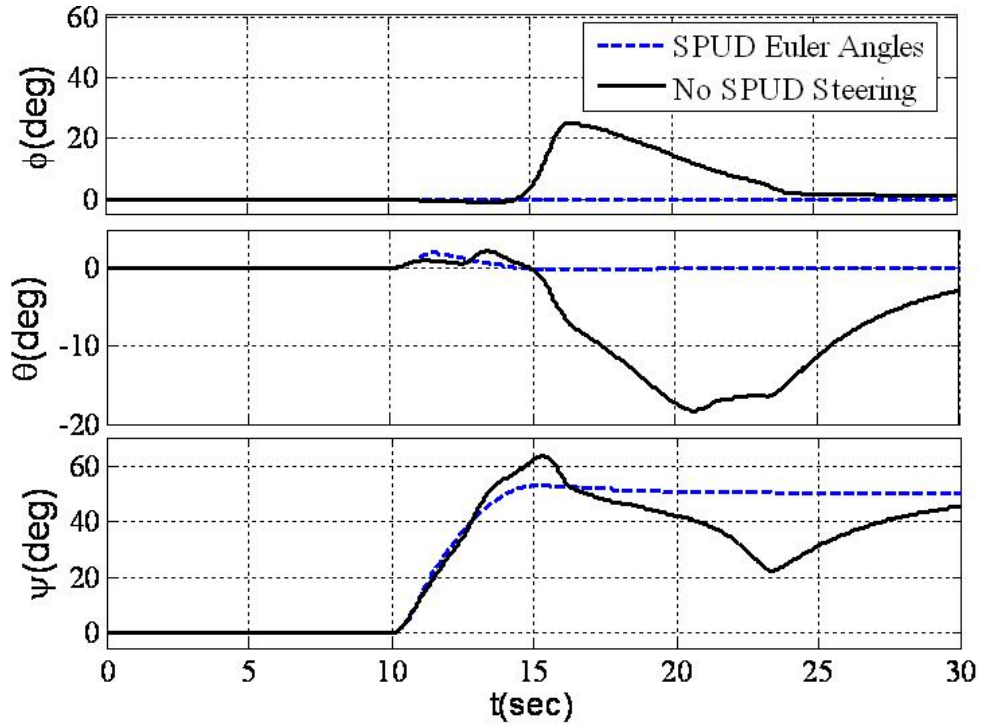Comparison of gimbal rates for 50° yaw maneuver with & without singularity penetration with unit delay
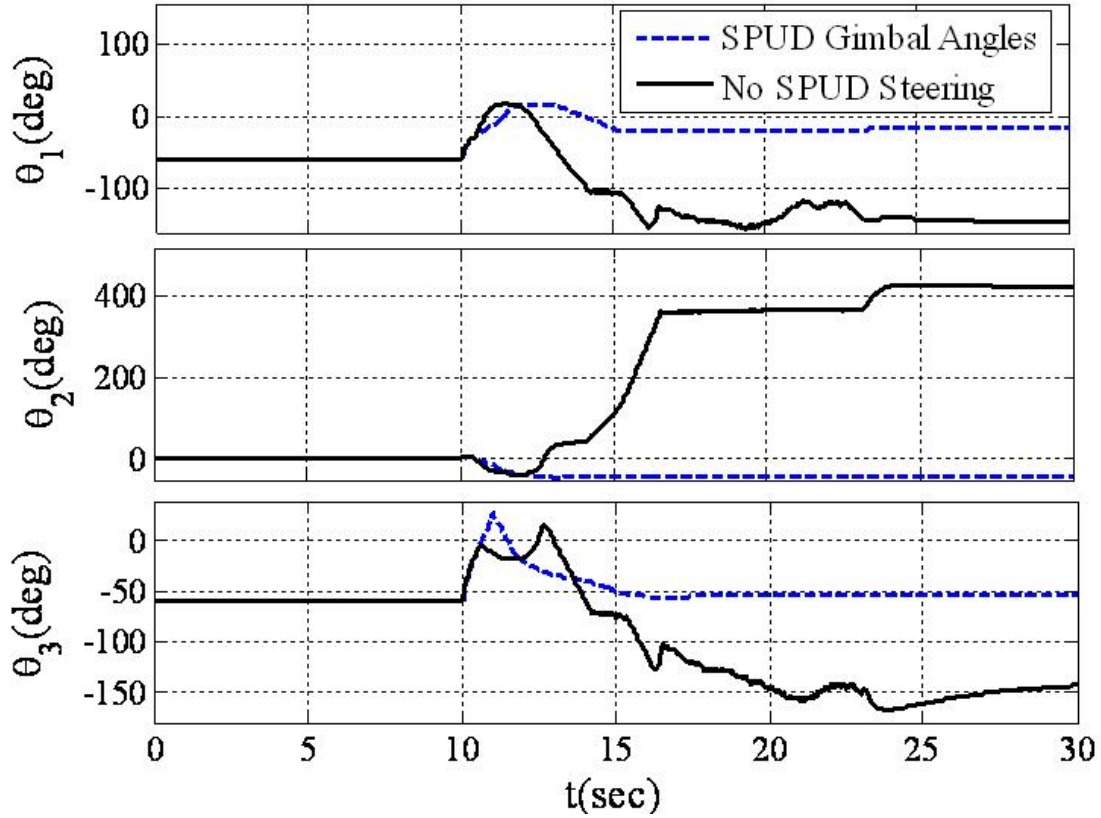
Figure 25 SIMULATION: Singularity penetration.

Comparison of gimbal angles for 50° yaw maneuver with & without singularity penetration with unit delay.

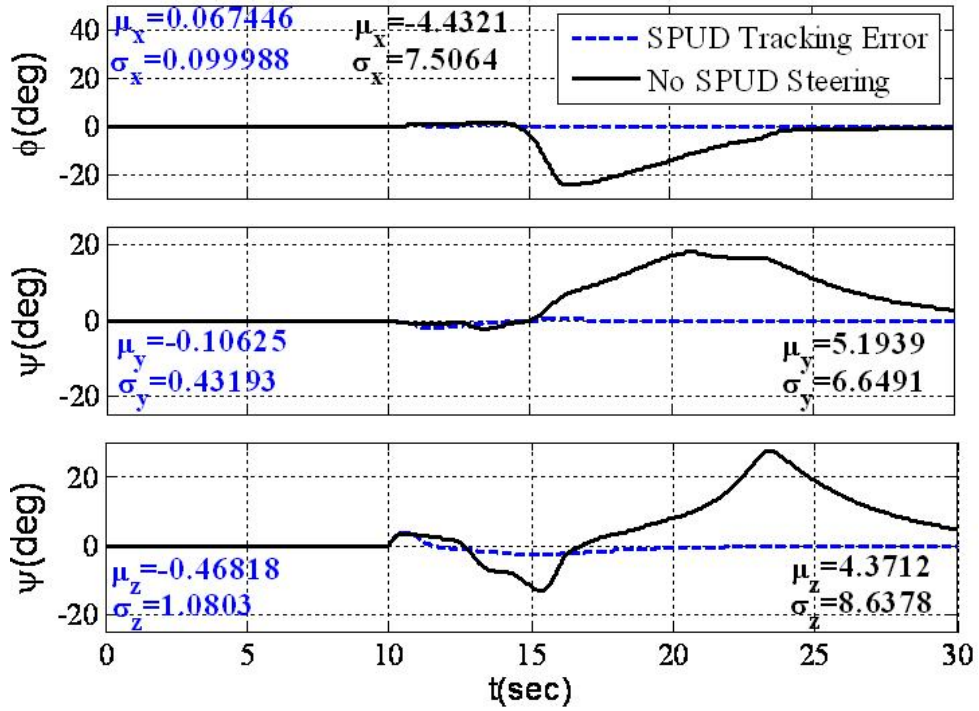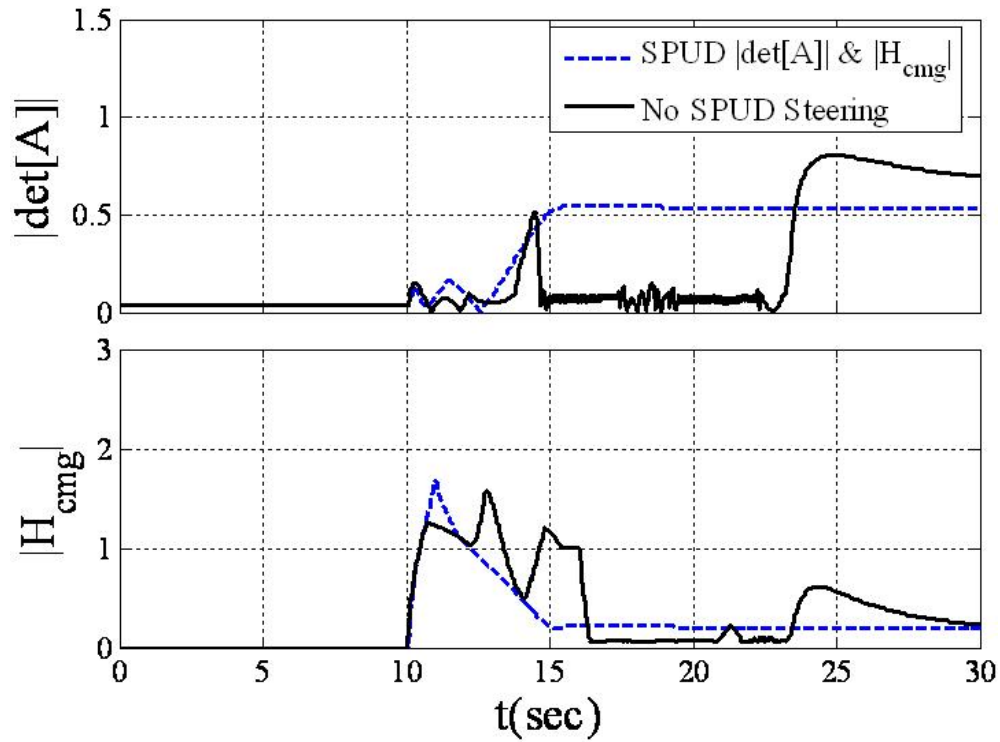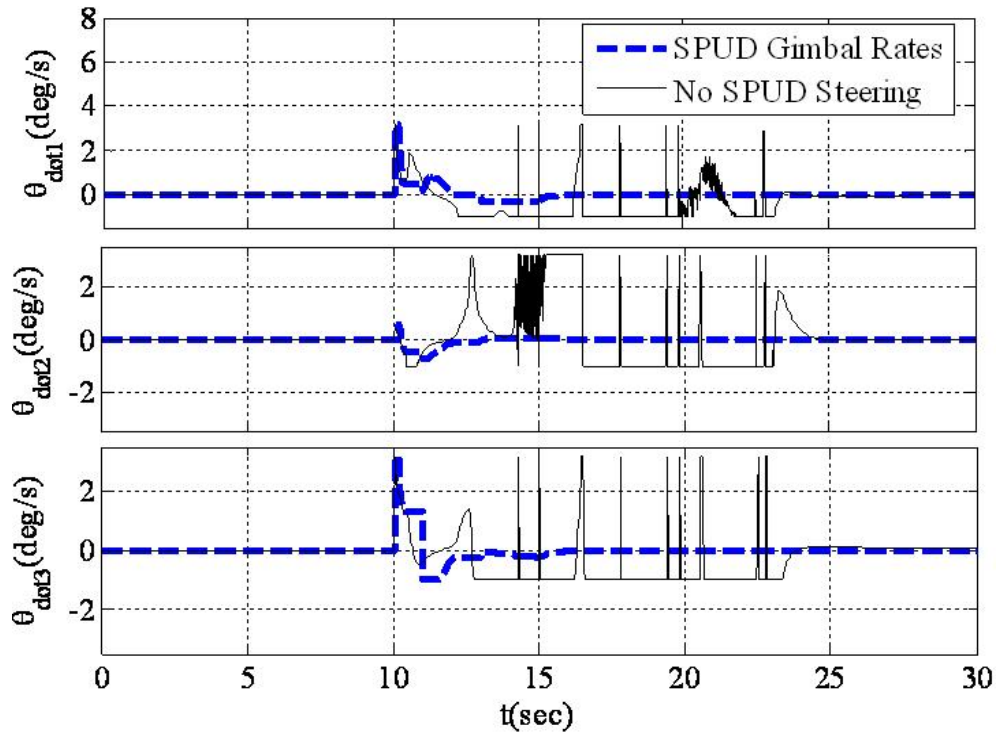In the simulations, singularity penetration with unit delay was engaged when det[**A**]=0.01. This was selected based on previous experimental experience. Instead, consider raising the determinant value and adding a gimbal rate saturation criteria. For all intensive purposes, you are singular at that point. This helps smoothly transit singularities making the entire momentum space accessible for rapid target acquisitions slew maneuvers. Following target acquisitions, fine tracking must be maintained to perform the military mission.

D.   TARGET TRACKING

1.   Introduction

Target tracking from a low or mid altitude earth orbit is complicated. The earth is moving underneath the satellite. Despite this rapid motion, the operational mission demands the spacecraft maintain three-axis attitude control while maneuvering to track the target point on the earth noting the target may be moving uncooperatively trying to

avoid detection. Theoretically, if a spacecraft inertia [**J**] is known exactly, an ideal feedforward command τ_{command} for an inertial rotation (with acceleration $\{\ddot{\mathbf{x}}\}$), could be formulated per Newton-Euler ($\tau_{command} = [\mathbf{J}]\{\ddot{\mathbf{x}}\}$) executing a perfect target tracking maneuver with no target tracking errors. Real world considerations (e.g. noise, disturbances, un-modeled effects) typically generate tracking errors, so this classical feedforward command is typically augmented with a feedback command to eliminate the tracking errors after they have been incurred.

For the case of un-modeled inertia errors, the predominant command is the classical feedforward with feedback augmentation as a secondary but critically important component. Fuel expenditure for spacecraft orbital maintenance maneuvers are amongst the reasons inertia is not exactly known on-orbit. The ground controller designs attitude commands for an assumed or estimated inertia $\hat{\mathbf{J}}$. If the actual inertia were greater than estimated $\|\mathbf{J}\| > \|\hat{\mathbf{J}}\|$, the classical feedforward command will result in inadequate torque to complete the maneuver. On the contrary if $\|\mathbf{J}\| < \|\hat{\mathbf{J}}\|$ the spacecraft maneuver would exceed the desired maneuver. Both instances result in tracking error that is corrected by the feedback control components *after the errors have been incurred and measured*.
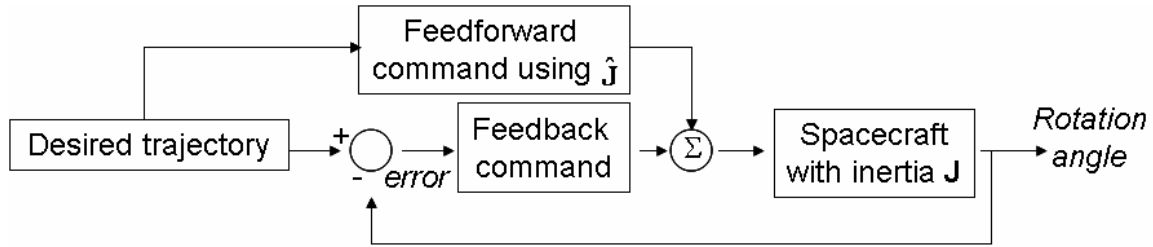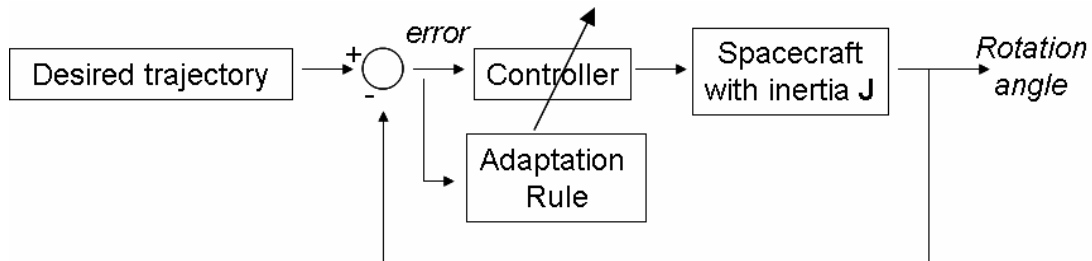

Figure 26 Spacecraft command relationships.

Figure 27 *One* kind of direct adaptive spacecraft command relationship.

42

Please note in Figure 26-Figure 27 are generic with regard to spacecraft actuators. While CMGs have been assumed so far, the developments presented here do not include any actuator dynamics. It is presumed that whatever control is generated by a controller the actuator will accomplish the commanded control.

Slotine (Ref [43], [44]) introduced an a nonlinear adaptive controller that modifies both feedforward and feedback control signals with inertia estimation and also by utilizing a reference trajectory which adds/subtracts commanded velocity to account for position error. This method of adaptive control is referred to as indirect adaptive control. Control is indirectly adapted by *explicitly estimating* unknown parameters that are used to formulate the control. Direct adaptive control techniques reparameterize the control eliminating the explicit estimation of plant parameters and directly adapting the control signal itself. In the case of Slotine's controller, the estimated plant parameters are in the control, so either term (direct/indirect) may arguably be used. For this paper, Slotine's approach will be referred to as indirect adaptive control. Slotine's indirect adaptive control technique was compared favorably to feedback control alone (not combined feedforward/feedback as is typically done) [44]. One particular weakness was that one single matrix in the adaptive controller requires several pages to express leading to unwieldy and unacceptable computations. Subsequently, Fossen modified Slotine's approach to solve the issue of unwieldy calculations. By determining the reference trajectory in the body coordinate frame versus the inertial coordinate frame as Slotine did, Fossen derived a substantial simplification. The method was not derived for spacecraft *rotational maneuvers*, nor were simulations or experimental verification performed.
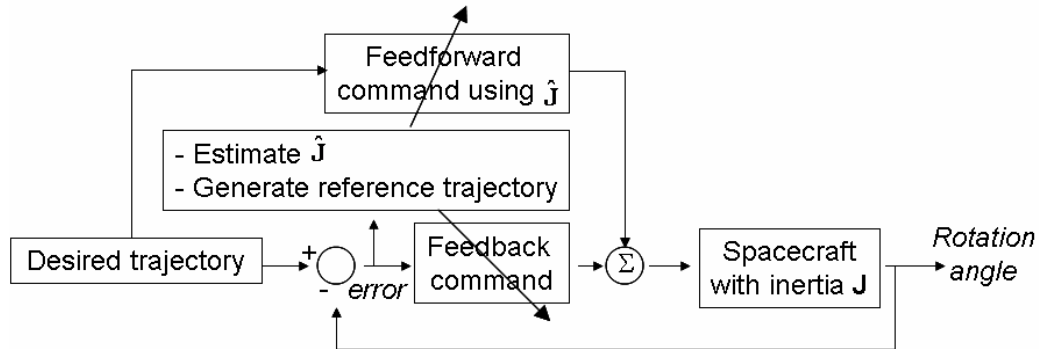

Figure 28 Slotine/Fossen indirect adaptive spacecraft command relationships.

Substantial contributions in this chapter of the thesis may be summarized.

1.   Derive the 9-parameter, Slotine/Fossen approach for 3-dimensional *rotational spacecraft control* including comparison versus feedforward + feedback control in simulation with experimental verification (all three absent in the literature).

2.   Reduced-order estimation (6-parameter) will be shown to be equally effective utilizing the [Slotine/Fossen] approach.

3.   Further estimation reduction (3-parameter) will be suggested with some simplifying assumptions (estimate only diagonal terms of inertia matrix).

4.   A new, improved indirect adaptive control technique will be introduced utilizing adaptive feedforward control with a reference trajectory as in [Slotine/Fossen], but retaining simple PD feedback control.

5.   Finally, it will be shown that estimation can be eliminated altogether without significantly sacrificing the gained performance increases.

Since the proposed indirect adaptive control technique is inspired and compared to the techniques in the recent literature (Slotine/Fossen), these techniques are evaluated first. With an understanding of the current methods, the proposed techniques are easily understood as simplified approaches which can further improve performance.

2.   Slotine/Fossen Approach

Recall equation 2 repeated here for clarity in terms of non-specific body coordinate **q** assumes no particular control actuator. This equation of motion may be written by various methods (Newton-Euler, Lagrange, Kane's, momentum, etc.) as follows:

$$[\mathbf{J}]\{\ddot{q}\}+[\mathbf{C}]\{\dot{q}\}=\{\boldsymbol{\tau}\} \tag{19}$$

where [**J**] is the inertia matrix, [**C**] is the matrix relating the motion rates to the Coriolis & centripetal forces, $\boldsymbol{\tau}$ is the sum of external torques and **q** is the body coordinates (e.g. roll ϕ, pitch θ, yaw ψ). The subscript "B" indicates the expression in the body coordinate

frame (duplicative when using **q**, but sometimes included for clarity). The body coordinates may be transformed into inertial coordinates via the transformation matrix $[\mathbf{R}]_{b2i}$.

$$\{\dot{x}\} = [\mathbf{R}]_{B2i}\{\dot{q}\} \tag{20}$$

Similarly, we may define a reference trajectory *in the body coordinates*:

$$\{\dot{x}_r\} = [\mathbf{R}]_{B2i}\{\dot{q}_r\}. \tag{21}$$

Rewriting the transformation and differentiating:

$$\{\dot{q}_r\} = [\mathbf{R}]^{-1}\{\dot{x}_r\} \tag{22}$$

$$\{\ddot{q}_r\} = [\mathbf{R}]^{-1}\{\ddot{x}_r\} - [\mathbf{R}]^{-1}[\dot{\mathbf{R}}][\mathbf{R}]^{-1}\{\dot{x}_r\} \tag{23}$$

We may use these quantities to define a control in terms of estimates and the reference trajectory per Slotine using a combined error measure $s = \dot{\mathbf{q}} - \dot{\mathbf{q}}_r$.

$$[\mathbf{R}]^T \underbrace{\left(\left[\hat{\mathbf{J}}^*\right]\{\ddot{x}_r\} + \left[\hat{\mathbf{C}}^*\right]\{\dot{x}_r\} \right)}_{\Phi^*(x,x,\ddot{x}_r,\ddot{x}_r)\Theta} - [\mathbf{R}]^T \mathbf{K}_d\{\mathbf{s}\} = [\mathbf{R}]^{-T}\{\tau\} \tag{24}$$

Slotine uses the linear regression model $[\Phi^*]\{\Theta\}$ to define an equivalent system based on parameter estimates:

$$\Phi^*(x,\dot{x},\dot{x}_r,\ddot{x}_r) \underbrace{\Theta}_{\text{unknown}} = \underbrace{\Phi^*(x,\dot{x},\dot{x}_r,\ddot{x}_r)}_{\text{measured}} \underbrace{\hat{\Theta}}_{\text{estimated}} + \underbrace{\text{error}}_{\Phi^*\tilde{\Theta}}. \tag{25}$$

The estimates $\hat{\Theta}$ are adapted using an adaption rule that makes the closed loop system stable in the Lyapunov sense. The regression model is then used in the control, which is where the complication arises. The $\Phi^*(x,\dot{x},\dot{x}_r,\ddot{x}_r)$ matrix of "knowns" occupies several pages and is used *at each time* step to formulate the adapted control signal making the method computationally impractical. [Fossen] on the other hand formulates the regression model in the body coordinates eliminated the complications seen above with the numerous multiplications with the coordinate transformation matrix [**R**]. Picking up from [Slotine]'s method above, we can simply express the regression model *including* the transformation matrix.

$$[\mathbf{R}]^T \left[\mathbf{J}^* \right] \{\ddot{x}_r\}_i + [\mathbf{R}]^T \left[\mathbf{C}^* \right] \{\dot{x}_r\}_i = \left[[\mathbf{J}]\{\ddot{\mathbf{q}}_r\} + [\mathbf{C}]\{\dot{\mathbf{q}}_r\} \right] = \Phi(x, \dot{q}, \dot{q}_r, \ddot{q}_r)\Theta \qquad (26)$$

Note the $\Phi(x, \dot{q}, \dot{q}_r, \ddot{q}_r)$ "measured" matrix has no asterisk. Fossen similarly suggests adaptive dynamics using an estimate of the regression vector.

$$\Phi(q, \dot{q}, \dot{q}_r, \ddot{q}_r)\theta = \underbrace{\Phi(q, \dot{q}, \dot{q}_r, \ddot{q}_r)}_{\text{measured}} \underbrace{\hat{\Theta}}_{\text{unknowns}} + \text{error} \qquad (27)$$

In order to do this, we must define the reference trajectory. The modifications to the overall feedforward control strategy may be embodied in these two venues: 1) estimate/adapt estimates of inertia in the regression model above, and 2) choose a reference trajectory that addresses system lead/lag when applying the assumed control to a spacecraft with modeling errors, disturbances and noise.

a.   *Reference Trajectory*

Define the reference trajectory such that the control helps the spacecraft "catch up" to the commanded trajectory. If the spacecraft is actually more massive than modeled, it needs a little extra control to achieve tracking than will be provided by classical feedforward control. If the spacecraft is actually less massive than modeled, the control must be reduced so as not to overshoot the commanded trajectory. Consider defining the reference trajectory as follows.

$$\begin{aligned}
\dot{q}_r &= \dot{q}_d - \lambda(q - q_d) \\
\ddot{q}_r &= \ddot{q}_d - \lambda(\dot{q} - \dot{q}_d)
\end{aligned} \qquad (28)$$

Note we have scaled the reference acceleration and velocity to subtract the velocity and position error respectively scaled by a positive constant, λ. Notice the example in Figure 29. The reference trajectory sometimes leads the desired trajectory (when the spacecraft is lagging behind the desired). The reference trajectory also sometimes lags the desired trajectory (when the spacecraft is leading the desired trajectory). Accordingly, subsequent sections will evaluate the effectiveness of the reference trajectory where the estimation dynamics are zero. First, let's conclude the derivation by multiplying out the linear regression form so that the reader can have the simple [Fossen] control equation for spacecraft rotational maneuvers.
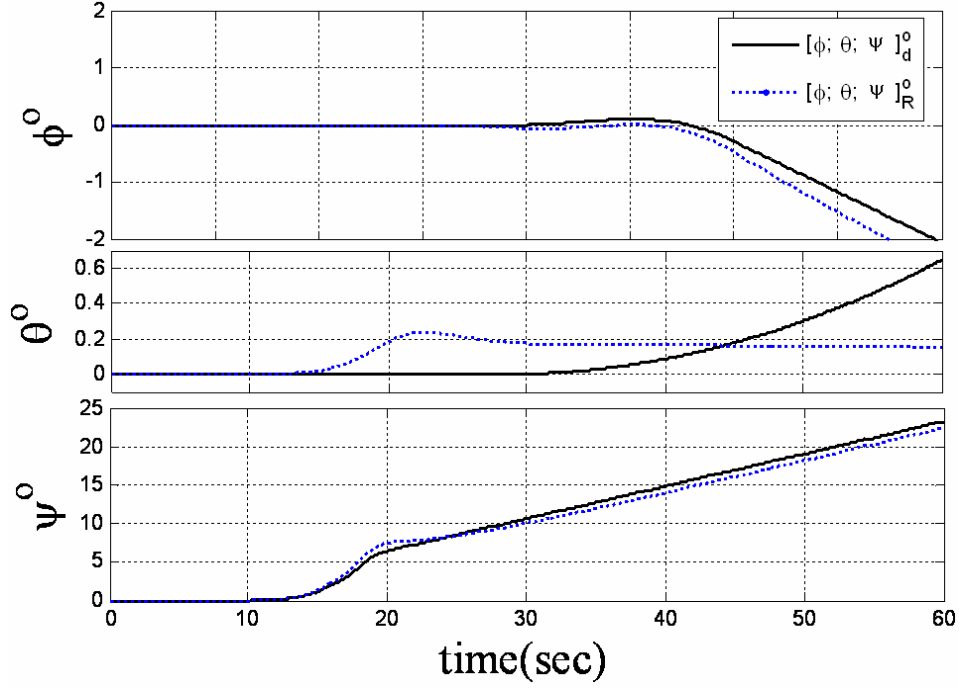
Figure 29 Reference trajectory example.

Reference Trajectory (dotted) compared with desired trajectory (solid). Notice reference sometimes leads and sometimes lags desired trajectory (based on tracking error).

Simplify $[\mathbf{J}]\{\ddot{q}_r\} + [\mathbf{C}]\{\dot{q}_r\} = \{\tau\}_B$ with reference trajectory $\ddot{q}_r = \dot{\omega}_r$ & $\dot{q}_r = \omega_r$:

$$[\mathbf{J}]\{\dot{\omega}_r\} + [\mathbf{C}]\{\omega_r\} = \{\tau\}_B \tag{29}$$

$$[\mathbf{J}]\{\dot{\omega}_r\} = [\mathbf{H}\times]\{\omega_r\} + \{\tau\}_B \tag{30}$$

$$[\mathbf{J}]\{\dot{\omega}_r\} = [\mathbf{J}]\{\omega\}\times\{\omega_r\} + \{\tau\}_B \tag{31}$$

where $[\mathbf{H}\times]$ is the skew symmetric matrix form of the total system momentum vector.

Expand $[\mathbf{J}]\{\dot{\omega}_r\} - [\mathbf{H}\times]\{\omega_r\} = \{\tau\}_B$:

$$\begin{bmatrix} J_{xx} & J_{xy} & J_{xz} \\ J_{yx} & J_{yy} & J_{yz} \\ J_{zx} & J_{zy} & J_{zz} \end{bmatrix} \begin{Bmatrix} \dot{\omega}_x \\ \dot{\omega}_y \\ \dot{\omega}_z \end{Bmatrix}_r - \begin{bmatrix} 0 & -H_z & H_y \\ H_z & 0 & -H_x \\ -H_y & H_x & 0 \end{bmatrix} \begin{Bmatrix} \omega_x \\ \omega_y \\ \omega_z \end{Bmatrix}_r \tag{32}$$

Multiplying out:

47

$$\begin{bmatrix} -H_y\omega_{z_r} + H_z\omega_{y_r} + J_{xx}\dot{\omega}_{x_r} + J_{xy}\dot{\omega}_{y_r} + J_{xz}\dot{\omega}_{z_r} \\ H_x\omega_{z_r} - H_z\omega_{x_r} + J_{yx}\dot{\omega}_{x_r} + J_{yy}\dot{\omega}_{y_r} + J_{yz}\dot{\omega}_{z_r} \\ -H_x\omega_{y_r} + H_y\omega_{x_r} + J_{zx}\dot{\omega}_{x_r} + J_{zy}\dot{\omega}_{y_r} + J_{zz}\dot{\omega}_{z_r} \end{bmatrix} = \begin{Bmatrix} \tau_x \\ \tau_y \\ \tau_z \end{Bmatrix}_B = \{\mathbf{u}_{ff}\}_{ideal} \qquad (33)$$

Let $\theta^T = \{ J_{xx} \quad J_{xy} \quad J_{xz} \quad J_{yy} \quad J_{yz} \quad J_{zz} \quad H_x \quad H_y \quad H_z \}$ assuming

$J_{yx} = J_{xy}$, $J_{zy} = J_{yz}$, $J_{zy} = J_{xz}$ implied $\{\mathbf{u}_{ff}\}_{ideal} = \left[\Phi(\omega_r, \dot{\omega}_r) \right]_{3x9} \{\Theta\}_{9x1}$:

$$u_{ff} = \begin{bmatrix} \dot{\omega}_x & \dot{\omega}_y & \dot{\omega}_z & 0 & 0 & 0 & 0 & -\omega_z & \omega_y \\ 0 & \dot{\omega}_x & 0 & \dot{\omega}_y & \dot{\omega}_z & 0 & \omega_z & 0 & \omega_x \\ 0 & 0 & \dot{\omega}_x & 0 & \dot{\omega}_y & \dot{\omega}_z & -\omega_y & \omega_x & 0 \end{bmatrix}_r \begin{Bmatrix} J_{xx} \\ J_{xy} \\ J_{xz} \\ J_{yy} \\ J_{yz} \\ J_{zz} \\ H_x \\ H_y \\ H_z \end{Bmatrix} \qquad (34)$$

Figure 30 CONTRIBUTION 5: Derived 9-parameter [Fossen] modification of [Slotine].

$$\left[\Phi(\omega_r, \dot{\omega}_r) \right] \{\Theta\} = \Phi_r \hat{\Theta} + \text{error} \qquad (35)$$

This is the derivation of Fossen's modification of Slotine's indirect adaptive feedforward control not currently in the literature (Referred to as *Slotine/Fossen*). Using this regression model, we are free to evaluate the first substantial contribution in this portion of this dissertation. After comparing this approach to classical feedforward and feedback control, this model will be the basis upon which proposed improvements are made.

The dynamics establish the classical feedforward command when the inertia is known and correct. Accordingly, utilize the estimated dynamics for formulate the adapted feedforward command based on estimated inertia. Additionally, feedback control may be added utilizing the reference trajectory in a PD control architecture.

$$\tau = \underbrace{[\Phi_r]\{\hat{\Theta}\}}_{u_{ff}} - \underbrace{\mathbf{R}^T\left[K_d(\dot{x}-\dot{x}_d)+K_p(x-x_d)\right]}_{u_{fb}} \tag{36}$$

Notice this definition of feedback control defines the reference trajectory gain $\lambda = K_p / K_d$. Thus choice of K_p and K_d constrains/defines the reference trajectory. This fact will be utilized later to improve the method.

$$\begin{aligned} u_{fb} &= -K_d(\dot{q}-\dot{q}_r) = -K_d(\dot{q}-\dot{q}_d - \lambda(q-q_d)) \\ &= K_d(\dot{q}-\dot{q}_d) - \underbrace{\lambda K_d}_{K_p}(q-q_d) \end{aligned} \tag{37}$$

Similar to the example in [44], *feedforward* techniques in this study are compared by fixing feedback gains: $K_d = 200\frac{control\ units}{error\ units}$, $\lambda = 1/2 \rightarrow K_p = 100\frac{control\ units}{error\ units}$. This causes a limitation in adaptation of the feedforward torque, since the regression model is formulated using the *reference* trajectory. The proposed technique is to feedback the desired trajectory rather than the reference trajectory. This allows the reference trajectory to be more aggressively used to adapt the feedforward control without effecting the feedback signal. Another way to look at it is fixing the λ for feedback (referred to as λ_{fb}) and allowing a more aggressive feedforward using λ_{ff}.

3.   Derived Reduced Estimation: 6-Parameter Regression ("Derived6")

Recalling $\{\mathbf{H}\}=[\mathbf{J}]\{\omega\}$, substitution into the 9-parameter regression model allows reformulation into the following equivalent 6-parameter regression model.

$$u_{ff} = \begin{bmatrix} \dot{\omega}_{x_r} & \dot{\omega}_{y_r} & \dot{\omega}_{z_r} & -\omega_y\omega_{z_r} & 0 & \omega_z\omega_{y_r} \\ \omega_x\omega_{z_r} & \dot{\omega}_{x_r} & 0 & \dot{\omega}_{y_r} & \dot{\omega}_{z_r} & -\omega_z\omega_{x_r} \\ -\omega_x\omega_{y_r} & 0 & \dot{\omega}_{x_r} & \omega_y\omega_{x_r} & \dot{\omega}_{y_r} & \dot{\omega}_{z_r} \end{bmatrix} \begin{Bmatrix} J_{xx} \\ J_{xy} \\ J_{xz} \\ J_{yy} \\ J_{yz} \\ J_{zz} \end{Bmatrix} \tag{38}$$

Figure 31 CONTRIBUTION 6: Reduction of Fossen's approach to 6-parameters.

49

It is proposed to no longer estimate the rate in the system momentum (since we have rate sensors), and instead estimate *only* the unknown inertia terms. This first proposed adaptive technique (*Proposed6*) utilizes this reduced regression model resulting in analytically identical results with fewer computations. In addition, this technique will be implemented with fixed λ_{fb} and variable λ_{ff} in a new proposed indirect adaptive control to be described in section 0.

4. Proposed Reduction: 3-Parameter Regression ("Proposed3")

Typical assumptions for simplified spacecraft dynamics modeling include neglecting inertia cross-products. The result is the following regression model.

$$u_{ff} = \begin{bmatrix} \dot{\omega}_{x_r} & -\omega_y \omega_{z_r} & \omega_z \omega_{y_r} \\ \omega_x \omega_{z_r} & \dot{\omega}_{y_r} & -\omega_z \omega_{x_r} \\ -\omega_x \omega_{y_r} & \omega_y \omega_{x_r} & \dot{\omega}_{z_r} \end{bmatrix} \begin{Bmatrix} J_{xx} \\ J_{yy} \\ J_{zz} \end{Bmatrix}$$

(39)

Figure 32 CONTRIBUTION 7: Reduction of Fossen's approach to 3-parameters.

The second proposed improvement to Slotine/Fossen's adaptive technique (*Proposed3*) utilizes this regression model.

5. Proposed Adaptive Control Algorithm

While the developments so far simplify the promising Slotine/Fossen approach, it is noted that λ defines the reference trajectory which is fed to both feedback and feedforward controls. Recall that *ideal* feedforward control perfectly achieves commanded maneuvers if the modeled inertia is *exactly* equal to the actual inertia. Feedback control is useful to catch the errors *after they have already been incurred*. The Slotine/Fossen approach does not feedback the desired, commanded trajectory. The feedback signal is calculated based on error tracking the more aggressive (leading/lagging) reference trajectory. It is intuitive to make a more aggressive *feedforward* signal if your inertia estimate is low, and a less aggressive *feedforward*

50

signal if your inertia estimate is high. But *feedback* controls are attempting to fix the attitude at the next time step with error based on the previous time step without using knowledge of upcoming trajectory which could be in an arbitrary direction. It is proposed that using the correct, desired trajectory to define the error in the feedback control while maintaining the reference trajectory for adaptive feedforward should result in lower tracking error.
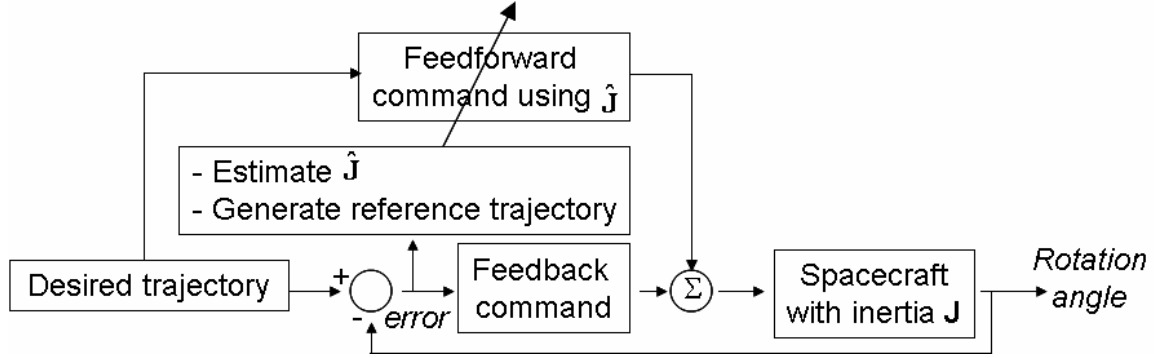

Figure 33 CONTRIBUTION 8: Proposed adaptive spacecraft command relationships.

This is accomplished by introducing a λ_{ff} to be used in the feedforward signal identically as λ previously derived in the Slotine/Fossen method. For feedback, λ_{fb} will be fixed to equate to normal PD (desired trajectory) feedback control per:

$$u_{fb} = -K_d(\dot{q} - \dot{q}_d) - \underbrace{\lambda_{fb} K_d}_{K_p}(q - q_d).$$
(40)

For example, the feedback control signal using Slotine/Fossen with $\lambda=1/2$ would equate to the proposed method feeding back the desired trajectory with a normal PD control using $K_p=100$, $K_d=200$ (*units* dropped for convenience). The feedback control relationships would be identical using either method. With this in mind it will become clear that increasing λ_{ff} will result in relative improvement.

$$\tau = \underbrace{[\Phi_r]\{\hat{\Theta}\}}_{u_{ff}} \underbrace{- K_d(\dot{q} - \dot{q}_d) - \underbrace{\lambda_{fb} K_d}_{K_p}(q - q_d)}_{u_{fb}}$$
(41)

51

a. *Stability Analysis*

Consider not using the reference trajectory in the feedback signal. The previous stability proof (Refs.[43],[46]) are no longer valid. The control equation would be $\tau = \Phi_r \hat{\Theta} - \mathbf{K}_d \dot{\tilde{\mathbf{q}}} - \mathbf{K}_p \tilde{\mathbf{q}}$ (where r denotes "reference," ~ denotes error from desired and $\hat{\Theta}$ denotes estimates) and the estimation equation is maintained $\dot{\hat{\Theta}}^T = -\mathbf{s}^T \Phi_r \Gamma$ where Γ is a positive constant estimation rate gain. And "$\mathbf{s}$" is a measure of error to be defined. Notice that this estimation dynamics equation implies any error (including noise and disturbances) will result in estimate dynamics (not just parameter error).

$$\tau = \Phi_r \hat{\Theta} - \mathbf{K}_d \dot{\tilde{\mathbf{q}}} - \mathbf{K}_p \tilde{\mathbf{q}}$$

$$\dot{\hat{\Theta}}^T = -\mathbf{s}^T \Phi_r \Gamma$$

Figure 34 CONTRIBUTION 8 Proposed Adaptive Control algorithm (42).

After defining requisite quantities, Lyapunov analysis demonstrates stability and convergence. First define the ideal feedforward control from the dynamics. If the dynamics were exactly known, they would determine the feedforward control that would accomplish a desired maneuver $\{\ddot{\mathbf{q}}_d\}$ with no error.

$[\mathbf{J}]\{\ddot{\mathbf{q}}\} + [\mathbf{C}]\{\dot{\mathbf{q}}\} = \{\tau\}$ for $\mathbf{J} = \mathbf{J}^T > 0$, $\dot{\mathbf{J}} = 0$, $\mathbf{C}$=skew symmetric

Define: $[\mathbf{J}]\{\ddot{\mathbf{q}}\} + [\mathbf{C}]\{\dot{\mathbf{q}}\} = \{\tau\}_{ideal} = [\mathbf{J}]\{\ddot{\mathbf{q}}_d\} + [\mathbf{C}]\{\dot{\mathbf{q}}_d\} = \{\Phi\}[\Theta] = \{\mathbf{u}_{ff}\}_{ideal}$ (43)

Define the tracking errors: $\tilde{\mathbf{q}} = \mathbf{q} - \mathbf{q}_d$ Thus $\dot{\tilde{\mathbf{q}}} = \dot{\mathbf{q}} - \dot{\mathbf{q}}_d$ and $\ddot{\tilde{\mathbf{q}}} = \ddot{\mathbf{q}} - \ddot{\mathbf{q}}_d$ (44)

Allowing definition of the reference trajectory $\ddot{\mathbf{q}}_r = \ddot{\mathbf{q}}_d - \lambda(\underbrace{\dot{\mathbf{q}} - \dot{\mathbf{q}}_d}_{\tilde{\mathbf{q}}}) = \ddot{\mathbf{q}}_d - \lambda(\dot{\tilde{\mathbf{q}}})$ (45)

and $\dot{\mathbf{q}}_r = \dot{\mathbf{q}}_d - \lambda(\underbrace{\mathbf{q} - \mathbf{q}_d}_{\tilde{\mathbf{q}}}) = \dot{\mathbf{q}}_d - \lambda(\tilde{\mathbf{q}})$ (46)

Define a combined measure of tracking error (error tracking the reference trajectory):

$$\mathbf{s} = \dot{\mathbf{q}} - \dot{\mathbf{q}}_r = \dot{\tilde{\mathbf{q}}} + \lambda\tilde{\mathbf{q}} = (\dot{\mathbf{q}} - \dot{\mathbf{q}}_d) + \lambda(\mathbf{q} - \mathbf{q}_d)$$ (47)

52

$$\dot{\mathbf{s}} = \ddot{\mathbf{q}} - \ddot{\mathbf{q}}_r = \ddot{\tilde{\mathbf{q}}} + \lambda\dot{\tilde{\mathbf{q}}} = (\ddot{\mathbf{q}} - \ddot{\mathbf{q}}_d) + \lambda(\dot{\mathbf{q}} - \dot{\mathbf{q}}_d) \tag{48}$$

From our earlier regression definition of the feedforward control,

Define: $\quad \Theta = \left\{ J_{xx} \quad J_{xy} \quad J_{xz} \quad J_{yy} \quad J_{yz} \quad J_{zz} \right\}^T \ \& \ \dot{\Theta} = 0 \tag{49}$

$$\hat{\Theta} = \left\{ \hat{J}_{xx} \quad \hat{J}_{xy} \quad \hat{J}_{xz} \quad \hat{J}_{yy} \quad \hat{J}_{yz} \quad \hat{J}_{zz} \right\}^T \tag{50}$$

Thus, the estimated dynamics may be defined using a similar regression:

$$\left[\hat{\mathbf{J}}\right]\{\ddot{\mathbf{q}}_r\} + \left[\hat{\mathbf{C}}\right]\{\dot{\mathbf{q}}_r\} = \left[\Phi_r(\mathbf{q},\dot{\mathbf{q}},\dot{\mathbf{q}}_r,\ddot{\mathbf{q}}_r)\right]\{\hat{\Theta}\} \tag{51}$$

Define the estimation error as the difference between estimated and actual inertia:

$$\tilde{\Theta} = \hat{\Theta} - \Theta \tag{52}$$

Consider the candidate Lyapunov function:

$$V = \frac{1}{2}\mathbf{s}^T\mathbf{J}\mathbf{s} + \frac{1}{2}\tilde{\Theta}^T\Gamma^{-1}\tilde{\Theta} + \frac{1}{2}\tilde{\mathbf{q}}^T\left(\lambda\mathbf{K}_d + \mathbf{K}_p\right)\tilde{\mathbf{q}} \tag{53}$$

Differentiating:

$$\dot{V} = \mathbf{s}^T\mathbf{J}\dot{\mathbf{s}} + \dot{\tilde{\Theta}}^T\Gamma^{-1}\tilde{\Theta} + \dot{\tilde{\mathbf{q}}}^T\left(\lambda\mathbf{K}_d + \mathbf{K}_p\right)\tilde{\mathbf{q}} \tag{54}$$

Substitute for $\dot{\mathbf{s}}$, distribute [**J**], substitute for $\mathbf{J}\ddot{\mathbf{q}}$ and add & subtract $\mathbf{C}\dot{\mathbf{q}}_r$ grouping $\Phi_r\Theta$.
Then reverse distribute [**C**] and substitute for **s** for $\dot{\mathbf{q}} - \dot{\mathbf{q}}_r$. Use skew symmetry to reduce:

$$\dot{V} = \mathbf{s}^T\left(\tau - \mathbf{J}\ddot{\mathbf{q}}_r - \mathbf{C}\dot{\mathbf{q}}_r\right) + \dot{\tilde{\Theta}}^T\Gamma^{-1}\tilde{\Theta} + \dot{\tilde{\mathbf{q}}}^T\left(\lambda\mathbf{K}_d + \mathbf{K}_p\right)\tilde{\mathbf{q}} \tag{55}$$

From Figure 34 $\tau = \Phi_r\hat{\Theta} - \mathbf{K}_d\dot{\tilde{\mathbf{q}}} - \mathbf{K}_p\tilde{\mathbf{q}} \tag{56}$

Group $\Phi_r\tilde{\Theta}$ and equate $\dot{\tilde{\Theta}} = \dot{\hat{\Theta}}$ using $\dot{\Theta} = 0$.

$$\dot{V} = \mathbf{s}^T\left(\Phi_r\tilde{\Theta} - \mathbf{K}_d\dot{\tilde{\mathbf{q}}} - \mathbf{K}_p\tilde{\mathbf{q}}\right) + \dot{\tilde{\Theta}}^T\Gamma^{-1}\tilde{\Theta} + \dot{\tilde{\mathbf{q}}}^T\left(\lambda\mathbf{K}_d + \mathbf{K}_p\right)\tilde{\mathbf{q}} \tag{57}$$

Using the combined measure of tracking error define $\dot{\hat{\Theta}}^T = -\mathbf{s}^T\Phi_r\Gamma \qquad \Gamma>0 \tag{58}$

Cancel $\Phi_r\tilde{\Theta}$ and substitute for $\mathbf{s}^T$ and distribute $(\dot{\tilde{\mathbf{q}}} + \lambda\tilde{\mathbf{q}})^T$ twice. Group terms then reverse distribute to $\left(\lambda\mathbf{K}_d + \mathbf{K}_p\right)$ canceling $\left(\lambda\mathbf{K}_d + \mathbf{K}_p\right)$ terms.

$$\boxed{\dot{V} = -\dot{\tilde{\mathbf{q}}}^T\mathbf{K}_d\dot{\tilde{\mathbf{q}}} - \lambda\tilde{\mathbf{q}}^T\mathbf{K}_p\tilde{\mathbf{q}} \leq 0} \tag{59}$$

For negative semi-definite Lyapunov function derivative, Barbalat's lemma says: if the differential function $V(t)$ has a finite limit as $t\to\infty$ (bounded) and is such that $\ddot{V}(t)$ exists and is bounded, then $\dot{V}(t)\to 0$ as $t\to\infty$. V(t) is lower bounded and $\dot{V}(t)$ is negative semi-definite, so if $\dot{V}(t)$ is uniformly continuous in time, then $\dot{V}(t)\to 0$ as $t\to\infty$. $\ddot{V} = -2\ddot{\tilde{\mathbf{q}}}^T\mathbf{K}_d\dot{\tilde{\mathbf{q}}} - \lambda\dot{\tilde{\mathbf{q}}}^T\mathbf{K}_p\tilde{\mathbf{q}}$ and $\ddot{\tilde{\mathbf{q}}} = \ddot{\mathbf{q}} - \ddot{\mathbf{q}}_d$. Since $V(t) < V(0)\forall t$, $V(t) = V(\mathbf{s},\dot{\tilde{\mathbf{q}}},\tilde{\mathbf{q}},\tilde{\Theta})$ is bounded, thus $\mathbf{s},\dot{\tilde{\mathbf{q}}},\tilde{\mathbf{q}},$ and $\tilde{\Theta}$ are all bounded. Since $\tilde{\mathbf{q}} = \mathbf{q} - \mathbf{q}_d$ and $\dot{\tilde{\mathbf{q}}} = \dot{\mathbf{q}} - \dot{\mathbf{q}}_d$ are bounded, and $\dot{\mathbf{q}}_d$ & $\mathbf{q}_d$ are bounded inputs, $\mathbf{q}$ and $\dot{\mathbf{q}}$ are bounded, thus, $\dot{\mathbf{q}}_r$ is bounded. Also, since $\ddot{\mathbf{q}}_d$ is a bounded input, $\ddot{\mathbf{q}}_r$ is bounded. Additionally, Since $\tilde{\Theta} = \hat{\Theta} - \Theta$ is bounded, and Θ is a bounded real world system (no such system of infinite inertia), $\hat{\Theta}$ is bounded, thus $\boldsymbol{\tau}(\hat{\Theta},\mathbf{q}_r,\dot{\mathbf{q}}_r)$ is bounded. Recalling the Newton-Euler relation and our defined torque (noting we have just demonstrated $\boldsymbol{\tau}(\hat{\Theta},\mathbf{q}_r,\dot{\mathbf{q}}_r)$ and $\dot{\mathbf{q}}$ are bounded), $\ddot{\mathbf{q}}$ must be bounded.

$$[\mathbf{J}]\{\ddot{\mathbf{q}}\} + [\mathbf{C}]\{\dot{\mathbf{q}}\} = \boldsymbol{\tau}(\hat{\Theta},\mathbf{q}_r,\dot{\mathbf{q}}_r) \to \{\ddot{\mathbf{q}}\} = [\mathbf{J}]^{-1}\left[\boldsymbol{\tau}(\hat{\Theta},\mathbf{q}_r,\dot{\mathbf{q}}_r) - [\mathbf{C}]\{\dot{\mathbf{q}}\}\right] \tag{60}$$

Since $\ddot{V}$ is bounded, $\dot{V}$ is uniformly continuous. According to Barbalat's lemma $\dot{V} = -\dot{\tilde{\mathbf{q}}}^T\mathbf{K}_d\dot{\tilde{\mathbf{q}}} - \lambda\tilde{\mathbf{q}}^T\mathbf{K}_p\tilde{\mathbf{q}} \to 0$ as $t\to\infty$. $\boxed{\dot{\tilde{\mathbf{q}}},\tilde{\mathbf{q}} \to 0 \text{ } as \text{ } t\to\infty}$ (61)

Estimate convergence requires persistent excitation in maneuvering. Also note that this stability proof requires estimation. Another technique without estimation will be addressed later, and stability of this new approach cannot be demonstrated with this argument. Adaptive controllers have become notorious since the 1960's and 1970s for instability often due to estimation parameter drift. In 1966 Michael James Adams was killed when his X-15 aircraft was torn apart due to his adaptive control system[47],[48]. The X-15 entered a divergent spiral as the adaptive controller estimates

diverged[49]. Accordingly, great efforts are exerted in this research to simplify the estimation and eventually eliminate estimation altogether.
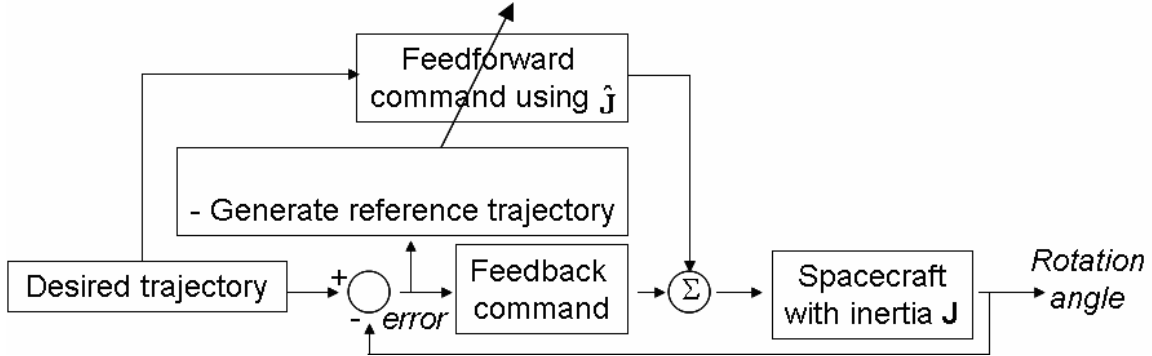

Figure 35 CONTRIBUTION 9: Proposed adaptive feedforward with no estimation.

$$\tau = \Phi_r \hat{\Theta} - \mathbf{K}_d \dot{\tilde{\mathbf{q}}} - \mathbf{K}_p \tilde{\mathbf{q}} \text{ where } \dot{\hat{\Theta}} = 0$$

Figure 36 CONTRIBUTION 9 Proposed Adaptive Control algorithm (62).

6. Adaptive Control Simulations

In this section, a nominal target tracking maneuver is performed with various control techniques to compare performance. The maneuver consists of a steady yaw (earth-tracking maneuver) with sinusoidal roll (target evasion). Older estimated values of the experimental testbed's inertia (prior to installation of the optical payload) are used as the simulated *actual*. It is assumed that a guess of inertia is available to design the feedforward torque command. The feedforward command assumed a diagonal inertia matrix whose components were 10% less than actual values for simulations.

$$\begin{bmatrix} J \end{bmatrix}_{actual(old\ data)} = \begin{bmatrix} 119.1259 & -15.7678 & -6.5486 \\ -15.7678 & 150.6615 & 22.3164 \\ -6.5486 & 22.3164 & 106.0288 \end{bmatrix} \qquad (63)$$

The controllers were individually coded in MATLAB/SIMULINK with switches used to activate controls. Each control was permitted to formulate commands for identical desired maneuvers fed into an identical spacecraft simulation model allowing "apples-to-apples" comparison.
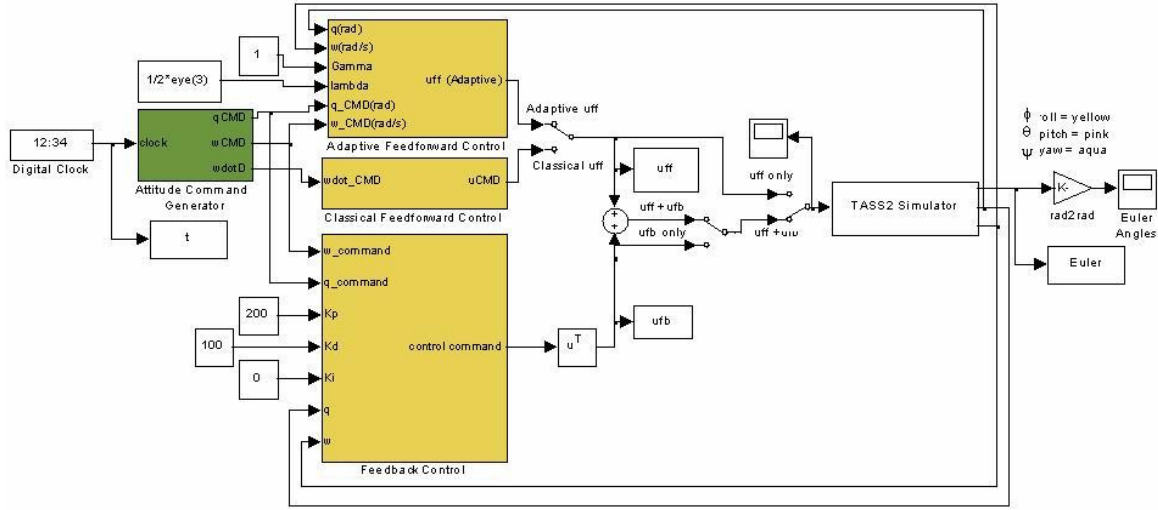
Figure 37 SIMULINK program used to compare advanced control algorithms.

After 10 seconds of initial regulation, the inertial target acquisitions acceleration trajectory is as follows.

$$
10 < t < 18 : \left\{ \ddot{\boldsymbol{x}}_d \right\} = \left\{ \begin{array}{c} 0 \\ 0 \\ -8 \left(\dfrac{\pi}{16} \right)^2 \sin \left(\dfrac{\pi}{16} (t - 10) \right) \end{array} \right\} \tag{64}
$$

$$
18 < t < 20 : \left\{ \ddot{\boldsymbol{x}}_d \right\} = \left\{ \begin{array}{c} 0 \\ 0 \\ -15 \left(\dfrac{\pi}{16} \right)^2 \sin \left(\dfrac{\pi}{16} (t - 10) \right) \end{array} \right\} \tag{65}
$$

Immediately following the acquisition maneuver, the inertial target tracking acceleration maneuver is as follows:

$$t > 20 : \quad \left\{ \ddot{x}_d \right\} = \begin{Bmatrix} -\left(\dfrac{2\pi}{30}\right)^2 \cos\left(\dfrac{2\pi}{30}t\right) \\[2em] 0 \\[2em] -\left(\dfrac{1}{10}\right)^2 \left(\dfrac{2\pi}{10}e^{-t} - te^{-t}\right) \end{Bmatrix} \qquad (66)$$

Recall a representative military space mission requiring rapid target acquisitions, and tracking with fine pointing may be tracking a non-cooperative target. The maneuver trajectory simulates a rapid slew yaw maneuver followed by aggressive target run in the yaw axis with target evasion simulated in roll axis.

Control Nomenclature	Methodology
[Slotine/Fossen]	Adaptive control introduced by Slotine and modified by Fossen. Use estimated inertia in feedforward signal and use reference trajectory to adapt both feedforward and feedback signals.
Derived6	Derived 6-parameter estimation form of [Slotine/Fossen] shown to be identical to 9-parameter [Slotine/Fossen] as presented in the literature.
Proposed6 ($\Gamma=i$) "i" indicates several Γs will be investigated.	Suggested adaptive feedforward using 6-parameter inertia estimation and more aggressive reference trajectory with standard PD feedback control. Γ is the estimation/adaption gain. $\Gamma =0$ indicates no estimation (a separate technique).
Proposed3 ($\Gamma=i$) "i" indicates several Γs will be investigated.	Suggested adaptive feedforward using 3-parameter inertia estimation and more aggressive reference trajectory with standard PD feedback control. Γ is the estimation/adaption gain. $\Gamma =0$ indicates no estimation (a separate technique).

Table 2 Nomenclature of adaptive control techniques.
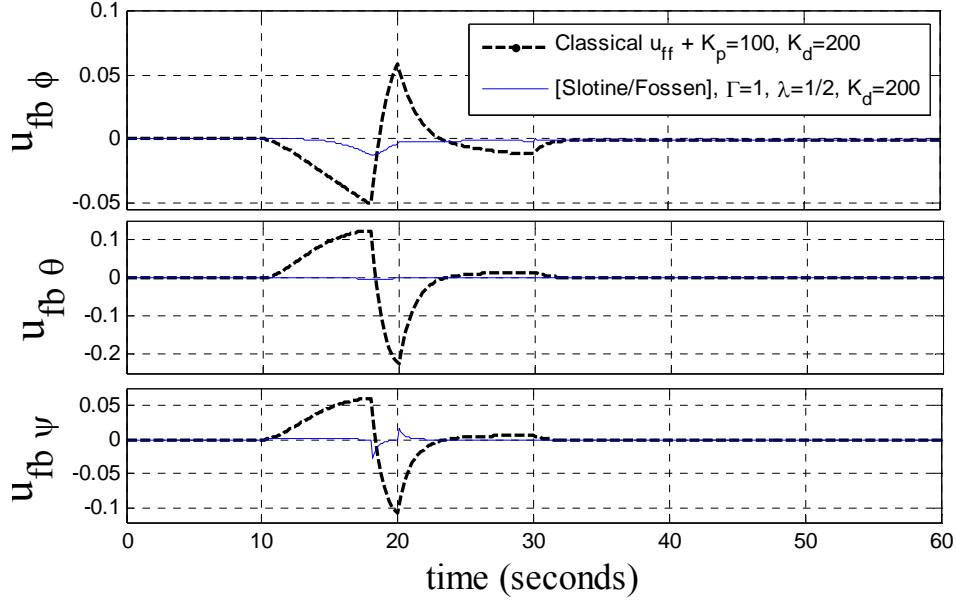
Figure 38 SIMULATION: Classical Vs. Slotine comparison 10% Inertia Error.

$\Gamma=1$, $\lambda_{fb}=1/2$, $\lambda_{ff}=1$,Kp=100,Kd=200. 10% Inertia Error for large-angle acquisition maneuver followed by target tracking trajectory: Feedback control comparison Classical feedforward + PD feedback versus [Slotine/Fossen] as proposed in the literature. Feedforward control assumed 10% less inertia than actual and assumes diagonal inertia matrix.
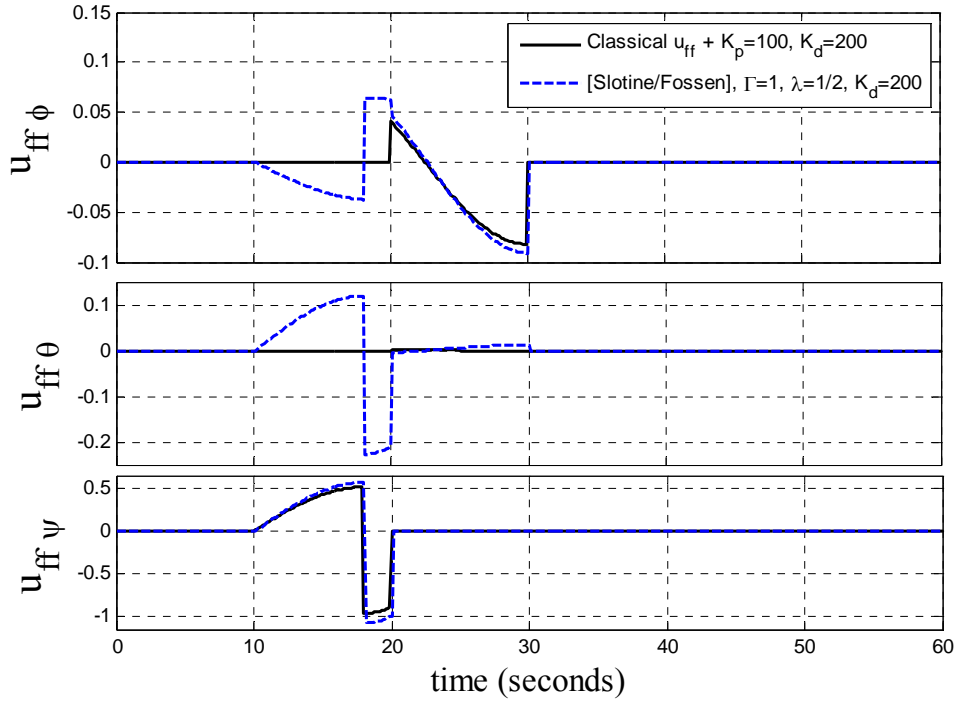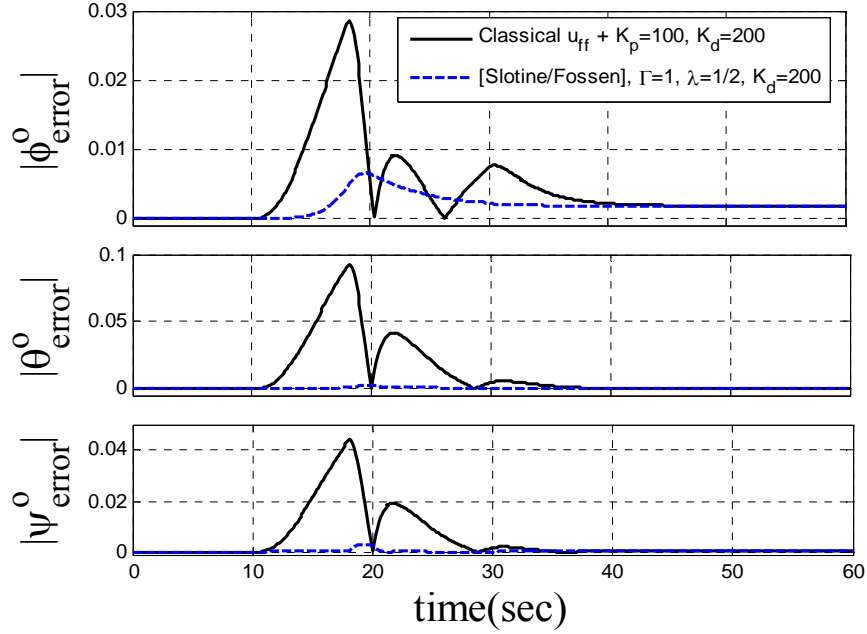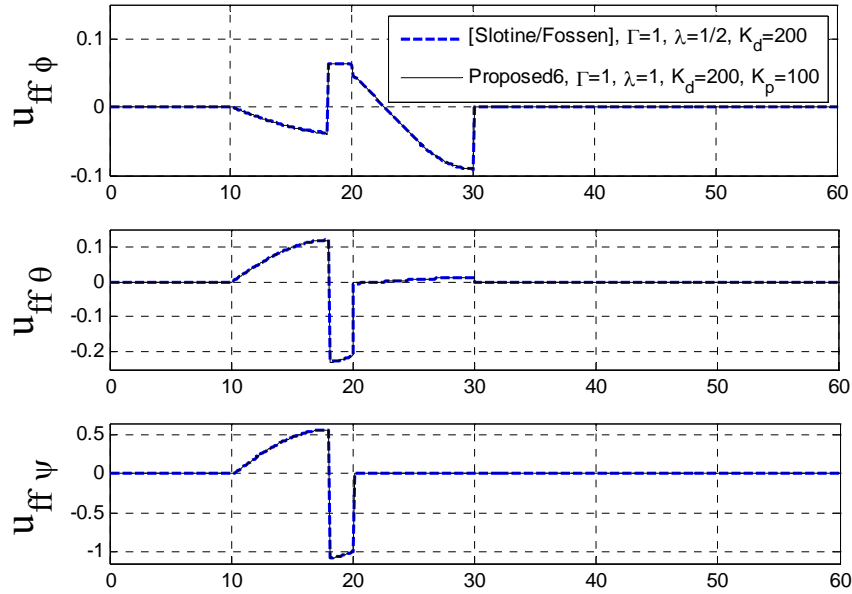

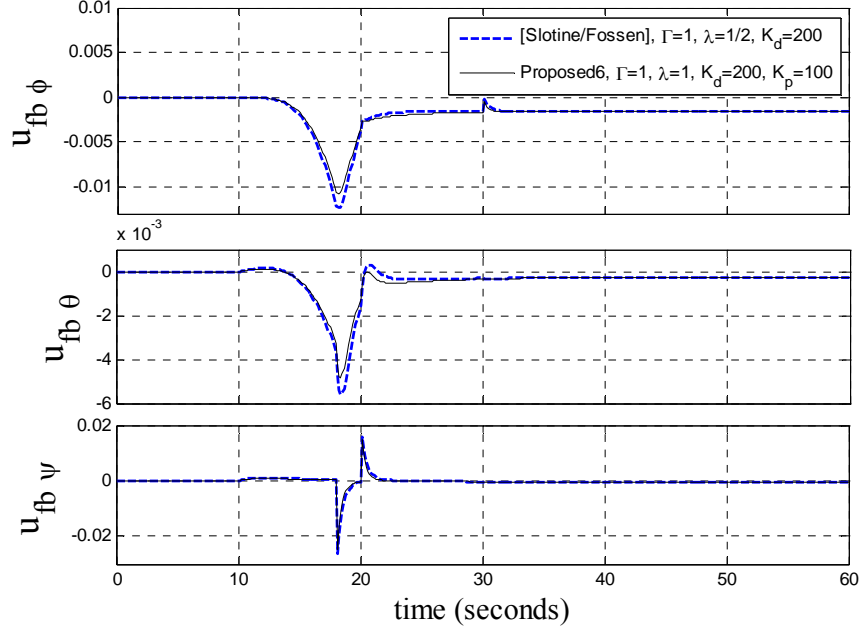Figure 39 SIMULATION: Classical Vs. Slotine comparison 10% Inertia Error.

$\Gamma=1$, $\lambda_{fb}=1/2$, $\lambda_{ff}=1$,Kp=100,Kd=200. 10% Inertia Error for large-angle acquisition maneuver followed by target tracking trajectory: Feedforward control comparison Classical feedforward + PD feedback versus [Slotine/Fossen] as proposed in the literature. Feedforward control assumed 10% less inertia than actual and assumes diagonal inertia matrix.

58

Figure 40 SIMULATION: Classical Vs. Slotine comparison 10% Inertia Error.

Γ=1, λ_{fb}=1/2, λ_{ff}=1,Kp=100,Kd=200. 10% Inertia Error for large-angle acquisition maneuver followed by target tracking trajectory: Tracking errors (roll ϕ, pitch θ, yaw ψ in degrees) comparison Classical feedforward + PD feedback control versus [Slotine/Fossen] as proposed in the literature. Feedforward control assumed 10% less inertia than actual and assumes diagonal inertia matrix.

Figure 41 SIMULATION: Adaptive control comparison 10% Inertia Error.

Γ=1, λ_{fb}=1/2, λ_{ff}=1,Kp=100,Kd=200. 10% Inertia Error for large-angle acquisition maneuver followed by target tracking trajectory: Feedforward control comparison [Slotine/Fossen] as proposed in the literature versus *Proposed6*. Feedforward control assumed 10% less inertia than actual and assumes diagonal inertia matrix.
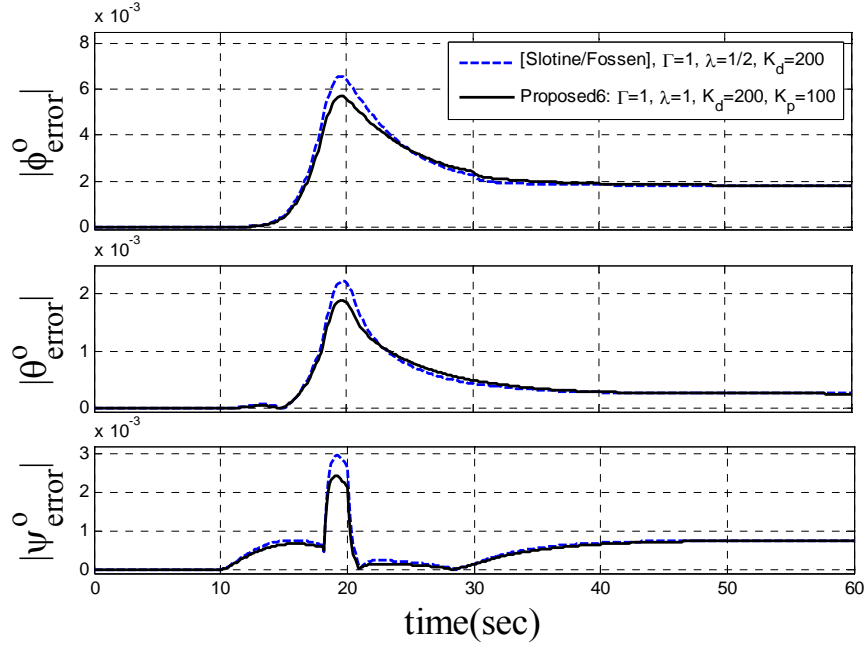
Figure 42 SIMULATION: Adaptive control comparison 10% Inertia Error.

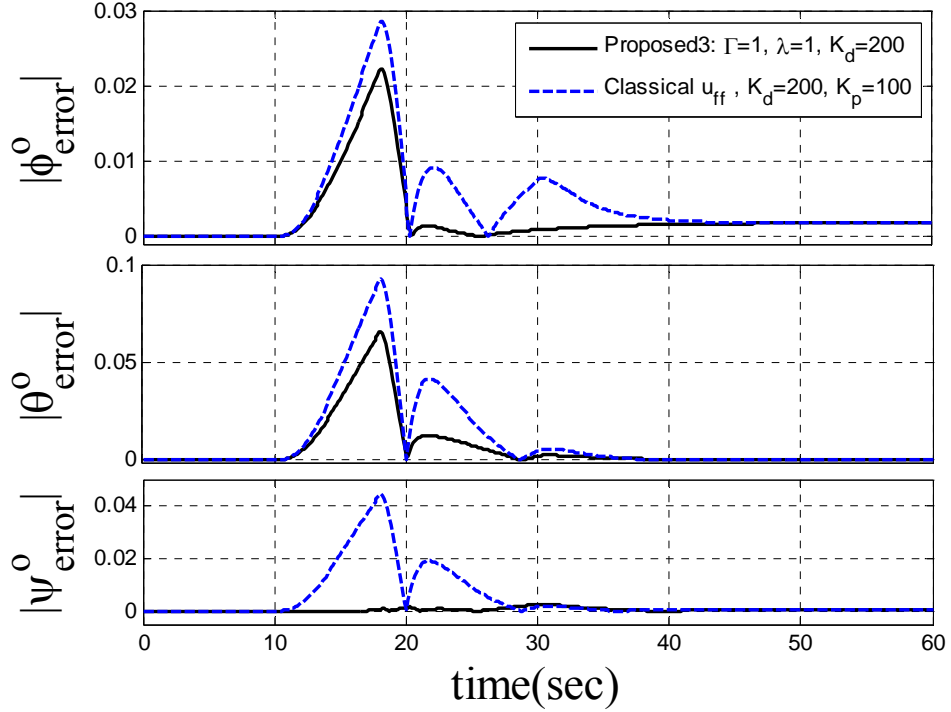$\Gamma=1$, $\lambda_{fb}=1/2$, $\lambda_{ff}=1$, Kp=100, Kd=200. 10% Inertia Error for large-angle acquisition maneuver followed by target tracking trajectory: Feedback control comparison [Slotine/Fossen] as proposed in the literature versus *Proposed6*. Feedforward control assumed 10% less inertia than actual and assumes diagonal inertia matrix.

Figure 43 SIMULATION: Adaptive control comparison 10% Inertia Error.

$\Gamma=1$, $\lambda_{fb}=1/2$, $\lambda_{ff}=1$, Kp=100, Kd=200 10% Inertia Error for large-angle acquisition maneuver followed by target tracking trajectory: Tracking errors (roll ϕ, pitch θ, yaw ψ in degrees) comparison [Slotine/Fossen] as proposed in the literature versus *Proposed6*. Feedforward control assumed 10% less inertia than actual and assumes diagonal inertia matrix.

60
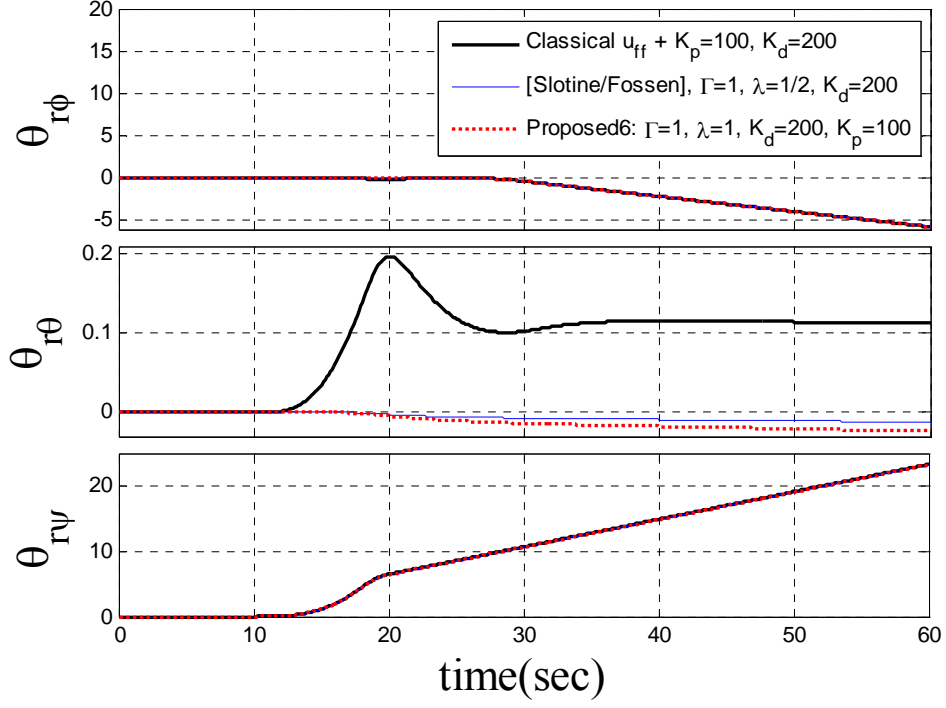
Figure 44 SIMULATION: Reference Trajectory comparison 10% Inertia Error.

$\Gamma=1$, $\lambda_{fb}=1/2$, $\lambda_{ff}=1$, Kp=100, Kd=200

Figure 45 SIMULATION: Proposed3 Vs. Classical feedforward + PD feedback.

$\Gamma=1$, $\lambda_{fb}=1/2$, $\lambda_{ff}=1$, Kp=100, Kd=200 10% inertia error.

60 second ATP Simulation, [J]error=10%	RMS ϕ^o Error	RMS θ^o Error	RMS ψ^o Error
K_p=100; K_d=200 only	1.16433297E-02	1.13170883E-02	4.69008123E-02
Classical u_{ff} + K_p=K_d=200* **BASELINE**	4.18550804E-03	1.03111235E-02	4.97428943E-03
[Slotine/Fossen] λ=1/2, Γ=1,K_d=200	3.54779190E-03	4.00139441E-04	4.49608508E-04
[Slotine/Fossen] λ=1/2, Γ=0,K_d=200	3.54779201E-03	4.00139485E-04	4.49608482E-04
Derived6: λ=1/2, Γ=1,K_d=200	3.54779190E-03	4.00139441E-04	4.49608508E-04
Proposed6: λ_{ff}=1, Γ=1,K_d=200, λ_{fb}=1/2	3.43409393E-03	4.31624240E-04	4.11224769E-04
Proposed6: λ_{ff}=1, Γ=0,K_d=200, λ_{fb}=1/2	3.43409412E-03	4.31624299E-04	4.11224783E-04
Proposed3: λ_{ff}=1, Γ=1,K_d=200, λ_{fb}=1/2	4.22287958E-03	6.00879340E-03	4.83002003E-04
Proposed3: λ_{ff}=1, Γ=0,K_d=200, λ_{fb}=1/2	4.22287958E-03	6.00879341E-03	4.83001979E-04

Table 3 Control Simulation Summary (10% Error).

With 10% Inertia Error for large-angle acquisition maneuver followed by target tracking trajectory: Tracking errors (roll ϕ, pitch θ, yaw ψ in degrees) comparison. Feedforward control assumed 10% less inertia than actual and assumes diagonal inertia matrix. Perfect sensor data is assumed, so experiments should certainly exhibit higher mean square errors.
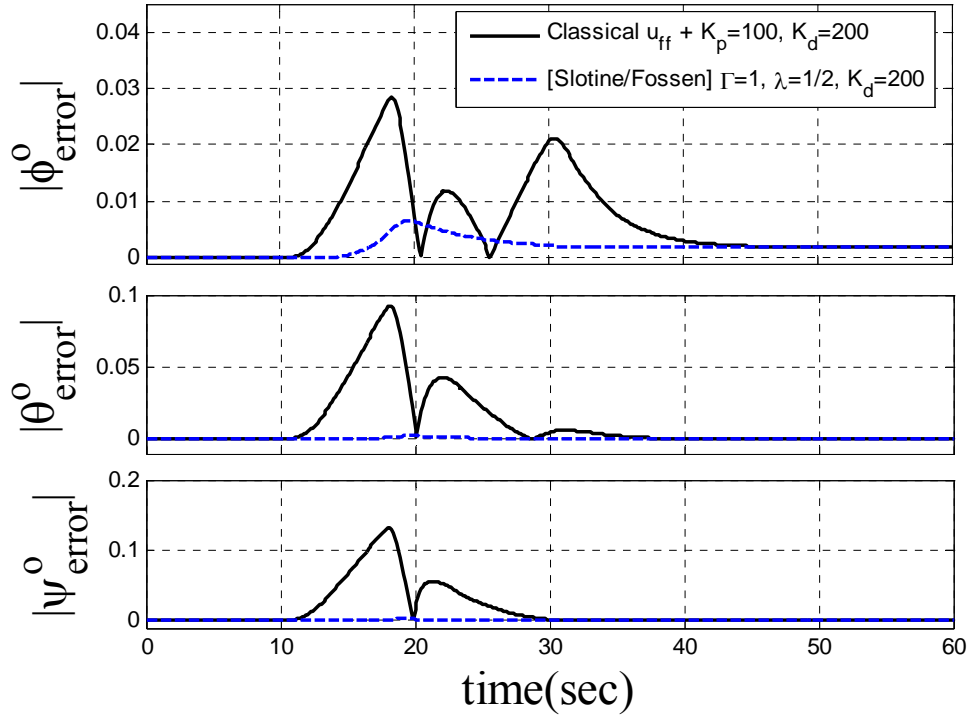

Figure 46 SIMULATION: Classical control comparison 30% Inertia Error.

30% Inertia Error for large-angle acquisition maneuver followed by target tracking trajectory: Tracking errors (roll ϕ, pitch θ, yaw ψ in degrees) comparison: Classical feedforward + PD feedback control versus [Slotine/Fossen] as proposed in the literature. Feedforward control assumed 30% less inertia than actual and assumes diagonal inertia matrix.
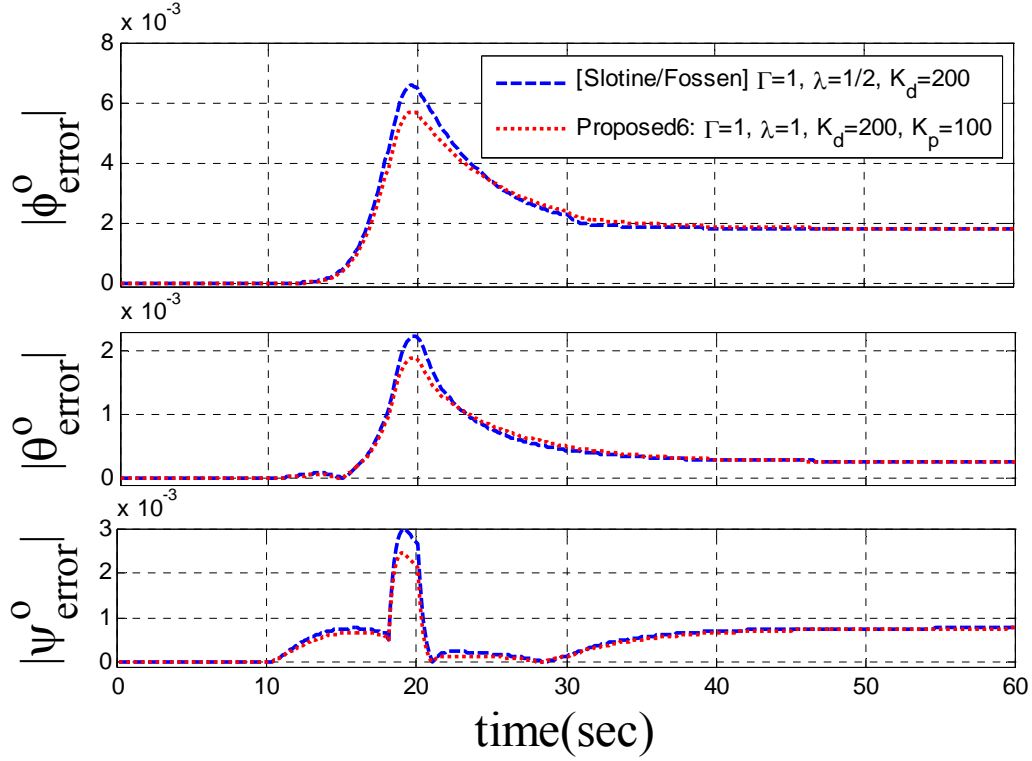
Figure 47 SIMULATION: Adaptive control comparison 30% Inertia Error.

Large-angle acquisition maneuver followed by target tracking trajectory: Tracking errors (roll ϕ, pitch θ, yaw ψ in degrees) comparison: [Slotine/Fossen] as presented in the literature versus *Proposed6* adaptive feedforward & PD feedback control. Feedforward control assumed 30% less inertia than actual and assumes diagonal inertia matrix.

60 second ATP Simulation, [J]error=30%	RMS ϕ^o Error	RMS θ^o Error	RMS ψ^o Error
K_p=100; K_d=200 only	1.164333E-02	1.131709E-02	4.690081E-02
Classical u_{ff} + K_p=K_d=200* **BASELINE**	5.819660E-03	1.049933E-02	1.407292E-02
[Slotine/Fossen] λ=1/2, Γ=1,K_d=200	3.547792E-03	4.001394E-04	4.496085E-04
[Slotine/Fossen] λ=1/2, Γ=0,K_d=200	3.547792E-03	4.001395E-04	4.496085E-04
Derived6: λ=1/2, Γ=1,K_d=200	3.547792E-03	4.001394E-04	4.496085E-04
Proposed6: λ_{ff}=1, Γ=1,K_d=200, λ_{fb}=1/2	3.434094E-03	4.316242E-04	4.112248E-04
Proposed6: λ_{ff}=1, Γ=0,K_d=200, λ_{fb}=1/2	3.434094E-03	4.316243E-04	4.112248E-04
Proposed3: λ_{ff}=1, Γ=1,K_d=200, λ_{fb}=1/2	4.222880E-03	6.008793E-03	4.830020E-04
Proposed3: λ_{ff}=1, Γ=0,K_d=200, λ_{fb}=1/2	4.222880E-03	6.008793E-03	4.830020E-04

Table 4 Control simulation summary(30% Error).

With 30% Inertia Error for large-angle acquisition maneuver followed by target tracking trajectory: Tracking errors (roll ϕ, pitch θ, yaw ψ in degrees) comparison. Feedforward control assumed 10% less inertia than actual and assumes diagonal inertia matrix. Perfect sensor data is assumed, so experiments should certainly exhibit higher mean square errors.

7.   Summary

General qualitative conclusions may be drawn from the ideal (no noise) simulations. PD Feedback alone can accomplish the maneuver, but combined classical feedforward plus PD feedback control is much better. Slotine/Fossen's adaptive techniques can improve performance more while also providing updated inertia estimates (not strictly required for reduced tracking errors). Furthermore, a simplified 6-parameter estimation algorithm retains the performance of Slotine/Fossen's method with further slight improvements where the feedforward control is made more aggressive, retaining PD feedback control. The proposed adaptive controller uses the reference trajectory *only* for feedforward controls allowing this performance increase. In the case used here (significant off-diagonal inertia terms), a proposed 3-parameter identification also improves performance compared to classical feedforward + PD feedback control, but does not perform as well as the higher computational algorithms.

Slotine's *Hamiltonian Adaptive Control of Spacecraft* [43] introduced a promising general methodology for nonlinear adaptive control of spacecraft with inertia estimation. The technique was handicapped by its derivation in the inertial reference frame.   Fossen's *Comments on Hamiltonian Adaptive Control of Spacecraft* [46] suggested equivalent formulation in the body reference frame, considerably reducing algorithmic complexity.   Fossen's formulation is derived and demonstrated here to improve performance compared to feedback, and classical feedforward with feedback controls. Furthermore an improvement is presented that utilizes the desired trajectory in the feedback control while maintaining the reference trajectory in the feedforward control. This improves performance further compared to all control methods. Two alternative formulations are presented to further simplify the computational complexity. A mere-three parameter adaptive control is even capable of controlling a spacecraft with non-negligible products of inertia based on these results.   A further algorithmic simplification is available by eliminating inertia estimation in cases where the estimates are not desired. Noting Table 3 & Table 4, Γ=0 was used to eliminate estimate dynamics evaluating the effectiveness of reference trajectory without estimation (a fixed gain robust controller). While the tracking performance is *technically* degraded (on the order

of 10^{-9} degrees), essentially no performance is lost by only using the reference trajectory fixed gain robust controller eliminating the estimation dynamics.

1. Slotine/Fossen improves ATP performance compared to current methods.

2. A derived "inertia-only" estimation method (*Derived6*) is identically effective.

3. *Proposed6* (maintaining PD feedback control and increasing 6-parameter adaptive feedforward control) further improves upon Slotine/Fossen's results.

4. *Proposed3* (maintaining PD feedback control and increasing 3-parameter adaptive feedforward control) effectively controls (with reduced performance compared to other adaptive methods only), as a simplified alternative.

5. Estimation is not required to improve tracking performance

THIS PAGE INTENTIONALLY LEFT BLANK

III. EXPERIMENTAL SPACECRAFT SIMULATOR

A. INTRODUCTION

A major contribution provided in this research dissertation is comprehensive simulation *and* experimental verification. While many modern algorithms seem promising on paper, real world situations often confound some modern algorithms. With this motivation, every proposed contribution presented here has been experimentally verified on a free-floating, three-axis spacecraft simulator. Such large, expensive realistic hardware is rare, so it is natural to fully explain the experimental setup in detail. The free-floating spacecraft testbed is referred to as TASS2 indicating it's heritage as the second such testbed developed at the Naval Postgraduate School.

The first testbed, TASS1 (ref [50]) was much smaller and did not utilize control moment gyroscopes. The spacecraft testbed's payload is an optical relay for laser beams. The lower deck of the spacecraft is a bench model spacecraft with control moment gyroscopes, active mass balancing system, fiber optic gyroscopes for attitude rate sensing, and typical onboard computers. The upper deck of the testbed is an experimental laser optical relay designed to accept a laser from the ground, aircraft or space-based source and relay the laser to an uncooperative target on the ground, in the air or in space. Description of the mission and some details about experimental hardware may be found in ref [53].

This laser relay mission demands rapid target acquisitions maneuvers in minimum time followed by fine pointing during target tracking. Accordingly, it provides an ideal venue for demonstration of the ATP improvements recommended in this thesis. Significant research effort is needed to develop acquisition, tracking, and pointing (ATP) technologies for optical spacecraft applications. Bifocal Relay Mirror Spacecraft (BRMS), whose concept is shown in Figure 48, is a good example of the importance of developing these ATP technologies. The BRMS is composed of two optically coupled telescopes used to redirect laser light from ground-based, aircraft-based or spacecraft based lasers to distant points on the earth or in Space.
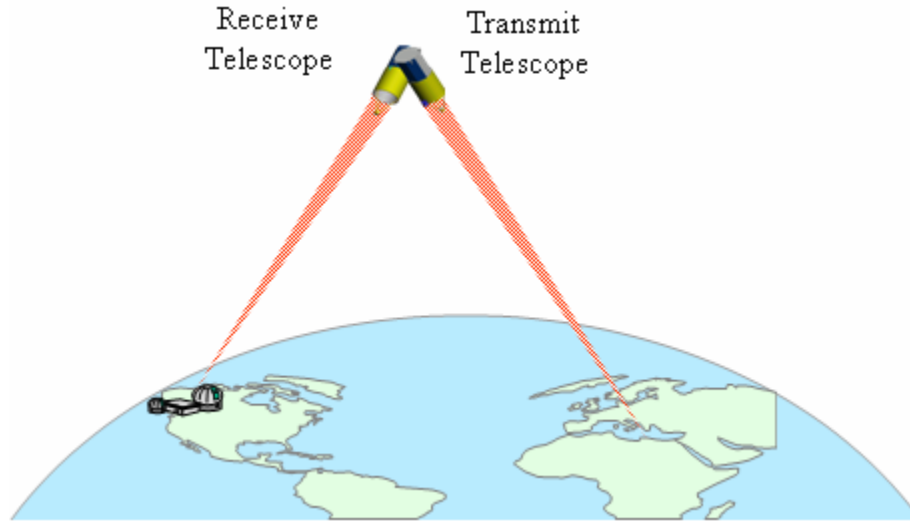
Figure 48 Bifocal relay mirror spacecraft mission.

The transmit telescope is attached to a majority of the spacecraft bus subsystems including the attitude control sensors and actuators. The spacecraft mass is 3300 kg at launch and the spacecraft orbit altitude is 715 km with an inclination of 40 degrees. The mission requirements are for a 3 meters spot beam on the ground, jitter less than 144 nanoradians (RMS) and mean dwell duration per pass of 250 seconds. The acquisition sequence consists of pitch and roll motion of the transmit telescope to acquire the target point. The yaw motion of the transmit telescope and the one axis motion of the receive telescope is used to acquire the receive point.

There are several unique multi-body pointing and control problems in the BRMS. The spacecraft has two large inertia telescopes that are gimbaled. This results in continual change in the spacecraft dynamics and spacecraft inertia during the operation. The BRMS also must slew the line of sight at a fast rate, as much as 180 degrees in a few seconds permitting laser relay to another relay mirror spacecraft. Therefore, high control actuation is required. Simultaneously, the vibrations and jitter must be reduced to optical tolerances. Therefore BRMS requires high bandwidth stabilization and tracking systems for beam control as well as the fast slew maneuver control for agile spacecraft maneuvers. The choice of actuators is a crucial element for the agile maneuver capability of the BRMS. CMGs are preferred actuators with high torque capabilities.

68

Ground simulation and testing of these techniques are highly desirable because it is extremely difficult to test and reconfigure the system once the vehicle is on orbit. Rigorous ground testing on spacecraft with optical payloads will significantly reduce the risk of the project. Spacecraft simulators are supported by a spherical airbearing to simulate frictionless rotation of a free-floating spacecraft. The airbearing-based testbed requires the center of mass location of the spacecraft is accurately aligned with the center of rotation of the spacecraft. Therefore, there is an added complexity of eliminating unnecessary gravity disturbance torque.
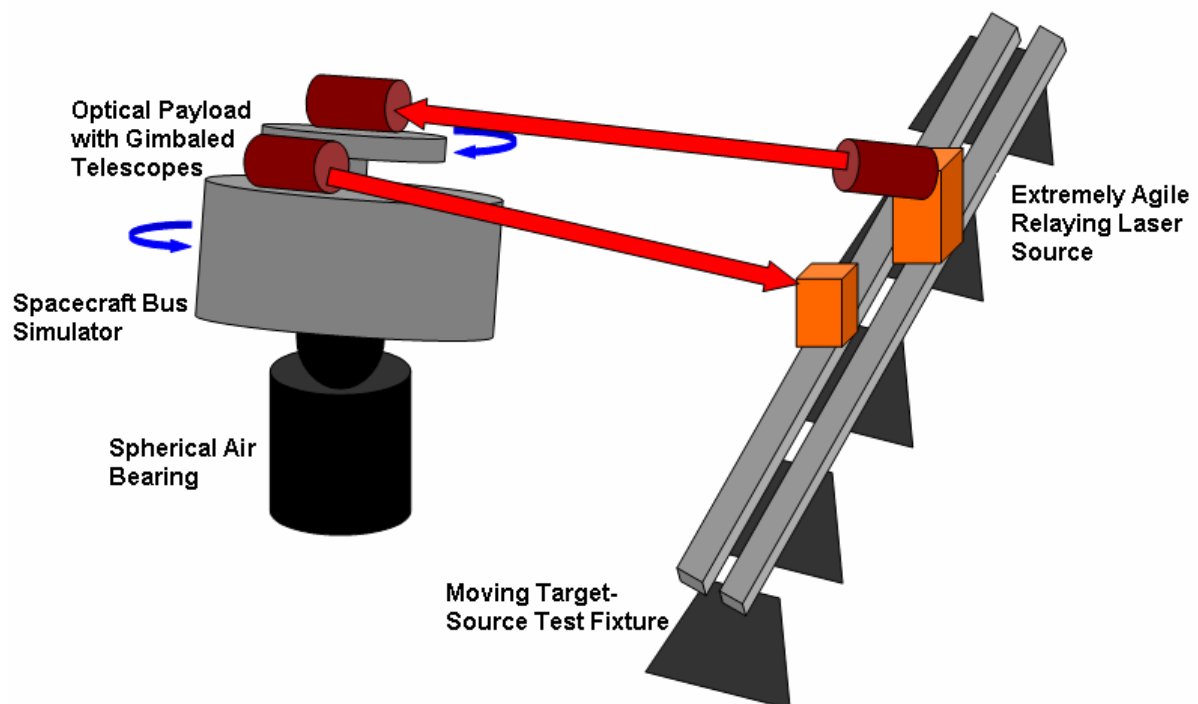
Figure 49 Spacecraft mission simulators.

Figure 49 illustrates the concept of the experimental testbed for the BRMS. The three-axis spacecraft bus simulator employs the optical payload including optically coupled receiving and transmitting telescopes. The laser beam from the laser source on a Moving Target-Source Test Fixture (MTSTF) is received by the top telescope and transmitted by the bottom telescope (fixed to the bus) to the target on the MTSTF. The top and bottom telescopes are connected by the rotational stage to allow the gimbaled motion.
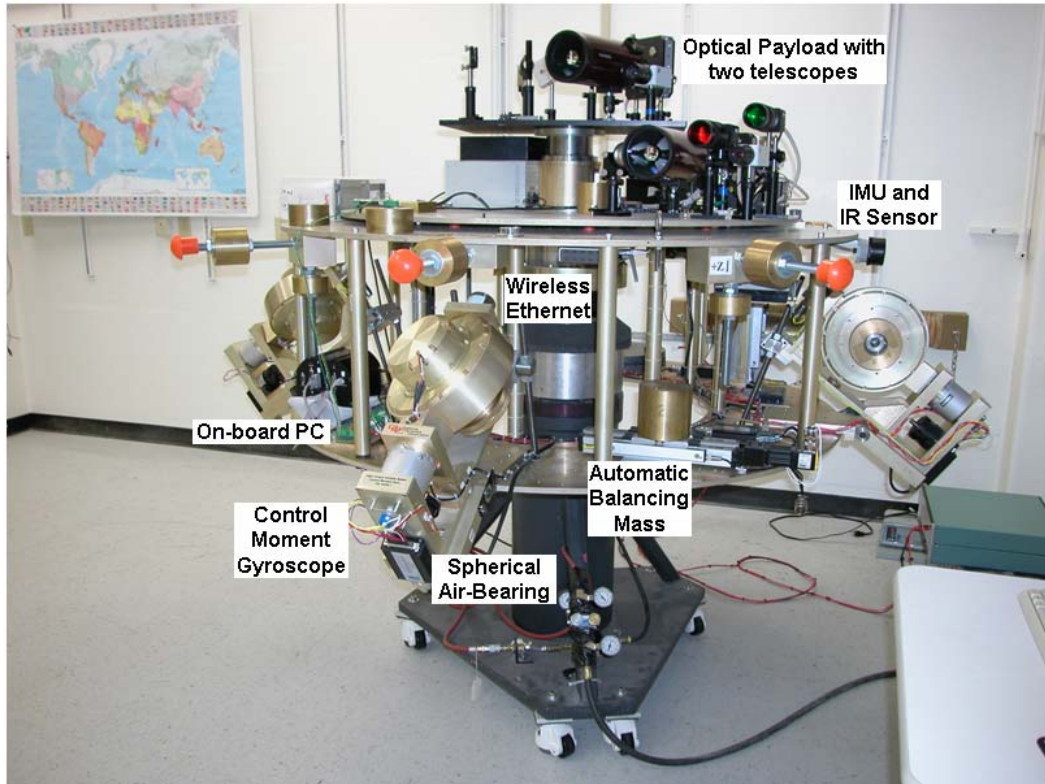
Figure 50 PHOTO: TASS2 Three-axis spacecraft simulator.

Description of the experimental hardware is based on [51] whose graphics were directly replicated here. Figure 50 shows the actual picture of the three-axis simulator named as TASS2. The spacecraft bus simulator is supported on a spherical air bearing to simulate a weightless environment. A thin film of compressed air is injected between a spherical ball and a mating spherical cup. This thin film of air creates an essentially frictionless lubrication layer between the ball and cup. When test articles, mounted to the ball segment are balanced, such that their aggregate center of gravity corresponds with the center of rotation of the ball, rotational motions of the ball and test articles match those of an object with similar inertial properties free falling though space. Because it is important to minimize the disturbance torque from any imbalance, three servo linear stages with lumped masses are employed for automatic mass balancing. The three linear stages are placed parallel to the three spacecraft body axes.

The maximum angular motion with this spherical bearing in roll and pitch is 45 degrees. However, in order to protect the hardware from damage during aggressive maneuvering, a bumper with a structural damper is installed on the bottom of the

spacecraft hub. Therefore, roll and pitch motion of the bus is limited to around 15 degrees. TASS2 has three variable speed control moment gyros (CMGs), Inertial Measurement Unit (IMU), two inclinometers (roll, pitch), on-board computer, IR sensor, and magnetometers for navigation and attitude control. The IMU consists of 3 Fiber Optic Rate Gyroscopes with integrated 3 translational accelerometers. The signals generated by the rate gyros, inclinometers, and IR sensor have two characteristics that make them difficult to utilize. First, the measurements are noisy, and this noise is significant at the near-zero rates encountered during normal operation. Second, the gyro experiences a bias that slowly varies during operation, and varies widely day-to-day.

Variable Speed Control Moment Gyroscopes (VSCMGs) are selected as main attitude control actuators for its high torque capacities. The testbed is equipped with four VSCMGs allowing several extra degrees of freedom to accommodate various CMG singularity avoidance techniques. In this study, the more challenging approach is taken utilizing only three (non-redundant) CMGs operated in *fixed-speed mode*. Each CMGs has a maximum angular momentum of 22.5 N-m-s and a maximum torque of 12 N-m at 2500 RPMs. The simulator electronics subsystem is an integration of power control switch box, power switching and control electronics, and industrial PC. The power control switch box has a main power switch and individual switches for CMGs, IMU, top-deck control, and the automatic mass balancing system. It also has an interface with an external power supply. Power switching and control electronics interface CMG controllers, IMU, IR sensor (not used), and inclinometers. The PC104 industrial PC has an analog input and output ports as well as digital out ports to send the commands and receive various data from control electronics. The main control program is coded in the host computer using MATLAB/SIMULINK. Real-time control software is communicated between the host computer and target PC104 industrial PC via wireless Ethernet connection.

The optical system of the testbed is composed of the Extremely Agile Relay Laser Source (EARLS), TASS2 upper deck optical payload with receiving telescope, TASS2 lower deck optical payload with transmitting telescope, and diagnostic target board. The EARLS and the target board are mounted on separate linear tracks in the MTSTF as shown in Figure 51.
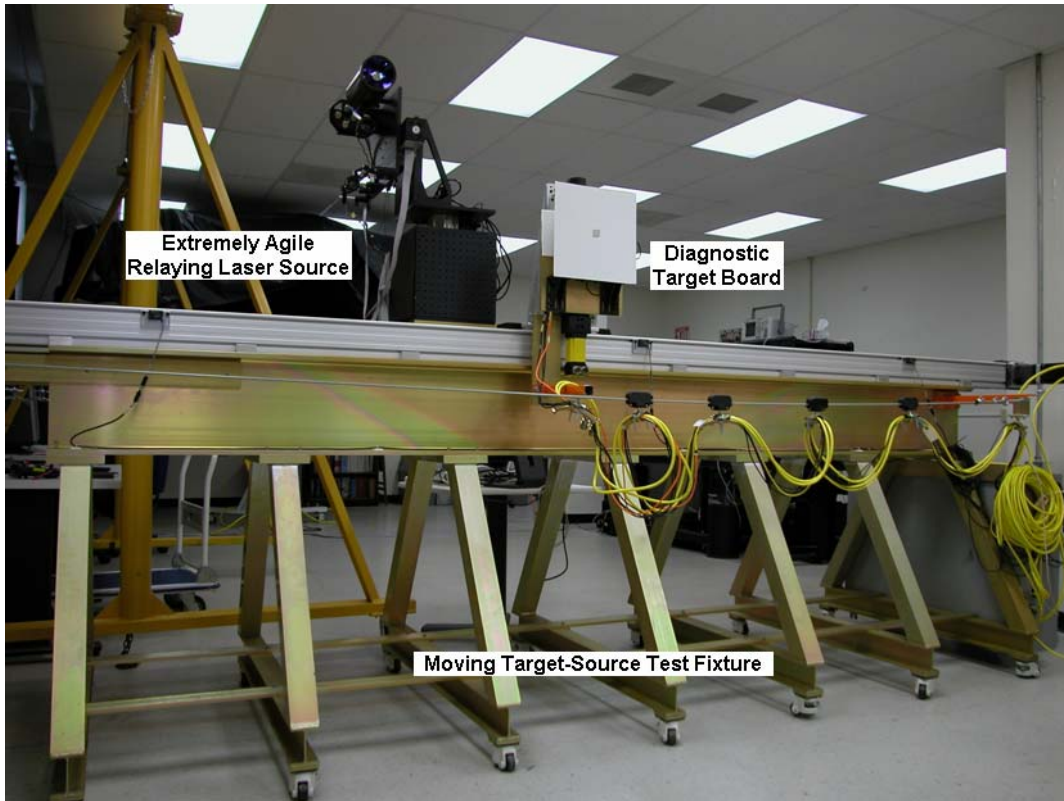
Figure 51 PHOTO: Moving Target-Source Test Fixture with Laser Source and Target.

B.   THREE-AXIS SATELLITE SIMULATOR

Notice in Figure 52 - Figure 53 the satellite simulator is composed of a spacecraft bus (bottom) with an optical payload mounted on the upper deck. Initial inertia estimates used in the adaptive control presented earlier were values experimentally estimated *prior to* installation of the upper payload deck. The upper payload deck is fixed to the satellite, so the spacecraft attitude control system must guarantee the payload bore sight is maintained. The ground/air/space based source laser is received through the lower telescope and optically relayed to the upper telescope for transmission to the target. The upper telescope is mounted on a small platform that gimbals with respect to the spacecraft and lower payload deck. This fourth degree of freedom allows the spacecraft to maintain source laser pointing in three dimensions and simultaneously track a moving target.

At the rear of each telescope note fast steering mirrors provide extremely fine (µrad) pointing control as long as the correct bore sight is maintained by the spacecraft

(keep the laser on the mirrors). A jitter sensing position sensing device (PSD) is provided on the upper deck to allow fine control pointing algorithms to remove jitter. Sensors and multiple electronics boxes are mounted on the underside of the top deck (pictured below). Sensors include inclinometers, magnetometers, sun sensors, and star sensors for angle with ring laser gyroscope (inertial measurement unit) for angular rate. Payload cameras also sense source laser beacons and targets. Actuators include control moment gyroscopes, balancing mass actuators, fast steering mirrors and a motorized drive to gimbal the optical deck. Numerous electronic busses control electrical signals and power to each device and interaction with desktop computers running MATLAB/SIMULINK is provided by XPC Target through a wireless router.
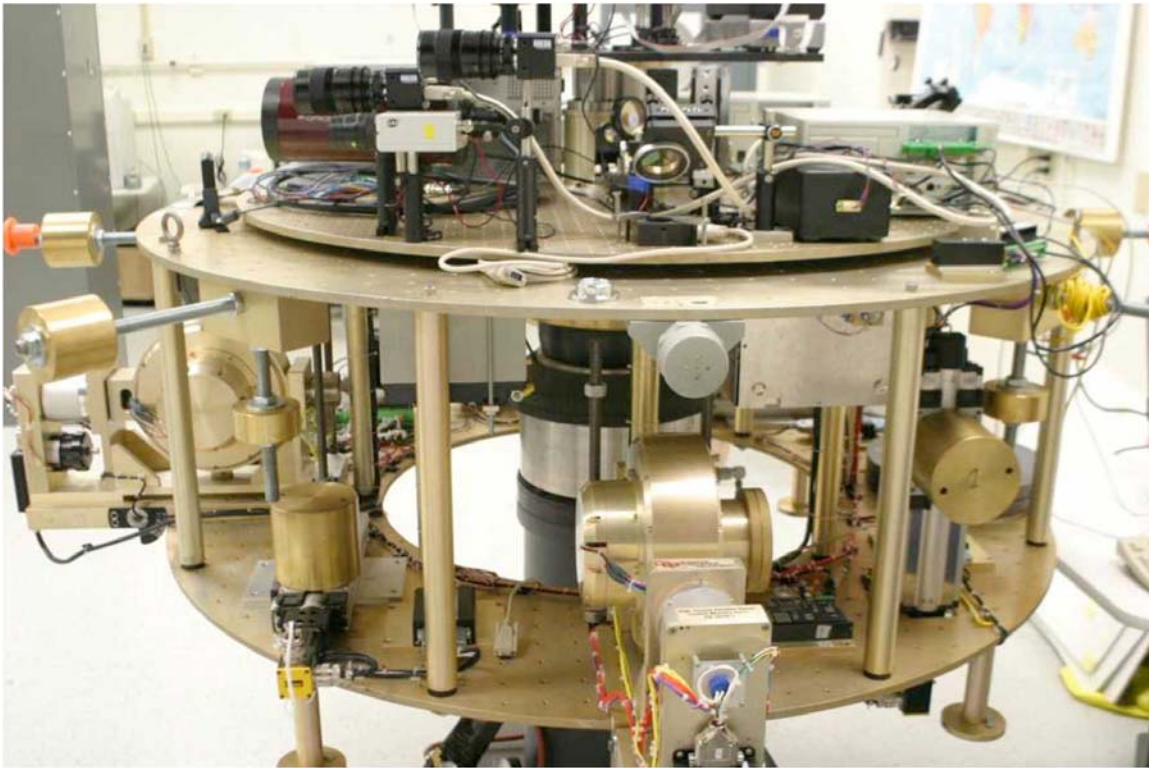
Figure 52 PHOTO: Three-axis satellite simulator 2 (TASS2).

Photograph on TASS2 free-floating experimental testbed at the Naval Postgraduate School
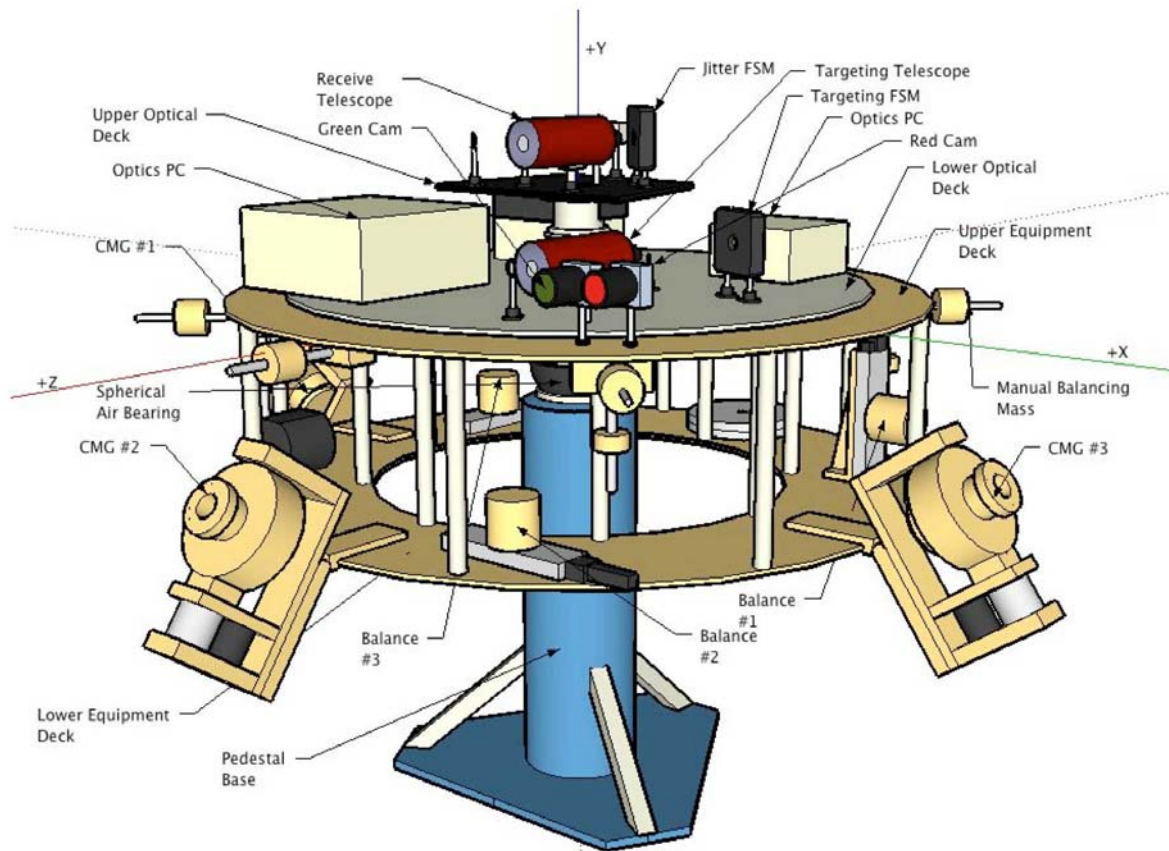
Figure 53 CAD: Three-axis satellite simulator 2 (TASS2).

Equipment location on TASS2 free-floating experimental testbed at the Naval Postgraduate School

Hardware	Nominal performance specification
CMGs	24.4 N-m-sec at 2800 RPM
	Resolution: 182 counts/ degree
IMU	Max bias=0.35°/hour;
	$\sigma_{\dot{\phi}} = 0.28$ rad/sec, $\sigma_{\dot{\theta}} = 0.26$ rad/sec, $\sigma_{\dot{\psi}} = 0.26$ rad/sec

Table 5 TASS2 key sensor/actuator specifications summary.

1.   Sensors

Experiments presented here integrated rate data from the ring laser gyroscopes (inertial measurement unir or IMU). A Northrup Grumman LN-200 fiber optic gyro

(FOG) with silicon accelerometers provides inertia angular rate measurements with a minimum spin up time of 0.8 sec with maximum accuracy achieved after 5 seconds. Maximum bias variation is 0.35°/hr with a repeatability of 1-10 $^{\circ}$/hr (1σ). The IMU interface is mounted underneath the top plate. Power to the IMU interface is applied by switching the IMU switch on the switchbox. The IMU interfaces converts the synchronous custom protocol IMU data (LN-200 data) to asynchronous RS-422 data for the FCU (via the power switching electronics).

2. Actuators

Three 24.4 N-m-sec (at 2800 rpm) GDC single-gimbaled, variable-speed control moment gyroscopes (Figure 54) are the main spacecraft attitude actuator. Rotor speed and gimbal controllers were made by ACEI. By fixing the rotor speed controller and gimbal controllers, the CMGs can act like reaction wheel. Variable speed was not used in this study by fixing the rotor speed but allowing the gimbals to move. Gimbal angle feedback is provided by the gimbal motors position encoder.
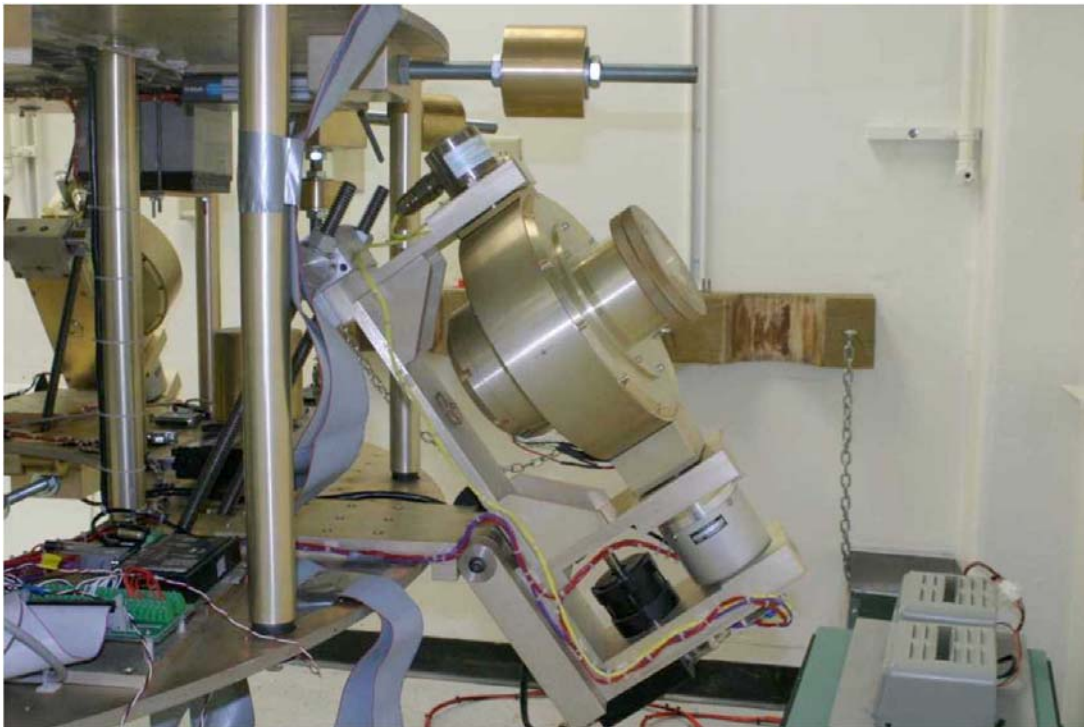
Figure 54 PHOTO: Control moment gyroscopes:

GDC single-gimbaled, variable-speed control moment gyroscope

3.   Electronics and Electrical Power

The TASS2 electronics package is an integration of four electronic box types and one industrial embedded computer on the spherical air bearing, a battery charger and a desktop XPC host computer are located off of the platform. The electronic boxes on the platform consist of a sun sensor/power switching electronics assembly, an RF model (wireless Ethernet hub), 4 CMG controllers and a switch box. The power system consists of the switchbox, charger, and two gel cells 12V 24Ah lead acid batteries. The power system is rated to operate at 100A of current. The bus voltage is a nominal 24.8V and is rated to operate down to 18.5V at which the switchbox will automatically disconnect power from the power bus to protect components. With all the components in the system powered up, the system draws 3.6A (no torque applied to the CMG rotors). At this current, the system is capable of running for over six hours without recharging. Additional power required to torque the rotors would shorten this time. It is possible to charge the batteries while running the system from external power, so that while preparing to run an experiment, the batteries do not have to be depleted. This may be done by connecting the power umbilical to the front switchbox with the big red switch in the "in" position. The batteries may not however be charged while the system is running off of the batteries. There is also the ability to power the CMG rotors from battery power while running all the other components from external power by simply keeping external power applied when switching to internal power.

The power switch box is the main user interface for powering the individual components of the TASS2. It also controls the type of power to be used on the platform ("on board" battery power or external power from the external source). It is also used as the interface for the charger unit. The switchbox has digital displays for the system voltage and current. It also provides protection against low voltage operation (which may damage some system components), as the built-in switchbox will remove power from all components if the system voltage drops below 18.5V. It is recommended that the system is powered from external power whenever possible to insure that there is adequate power when a simulation is to be run. All systems can be powered from external power with the exception of the CMG rotors (although gimbals and controllers will still function if not attempting to spin the rotors up/down). CMG controllers are mounted to the outside edge

of the CMG mechanical hardware. The CMG controllers are the interface between the control unit (via the power switching electronics) and the gimbal motor on the CMGs as well as the analog command to the Emoteq brushless motor drive for the CMG rotor. The CMG controllers also provide an analog feedback for the gimbal position and rate. Analog information is provided by a conductive plastic potentiometer (Bourns P/N – 6639S-1-502) with +5V excitation. Power to the CMG controllers is applied by switching the CMG switch in the switch box. The CMG controller uses serial command inputs, and also has analog input capability to control the CMG it is wired to. The Emoteq brushless motors are designed for high torque to inertia and size ratios and contain high energy neodymium iron boron magnets, samarium cobalt magnets for operation in harsh environments, and Hall-effect sensors for commutation. Hall-effect sensors are integral to the motor and require no setup on the part of the user.

Three leveling mass interfaces (ACEi PN# NPS-05413) in are mounted on the lower equipment deck near the linear actuator they control. The leveling mass interfaces are the interface between the FCU via the power switching electronics and the linear actuator motors. Power to the leveling mass interfaces is applied by switching the BALANCE switch on the switch box. The leveling mass interface uses serial common inputs to control the linear actuator it is wired to. All three controllers are identically controlled, but the vertical actuator also automatically controls a brake to prevent the mass from sliding (due to gravity) when the controllers are off. The controllers can save the last "home" position to non-volatile memory, so that when a controller is powered up, it can find the last saved position (this can be reset to dead center of the actuator also).

Power to the Ethernet wireless transceiver is applied automatically upon system power up. Initialization is automatic and requires no user interaction. The wireless Ethernet transceiver allows wireless communication via TCP/IP protocol of xPC data to the host PC located off the platform. It is a standard commercial 802.11b(Dlink) wireless Ethernet switch.

The industrial embedded computer uses a data acquisition interface via MATLAB XPC to read in analog sensor measurements, and the RS-232 communications port to communicate with the power switching electronics. The computer uses 2 analog cards

77

(Diamond MM32, and the Diamond Ruby MM8) to input sensor data, and output analog commands, such as CMGs when in analog mode. The computer is based on the Intel Pentium III 750Hz platform running xPC for on-board – remotely updateable control.

4.   **Mass Balancing**
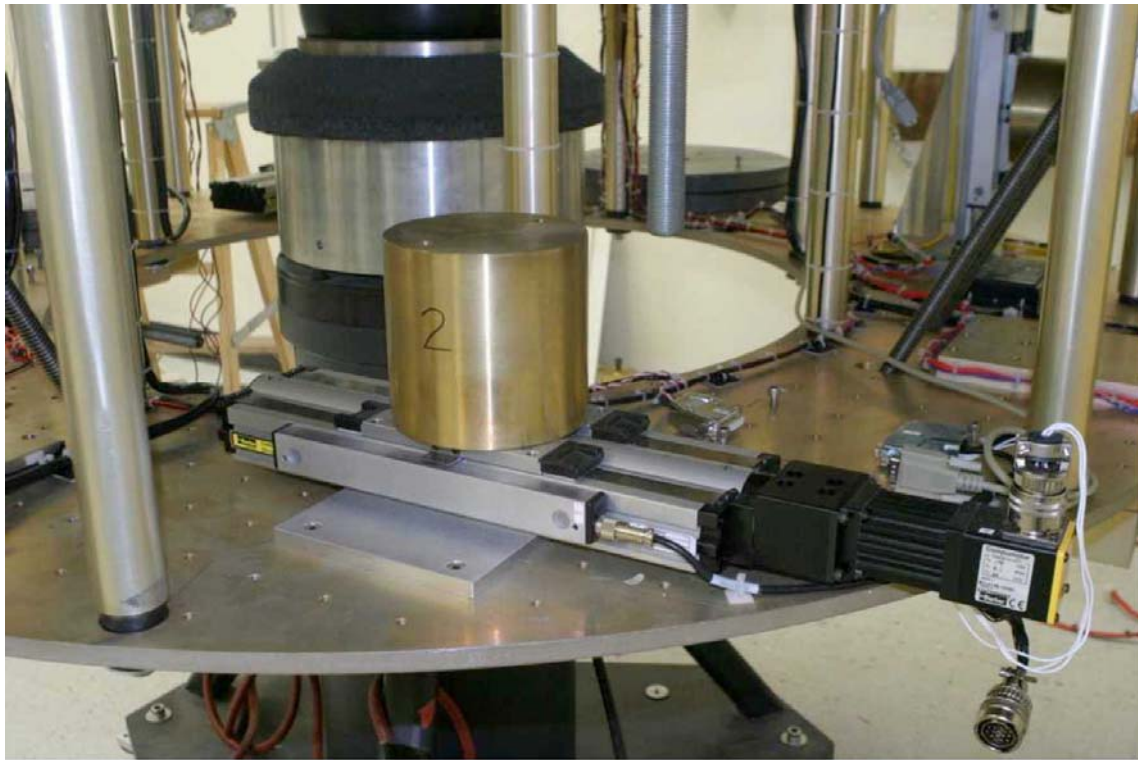
Figure 55 PHOTO: Mass balancer.

IV. EXPERIMENTAL RESULTS

A. ACQUISITIONS MANEUVERS EXPERIMENTS

1. Optimal Singularity Free Momentum

Experimental verification is performed to demonstrate singularity free operations. A $+5^o$ degree yaw maneuver in 4 seconds is followed by a -5° yaw maneuver in 4 seconds. The attitude is regulated to zero. The CMG continues to output significant torque to counter dramatic gravity gradient disturbances typical of imbalanced ground test spacecraft simulators. This maneuver has been previously performed using a skew angle of 57 degrees (not depicted). The CMG array became singular and attitude control was lost motivating this study. Skew angle was increased to ninety degrees for all three CMGs, and the identical experiment was repeated. The resultant experimental momentum trajectory is placed in the context of the theoretical singular momentum space for easy visualization. Notice in Figure 56 that the maneuver is performed and the testbed is regulated for 5 minutes without striking any singular surfaces. Momentum magnitude and the inverse of the condition of the [**A**] matrix verify this assertion. Thus, the singularity-free approach has been demonstrated not to spoil tracking accuracy at least within the current attitude and rate sensing accuracy of the testbed.

Notice what happens when the same momentum trajectory is placed in the context of the theoretical singular momentum space of the "optimal spherical" skew angle, $\beta=54.73^o$ (Figure 58) which shares a very similar momentum space appearance as the previously used $\beta=57^o$. The internal singular surfaces are depicted individually for ease of visualization. This momentum trajectory is constantly close to the internal singular surfaces and strikes an impassable singular surface. A corresponding impassable singular surface exists for a skew angle of 57°. Prior experiments using 57° went singular and resulted in the loss of attitude control when the momentum trajectory struck this corresponding impassable singular surface.
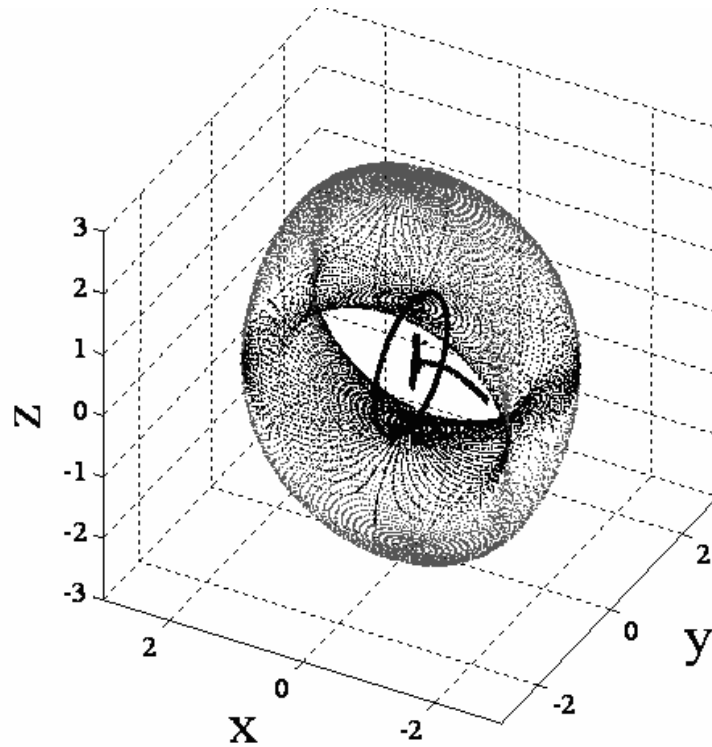
Figure 56 EXPERIMENT: Optimal configuration.

$+5^{\circ}$ yaw in 4 seconds, -5° yaw in 4 seconds, then regulate at $\{x,y,z\}=\{0,0,0\}$ countering cg-offset disturbance torque of unbalanced ground test satellite simulator. Momentum trajectory placed in context of theoretical singular momentum hypersurface of $\beta_i=90^{\circ}$ configuration.
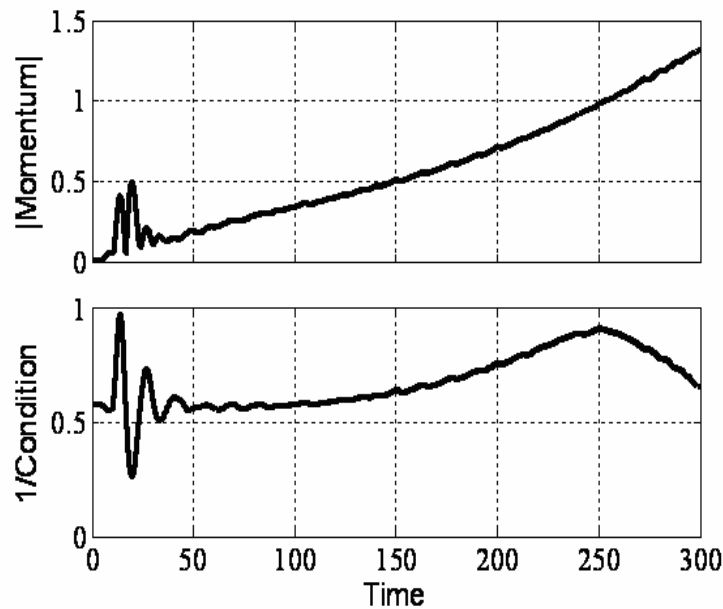
Figure 57 EXPERIMENT: Optimal Configuration.

$+5^{\circ}$ yaw in 4 seconds, -5° yaw in 4 seconds, then regulate at $\{x,y,z\}=\{0,0,0\}$ magnitude of normalized momentum and inverse of condition number of [A] matrix (would approach zero if array became singular).
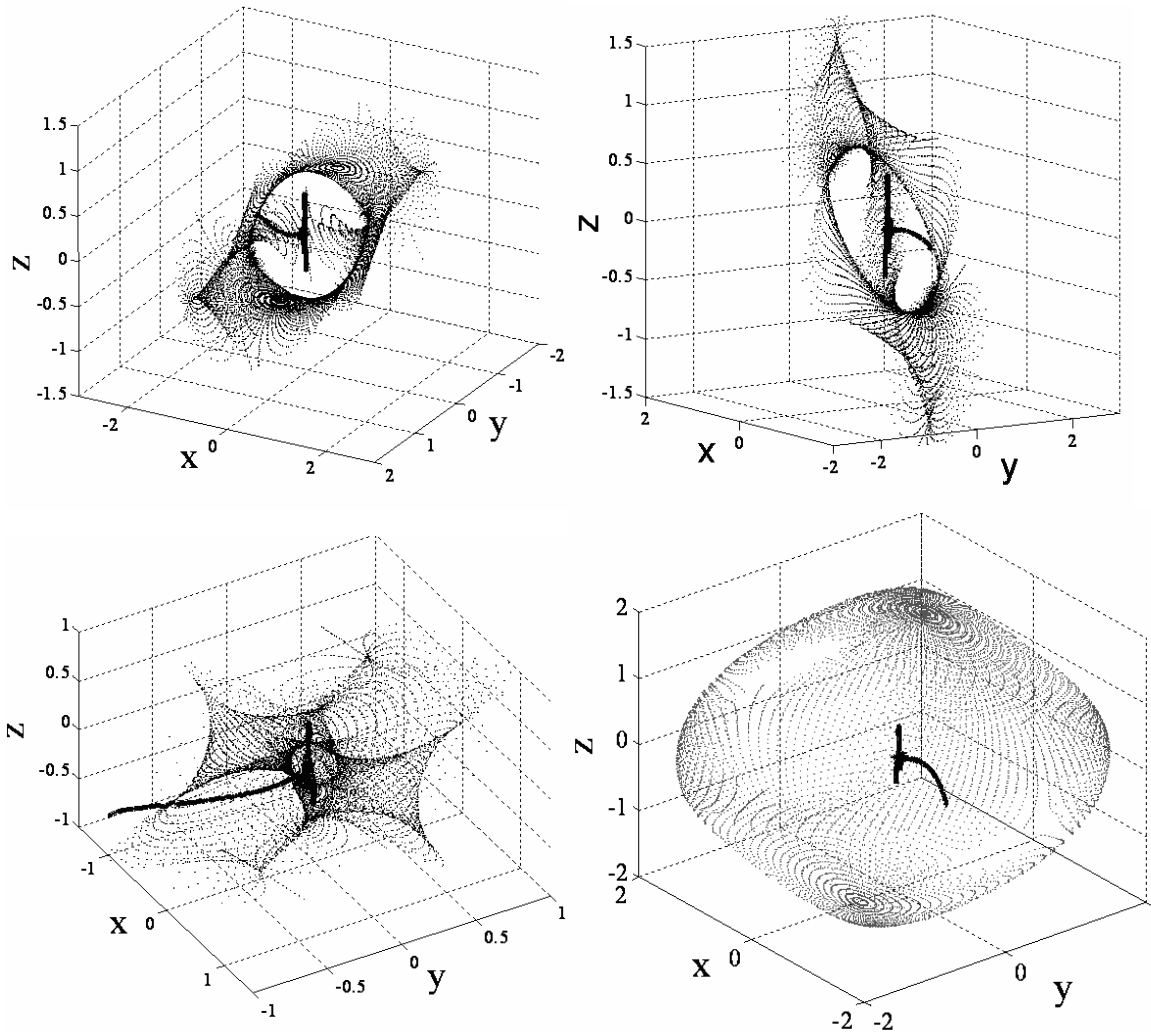
Figure 58 EXPERIMENT: Configuration comparison.

Experiment from Figure 56 performed in β_i=90° configuration placed in context of "optimal spherical" β_i=54.73° for the purpose of comparison. Note continuous flirting with singular surfaces and impact with impassable surface occurs less than ¼ way through trajectory. This trajectory would not have continued as depicted had the skew angles been β_i=54.73° , instead the array would have gone singular and attitude control would have been lost.

2.   Max Momentum Reorientation with Mixed Skew Angles

Next, experiments were performed with mixed skew angles to orient the maximum momentum capability about the yaw axis as seen in Figure 59. The maneuvers were increased 325% in the same duration from 4*ᵒ* to *13ᵒ* in only 4 seconds. This demands significantly more momentum change specifically about yaw. The momentum is achieved singularity free and maneuver is performed without incident.

81
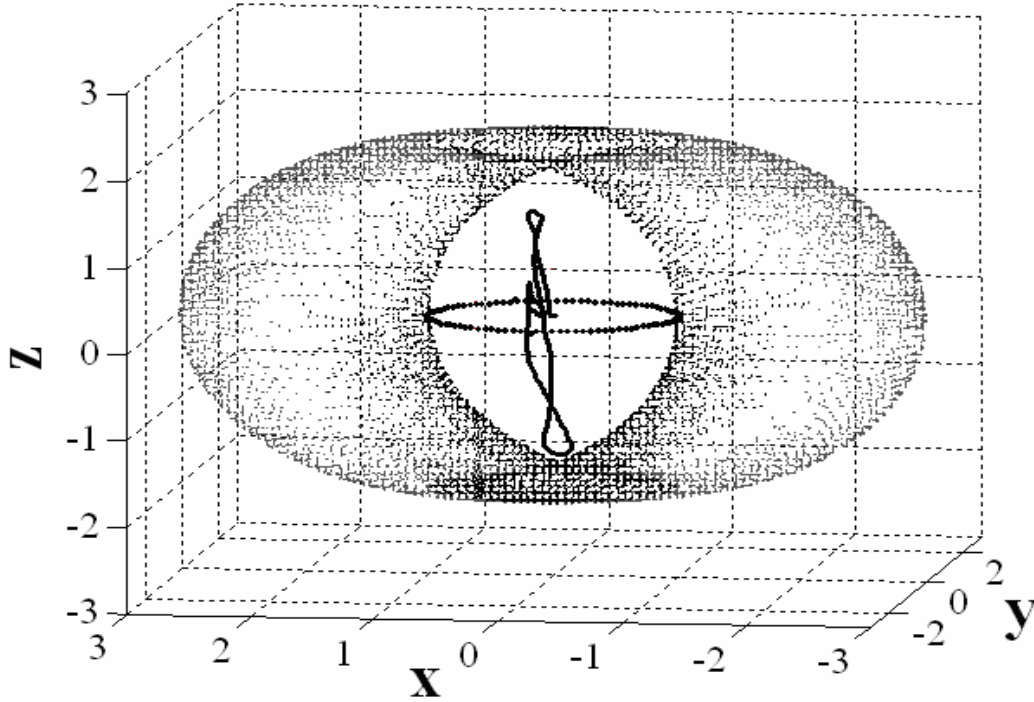
Figure 59 EXPERIMENT: Mixed skew angles.

+13° yaw in 4 seconds, -13° yaw in 4 seconds performed in $\{\beta_1,\beta_2,\beta_3\}=\{90^O,0^O,90^O\}$ mixed skew angle configuration. Momentum trajectory placed in context of theoretical singular hypersurface.
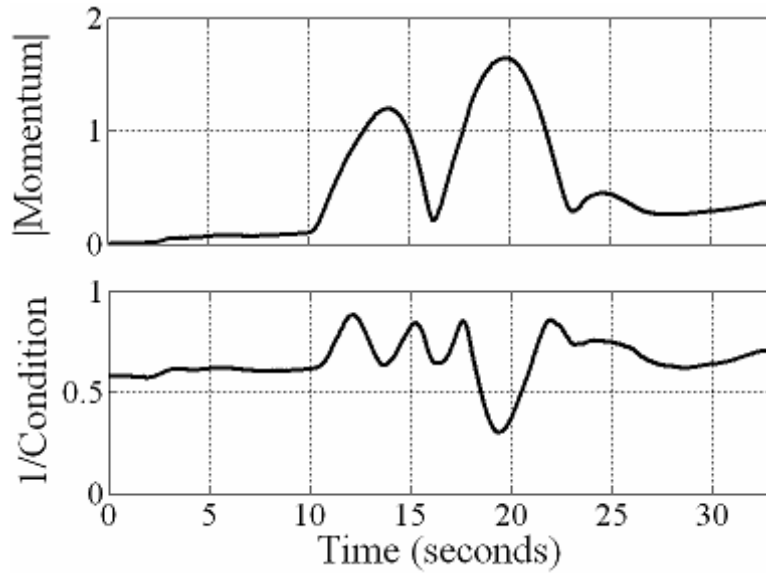
Figure 60 EXPERIMENT: Mixed skew angles.

+13° yaw in 4 seconds, -13° yaw in 4 seconds performed in $\{\beta_1,\beta_2,\beta_3\}=\{90^O,0^O,90^O\}$ mixed skew angle configuration. Maneuver momentum and inverse condition of [**A**].

3. Singularity Avoidance: Generalized Singularity-Robust Inverse

Singularity avoidance was implemented per ref [17],[23] for experimental regulation of three-axis satellite simulator 2 (TASS2) $\beta=57^{o}$ skew angles with generalized singularity robust steering law and quaternion feedback control [52]. TASS2 has center-of-gravity offset disturbance that must be countered by the three CMG array. The testbed was floated on the spherical air bearing at 60 seconds. The initial gimbal angles were [0°, 120 ^{o}, -60 ^{o}]. The resulting attitude angles of Figure 1shows that the system became unstable after ~150 seconds of regulation (Figure 61). Although total momentum is with in the momentum envelop, it cannot produce more momentum for a specific direction, due to singularity (magnitude of momentum from each CMG is normalized to 1). Notice the corresponding gimbal angles during singularity are erratic. Singular values of A matrix verify that singularity avoidance effectively keeps the [**A**] matrix from becoming singular, but it cannot penetrate the elliptical singularity. This is the motivation for alterative singularity reduction and penetration.
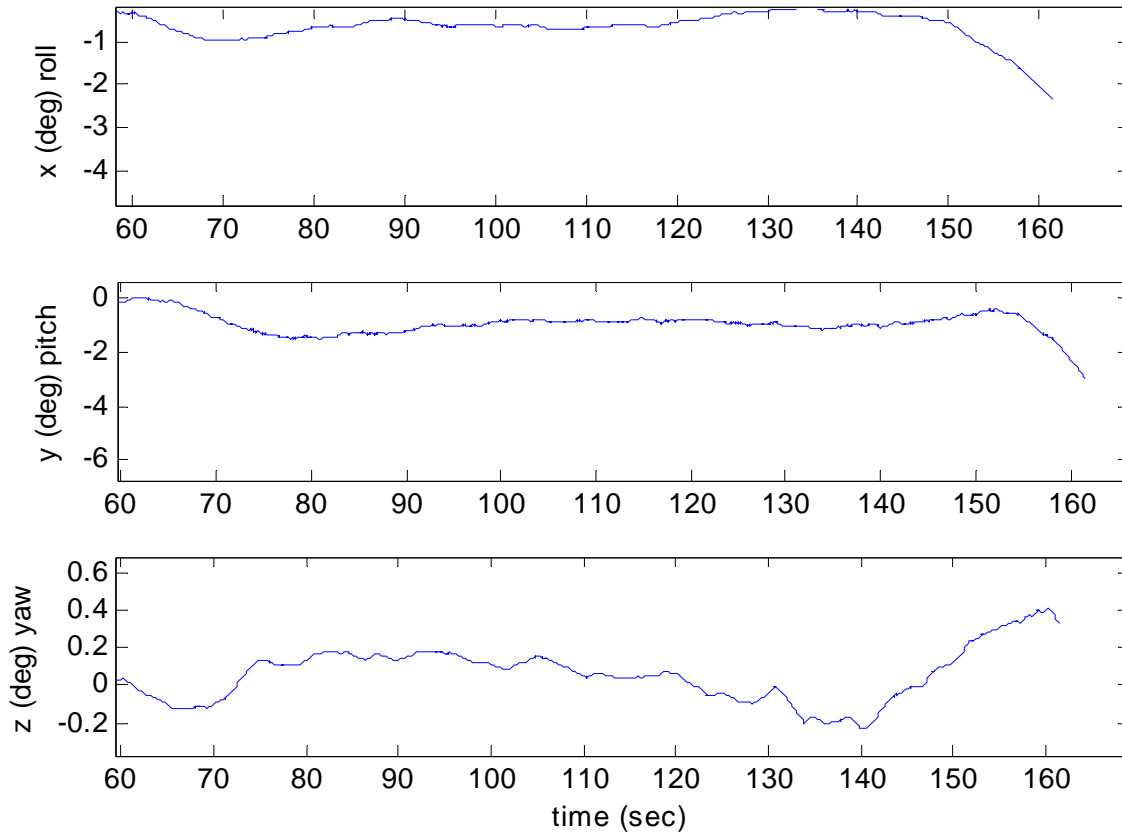
Figure 61 EXPERIMENT: SR Inverse actual attitude Angles.
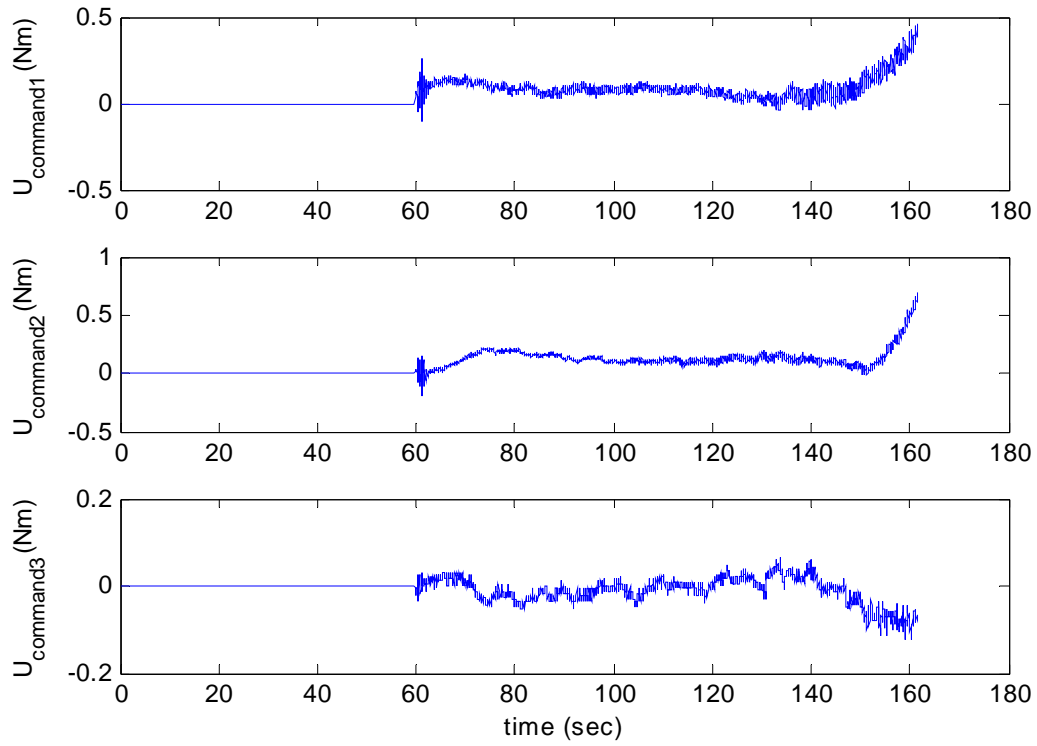
Figure 62 EXPERIMENT: SR Inverse commanded control torque.
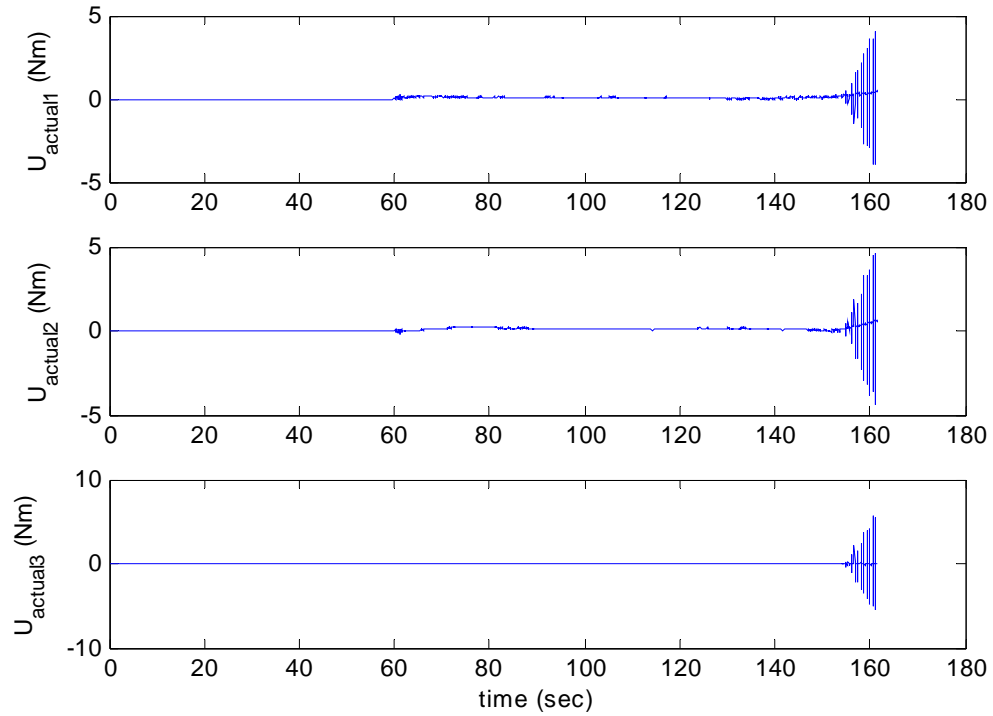
Figure 63 EXPERIMENT: SR Inverse actual control torque.

84
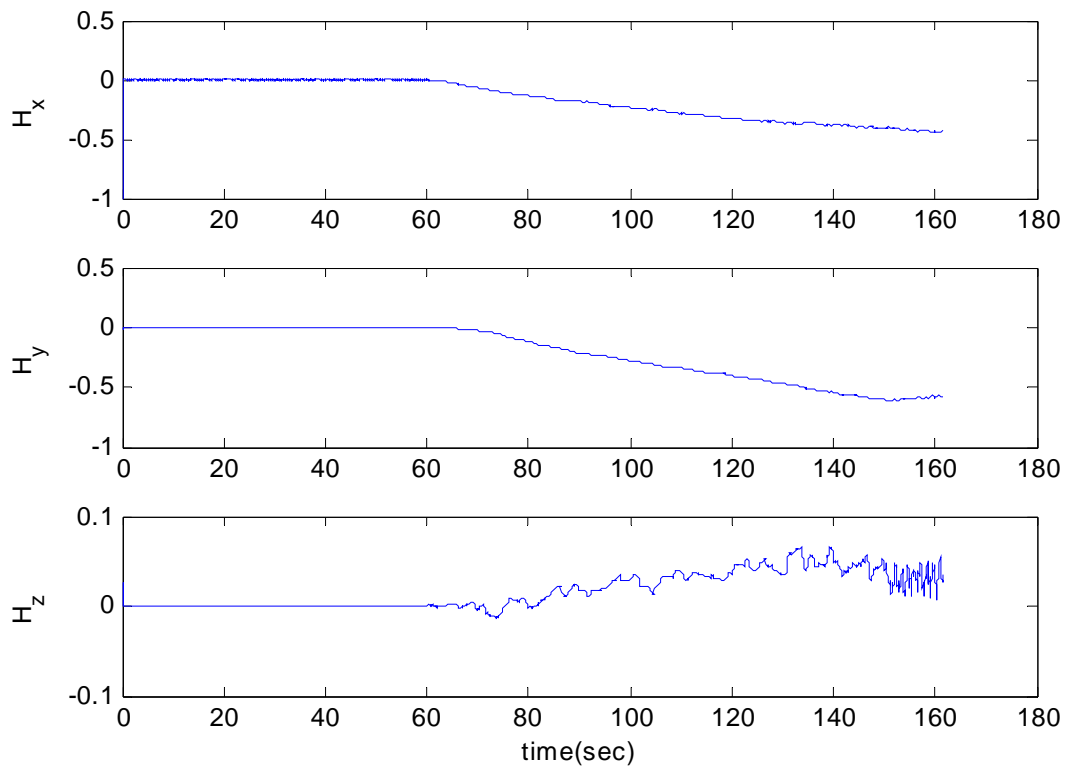
Figure 64 EXPERIMENT: SR Inverse normalized momentum.
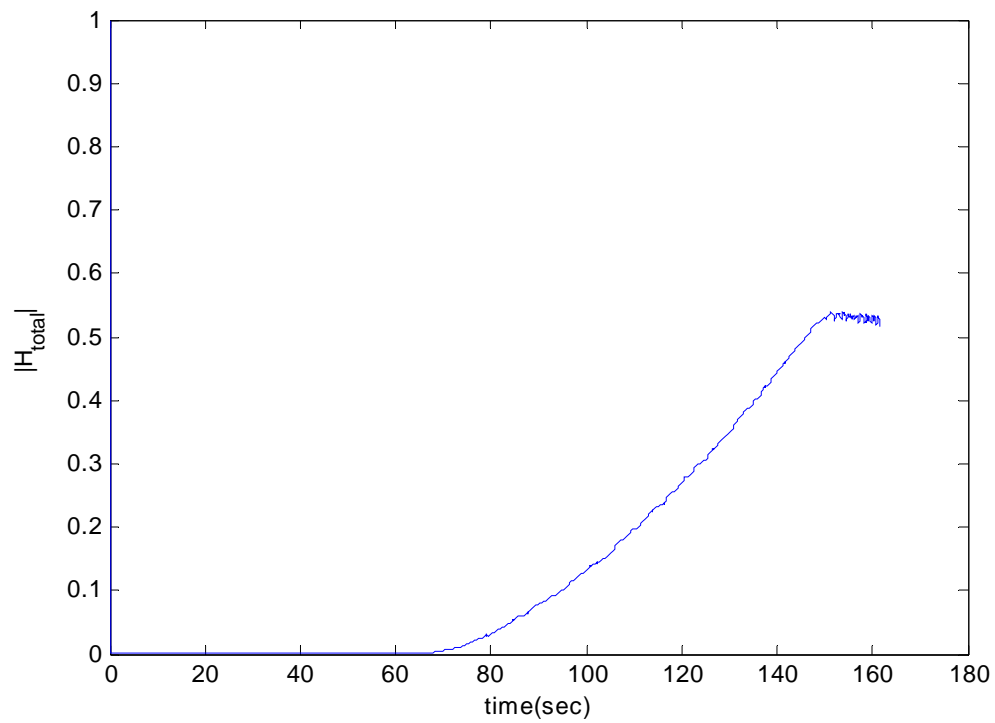
Figure 65 EXPERIMENT: SR Inverse normalized momentum magnitude.
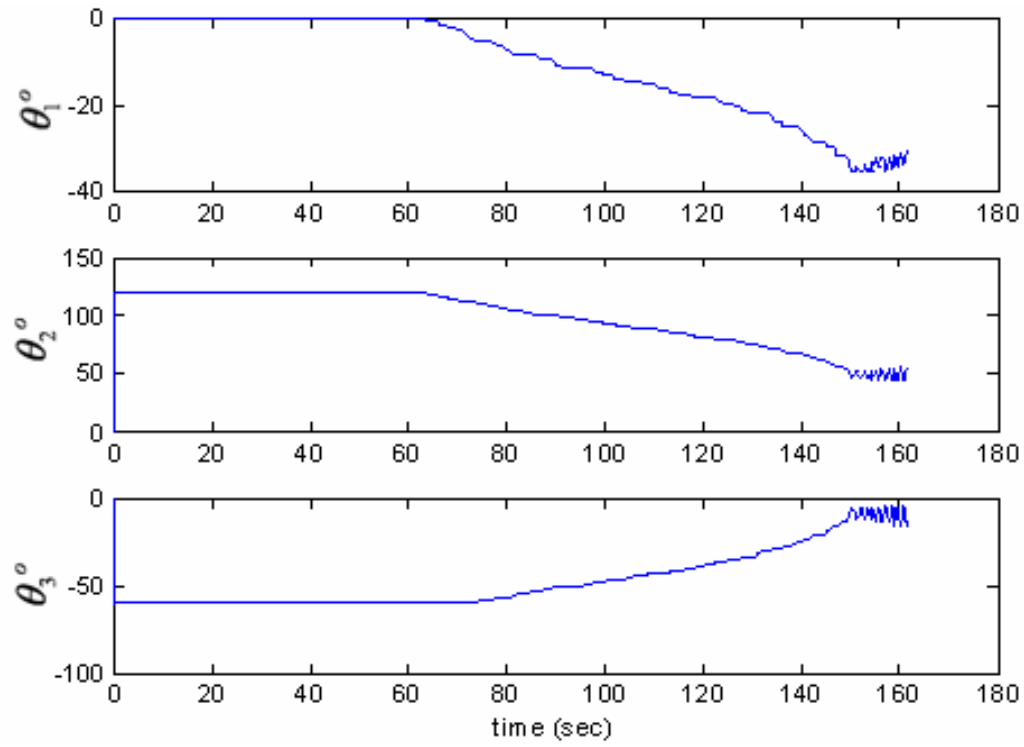
Figure 66 EXPERIMENT: SR Inverse gimbal angles.
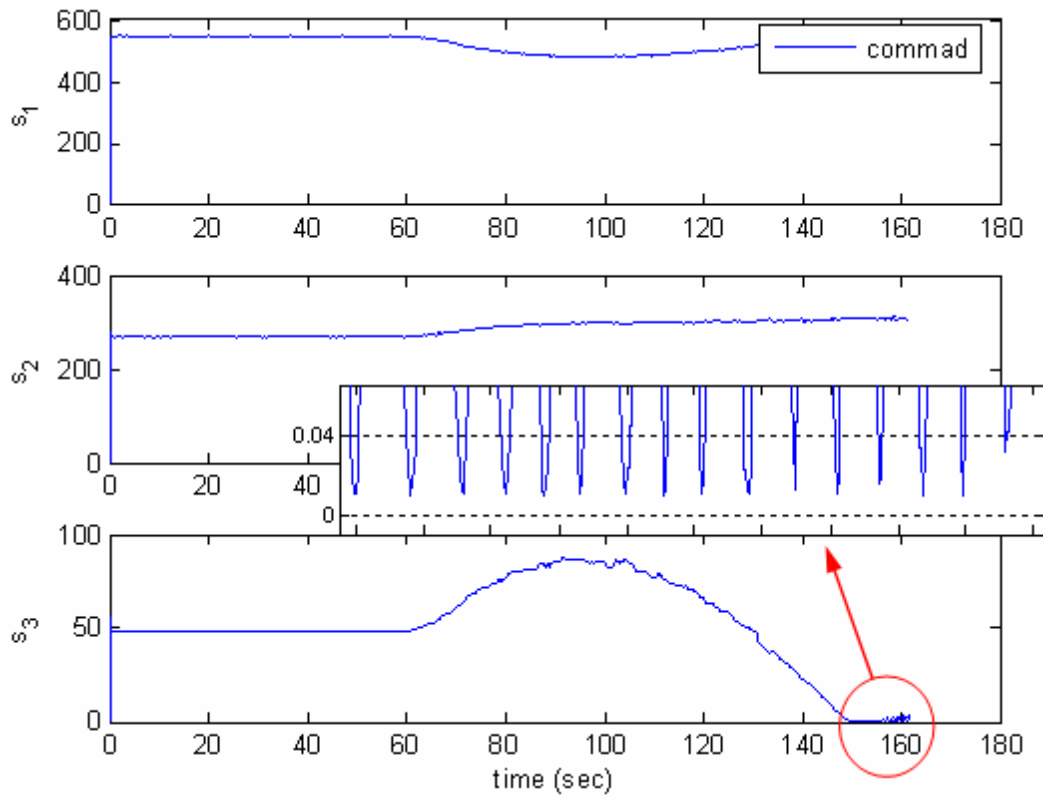
Figure 67 EXPERIMENT: SR Inverse singular value of [A] matrix.

86

4. Singularity Reduction with Decoupled Control Steering

Experiments were performed with decoupled control to maximum momentum capability about the yaw axis. First note Figure 68 displays the ability of decoupled control steering to penetrate the singular surface associated with the coupled [A] matrix of CMG gimbal angles and skew angle. This attribute is exploited with an aggressive yaw maneuver (Figure 69). The commanded maneuver angle from [2] was increased 700% from $\pm5^o$ in 4 seconds to $\pm35^o$ in 10 seconds. This demands significantly more momentum change specifically about yaw. Figure 70 displays the required maneuver is achieved without incident. Notice that the *coupled* [A] matrix was singular twice during this drastic maneuver.
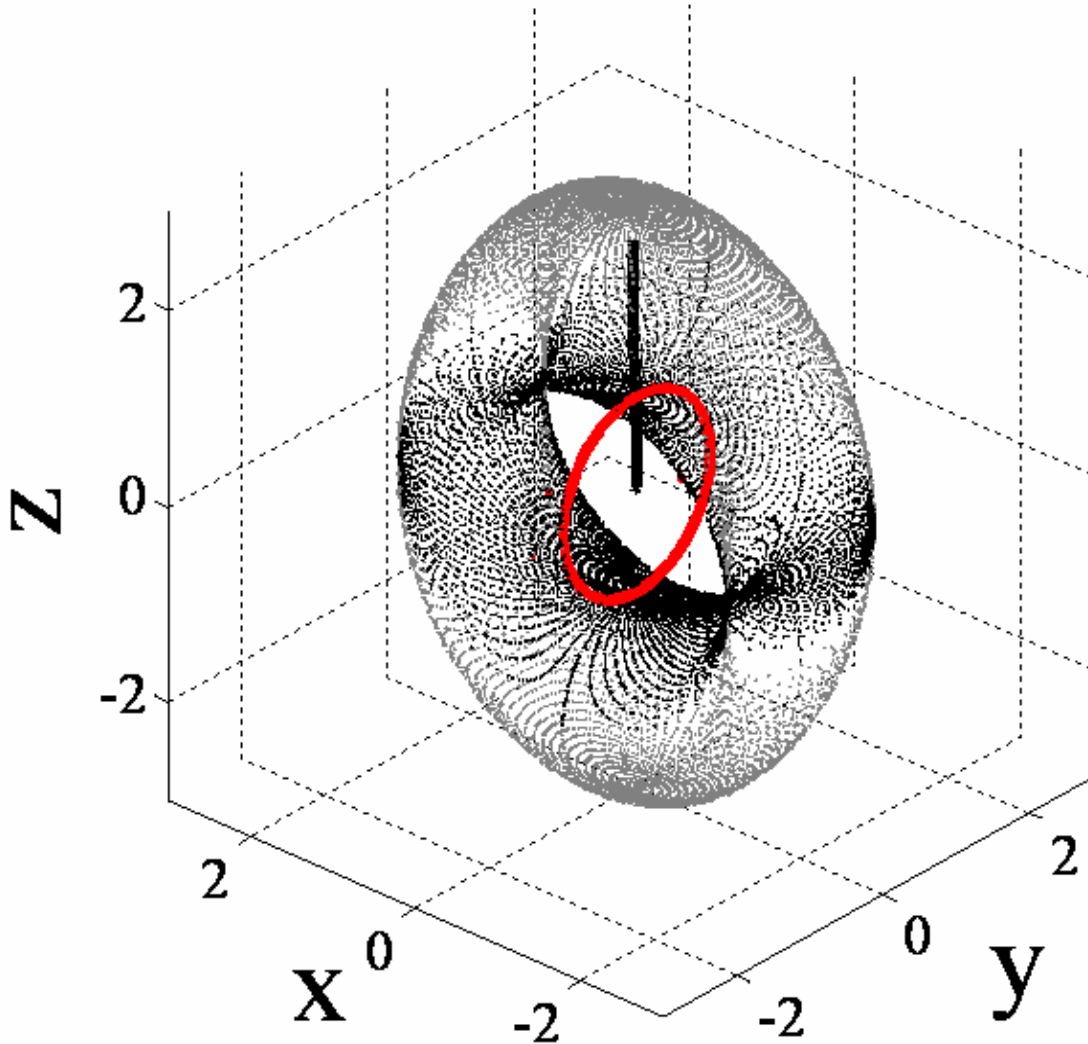
Figure 68 EXPERIMENT: Decoupled control.

Demonstrate ability to pass cleanly through the singular surface at 1H using proposed decoupled control.
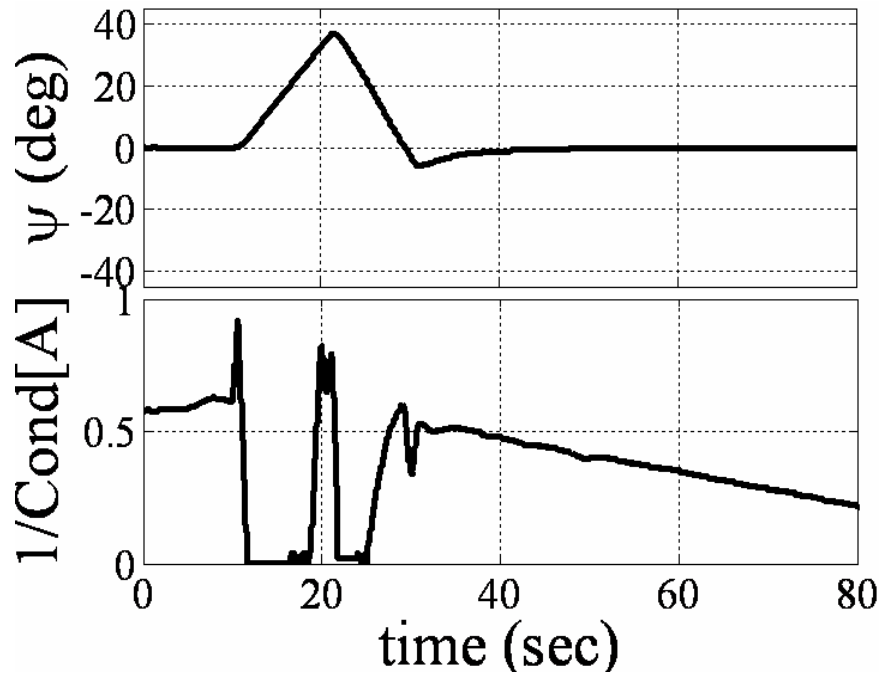
Figure 69 EXPERIMENT: Decoupled control yaw angle.

Yaw Euler angle (top) and 1/cond[A] (bottom) versus time (secs) for $+35^{\circ}$ yaw in 10 seconds, -35° yaw in 10 seconds performed with decoupled control steering
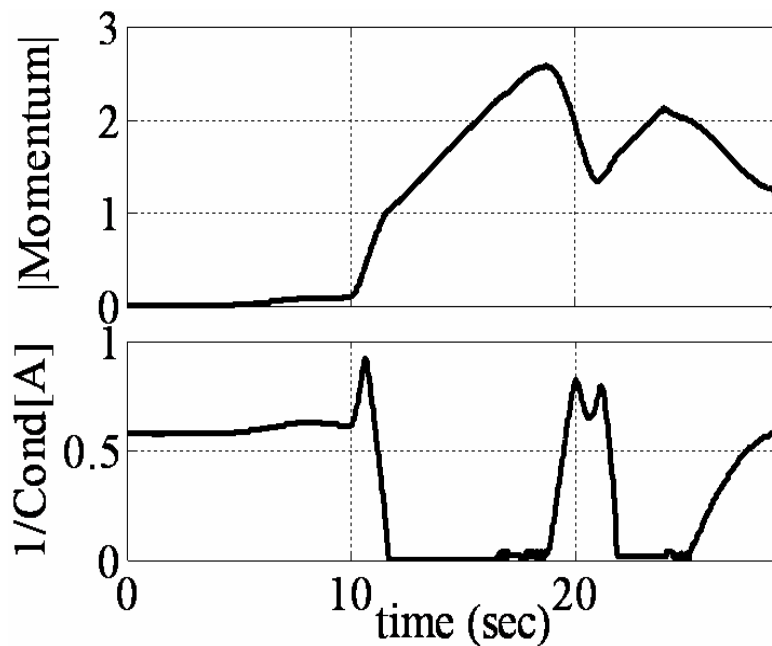
Figure 70 EXPERIMENT: Decoupled control momentum.

Momentum Magnitude (left-top) and 1/cond[A] (left-bottom) versus time (seconds) for $+35^{\circ}$ yaw in 10 seconds, -35° yaw in 10 seconds performed with decoupled control steering. Note momentum increase/decrease despite singular [A] matrix with decoupled control. Also, note the maneuver drastically exceeds 1H momentum.

88
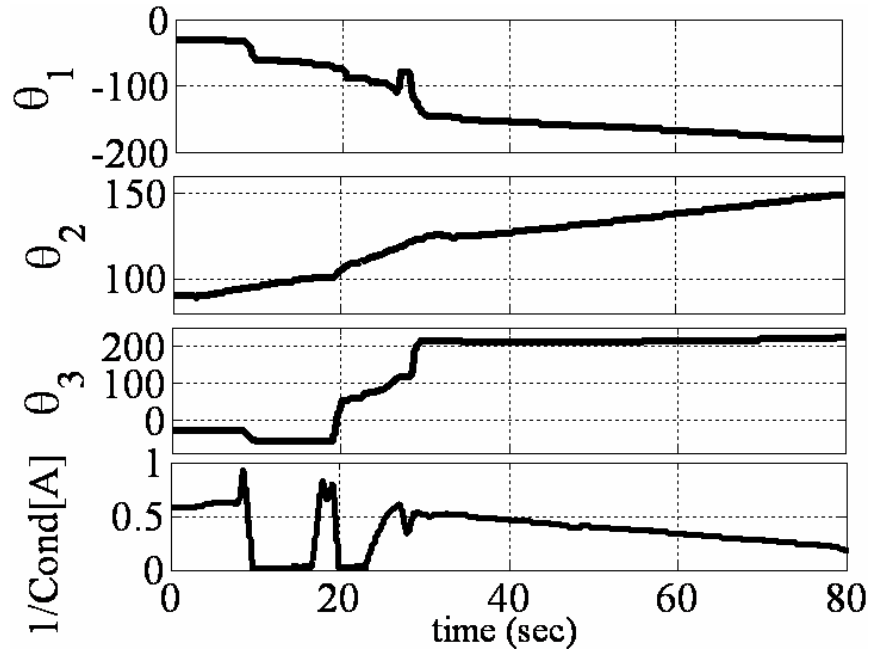
Figure 71 EXPERIMENT: Decoupled control gimbal angles.

Gimbal angles (top) and 1/cond[A] (bottom) versus time (seconds) for +35° yaw in 10 seconds, -35° yaw in 10 seconds performed with decoupled control steering. Note smooth gimbal action despite singular [A] matrix with decoupled control. Typical coupled control steering would have resulted in loss of spacecraft attitude control. Instead, with decoupled steering, you will notice a nice maneuver despite singular [A] matrix. Attitude control is not lost at any time.

5.   Singularity Penetration with Unit Delay

We see that singularity reduction is effective. While SR Inverse was effective at avoiding singularities, it could not follow the commanded momentum trajectory through the singularity. Singularity reduction permits momentum trajectory following, but is unique to the optimal singularity-free skew angle. Next, experiments were performed with typical *coupled* control and singularity penetration algorithm, SPUD. In the comparative slides, you'll immediately notice the experiment performed *without* SPUD was terminated early (after about 25 seconds) to prevent hardware damage due to loss of attitude control. This demonstrates that with a coupled system, spacecraft control would have been lost around 1H, not the nearly 3H achieved in the previous section. For the depicted experiment (Figure 72), a challenging yaw reversal was commanded just after penetrating the singularity causing the singularity to be immediately penetrated again. SPUD penetrated singularities well in both directions.
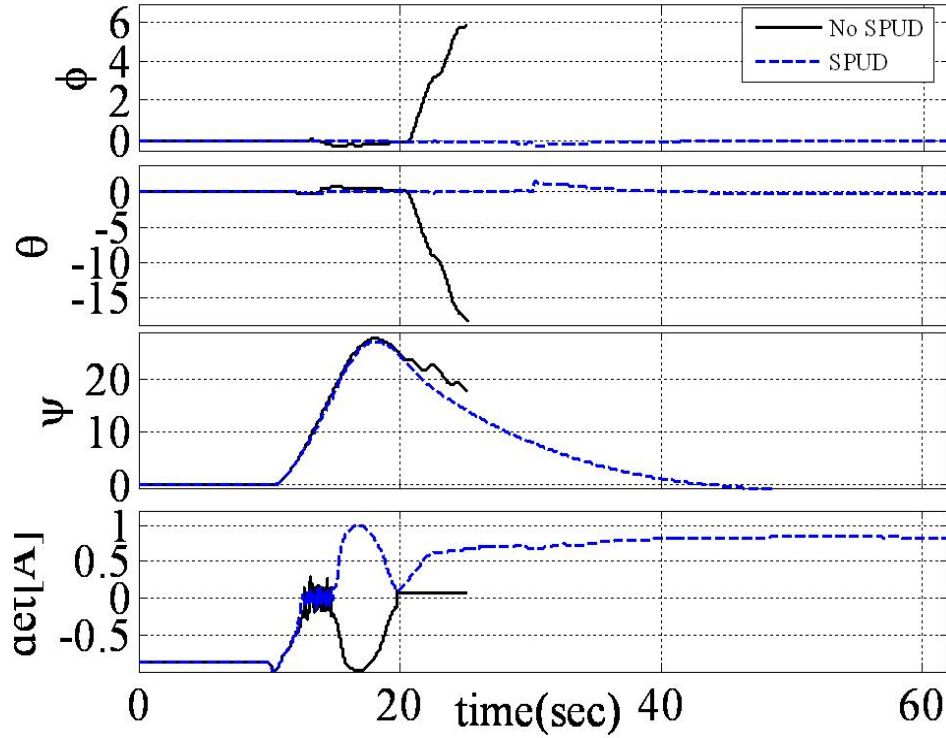
Figure 72 EXPERIMENT: Singularity penetration Euler angles.

Yaw Euler angle (top) and 1/cond[A] (bottom) versus time (seconds) for $+30^o$ yaw in 8 seconds immediately followed by -30° in 8 seconds performed with and without SPUD.
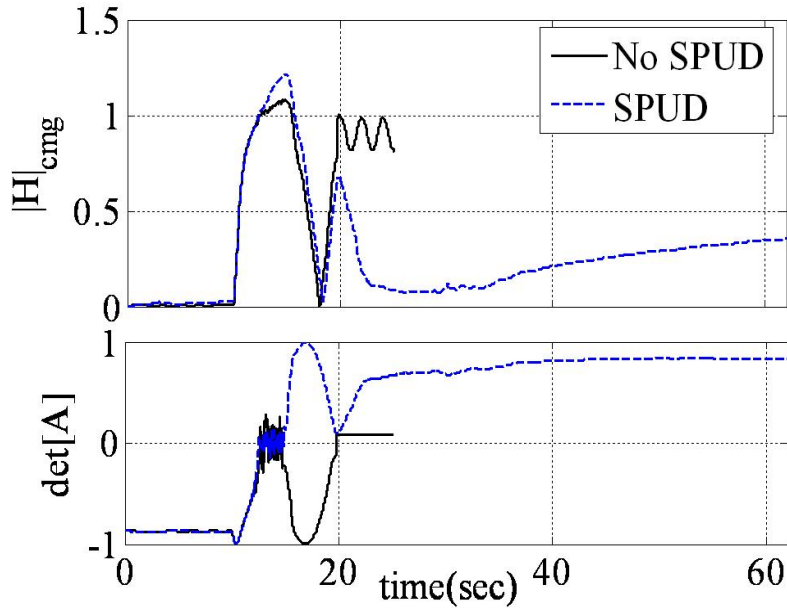
Figure 73 EXPERIMENT: Singularity penetration momentum.

Momentum Magnitude (top) and det[A] (bottom) versus time (seconds) for $+30^o$ yaw in 8 seconds, immediately followed by -30° in 8 seconds performed with and without SPUD. Note momentum increase/decrease despite singular [A] matrix with decoupled control. Also, note the maneuver drastically exceeds 1H momentum.
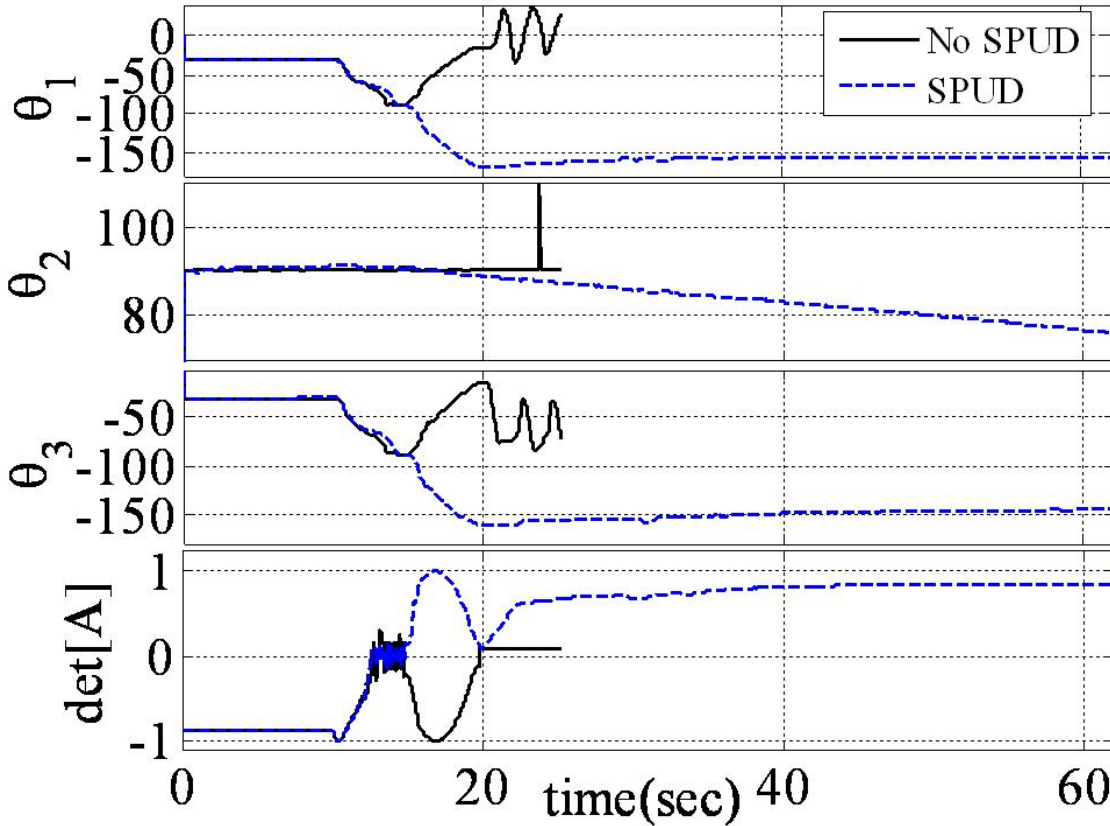
Figure 74 EXPERIMENT: Singularity penetration gimbal angles.

Gimbal angles (top) and det[A] (bottom) versus time (seconds) for +30o yaw in 8 seconds immediately followed by -30o in 8 seconds performed with and without SPUD. Note smooth gimbal action despite singular [A] matrix with SPUD.

These experiments demonstrate a much desired goal of CMG attitude control, extremely high torque without mathematical singularity thus without loss of attitude control. A new optimized geometry is shown to increase singularity-free torque capability an order of magnitude. The maximized singularity-free momentum is rotated to a desired by utilizing mixed skew angles. Using a proposed decoupled control strategy, further singularity reduction is achieved. Lastly, a singularity penetration algorithm is shown to allow momentum trajectories to cleanly pass through singular surfaces without loss of attitude control. These claims were introduced analytically and promising simulations are provided. Finally experimental verification is performed demonstrating dramatic yaw maneuvers that pass through singular surfaces that would render loss of attitude control using typical coupled control techniques.

91

B.   TARGET TRACKING EXPERIMENTS

1.   Classical Control Experiment

Actual spacecraft inertia (6) components are unknown. Older estimated inertia values (prior to payload installation) are used for classical feedforward control design and initializing adaptive controllers. The identical acquisitions and target tracking maneuver simulated above is commanded on the Naval Postgraduate School's three-axis satellite simulator 2 (TASS2). The methods in the literature (Slotine/Fossen) compare adaptive feedforward and feedback control favorably to PD feedback only. This study will compare to the more realistic classical feedforward with feedback (established as a baseline in Figure 75). With this baseline, the proposed adaptive feedforward controllers are compared to this baseline.
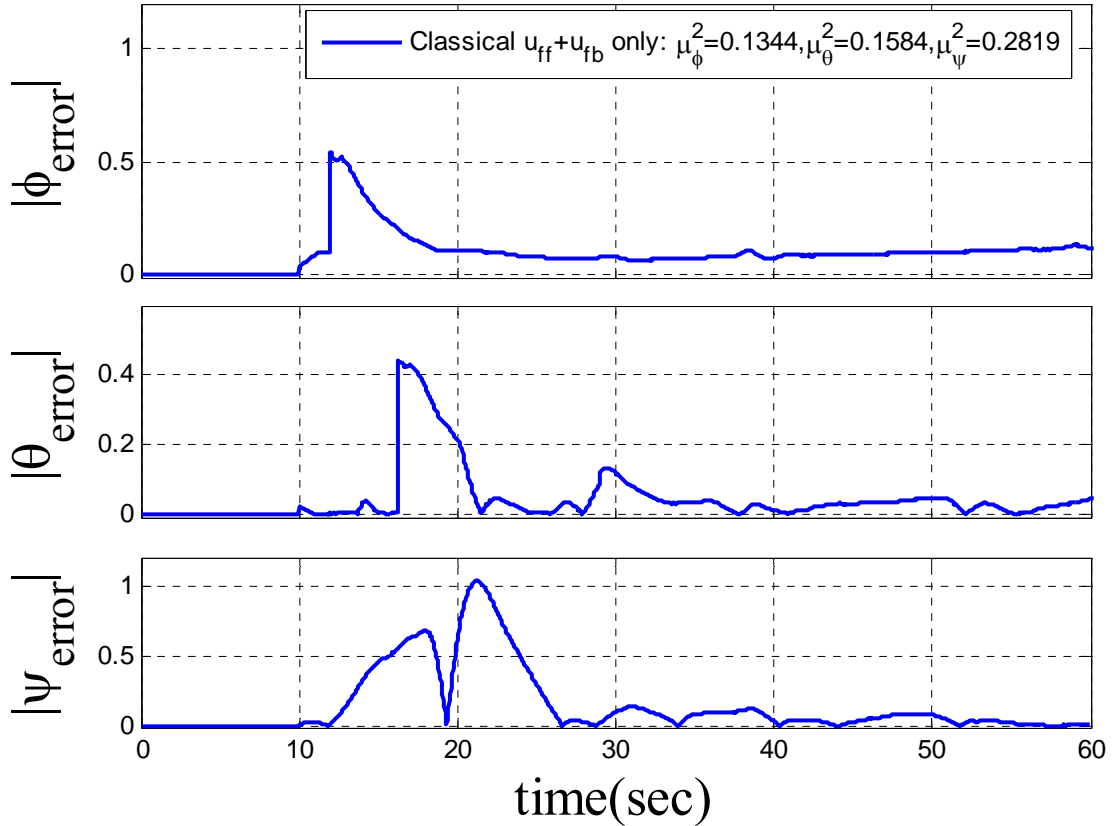
Figure 75 EXPERIMENT: Classical control experiment.
Large-angle acquisition maneuver followed by target tracking trajectory: Tracking errors (roll ϕ, pitch θ, yaw ψ in degrees) BASELINE: Classical feedback + PD feedback control (K_p=100, K_d=100).

2. Adaptive Control Experiments
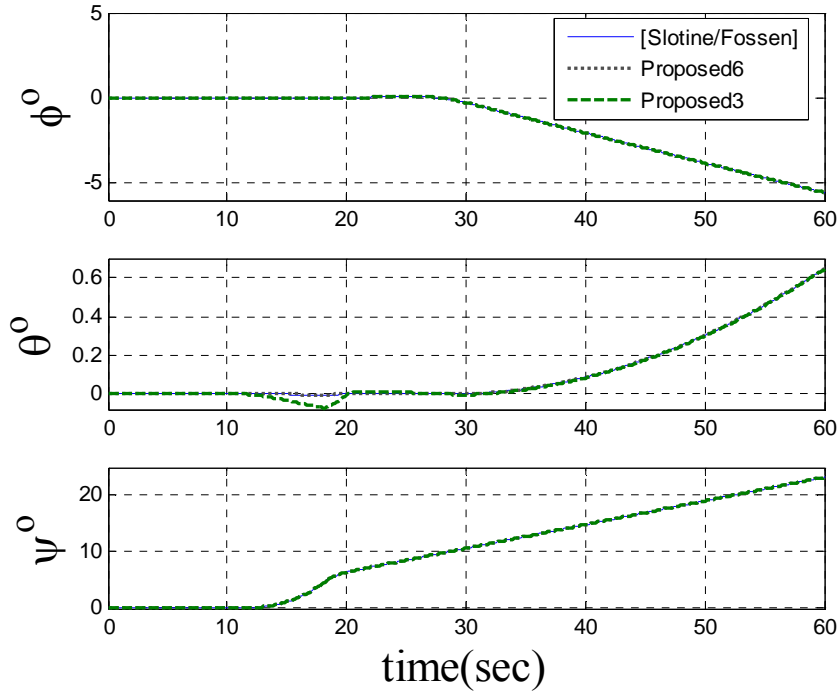
Figure 76 EXPERIMENT: Euler angle comparison.

Adaptive Control techniques compared for ATP trajectory: $\lambda=\lambda_{fb}=1/2$, $\Gamma=1$, $K_d=200$, $\lambda_{ff}=1$, $K_p=100$
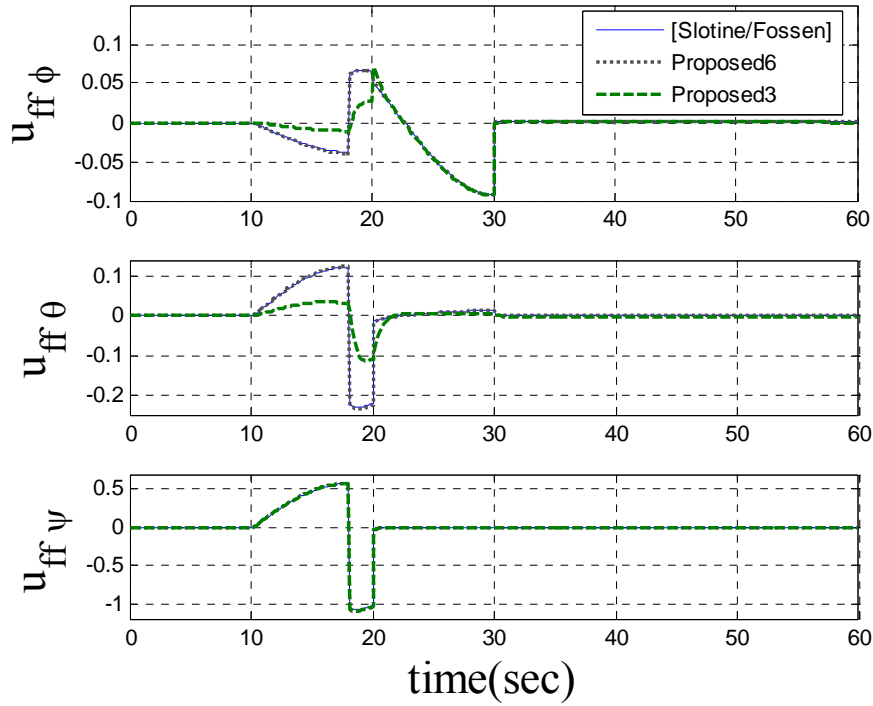
Figure 77 EXPERIMENT: Feedforward control comparison.

Adaptive Control techniques compared for ATP trajectory: $\lambda=\lambda_{fb}=1/2$, $\Gamma=1$, $K_d=200$, $\lambda_{ff}=1$, $K_p=100$
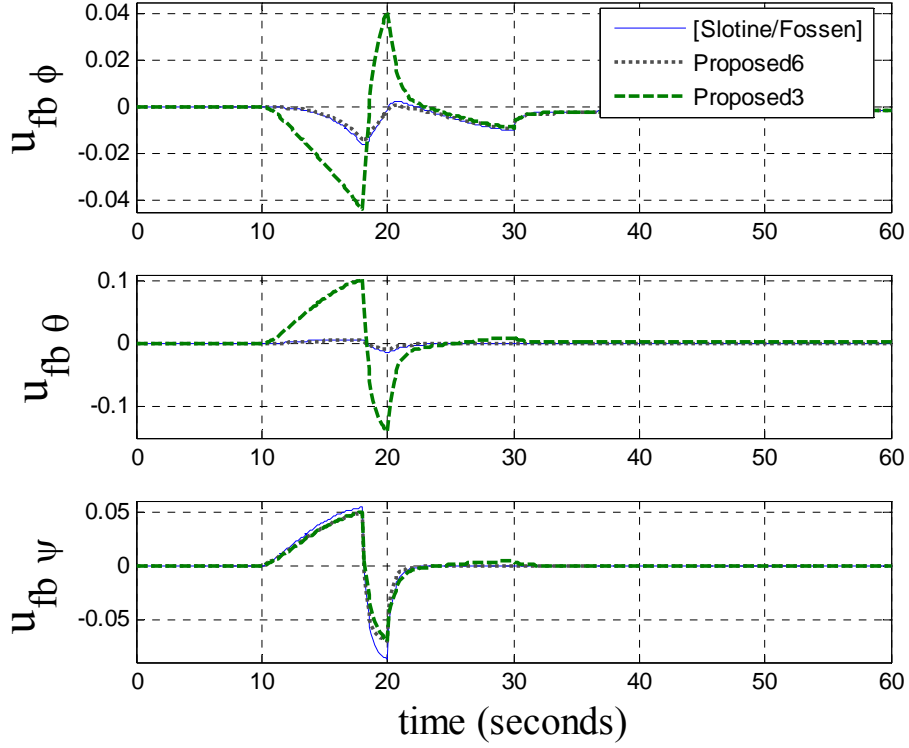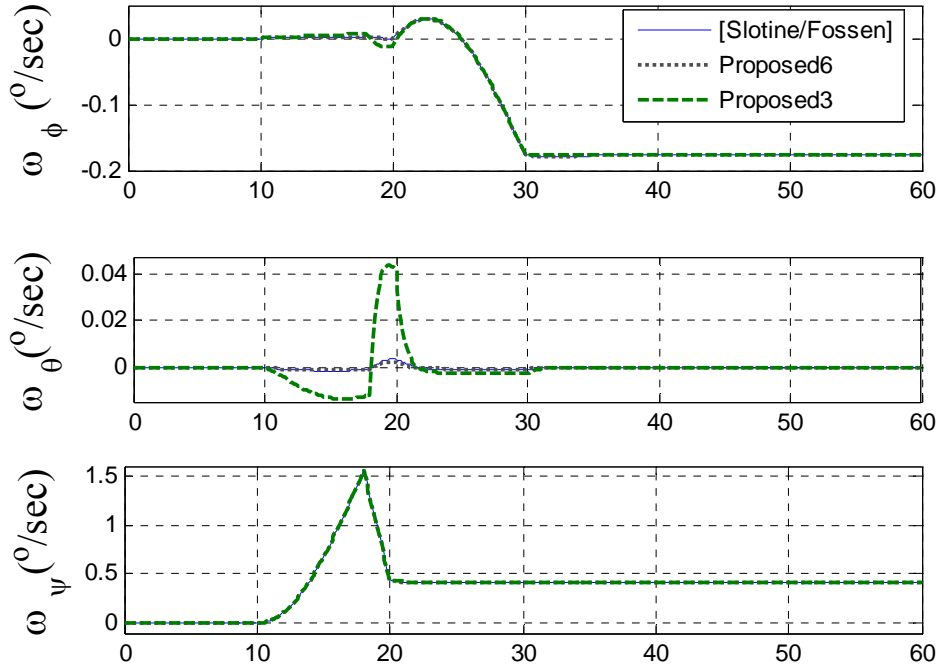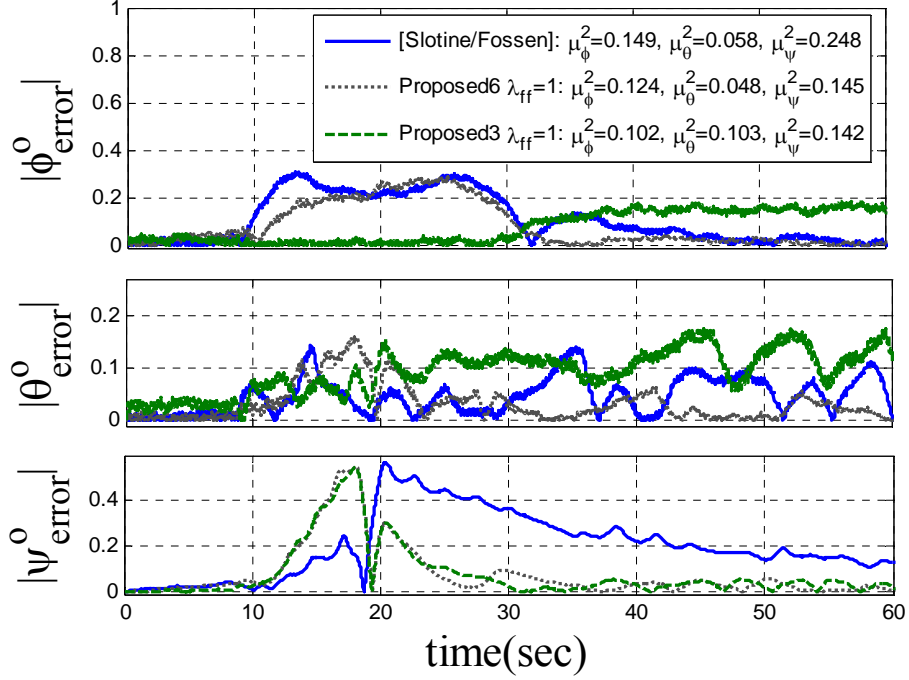
Figure 78 EXPERIMENT: Feedback control comparison.

Adaptive Control techniques compared for ATP trajectory: $\lambda=\lambda_{fb}=1/2$, $\Gamma=1$, $K_d=200$, $\lambda_{ff}=1$, $K_p=100$

Figure 79 EXPERIMENT: Angular rate comparison.

Adaptive Control techniques compared for ATP trajectory: $\lambda=\lambda_{fb}=1/2$, $\Gamma=1$, $K_d=200$, $\lambda_{ff}=1$, $K_p=100$

Figure 80 EXPERIMENT: Adaptive control comparison.

$\lambda=\lambda_{fb}=1/2$, $\Gamma=1$, $K_d=200$, $\lambda_{ff}=1$, $K_p=100$ For large-angle acquisition maneuver followed by target tracking trajectory: Tracking errors (roll ϕ, pitch θ, yaw ψ in degrees) comparison: [Slotine/Fossen] adaptive feedforward & PD feedback control, Proposed6 adaptive feedforward ($\lambda_{ff}=1$) & PD feedback control, Proposed3 adaptive feedforward ($\lambda_{ff}=1$) & PD feedback control.
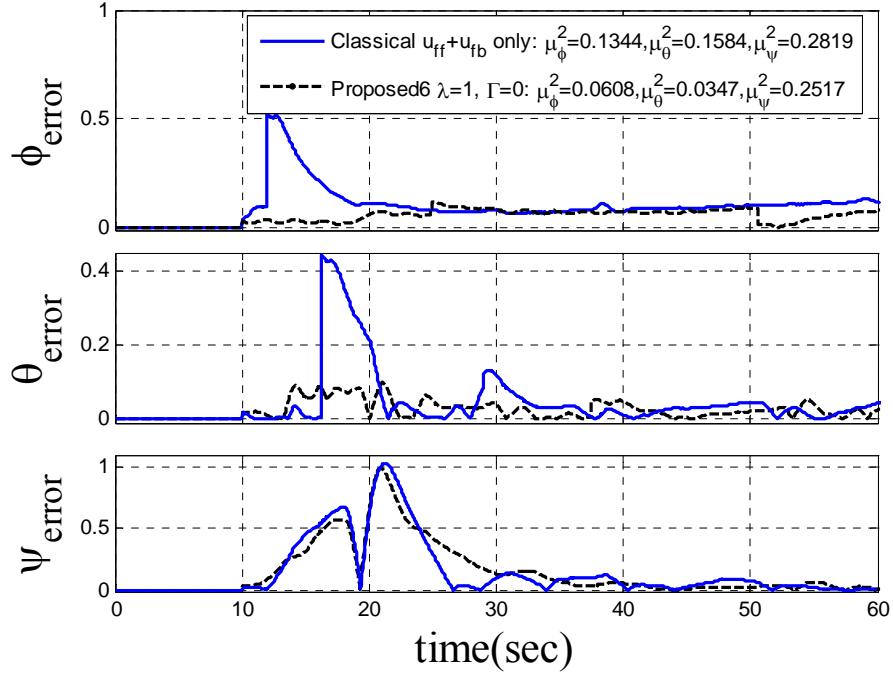
Figure 81 EXPERIMENT: No estimation adaptive control comparison.

$\lambda=\lambda_{fb}=1/2$, $\Gamma=1$, $K_d=200$, $\lambda_{ff}=1$, $K_p=100$
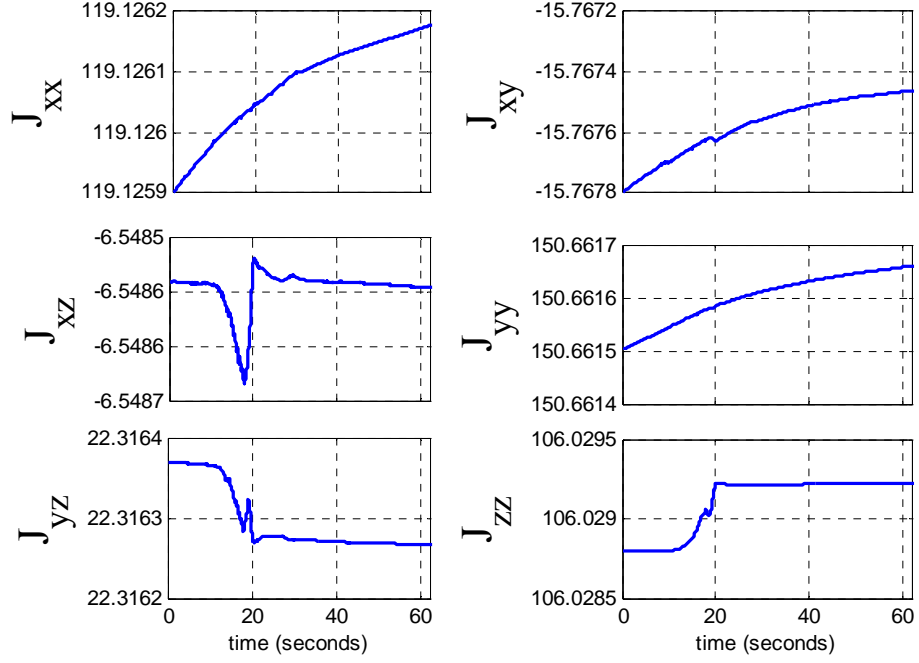
Figure 82 EXPERIMENT: Inertia estimation.
Inertia estimates using Proposed6 adaptive feedforward $u_{ff} + u_{fb}$: $\Gamma=1$, $\lambda_{ff}=1$,Kp=100,Kd=200.
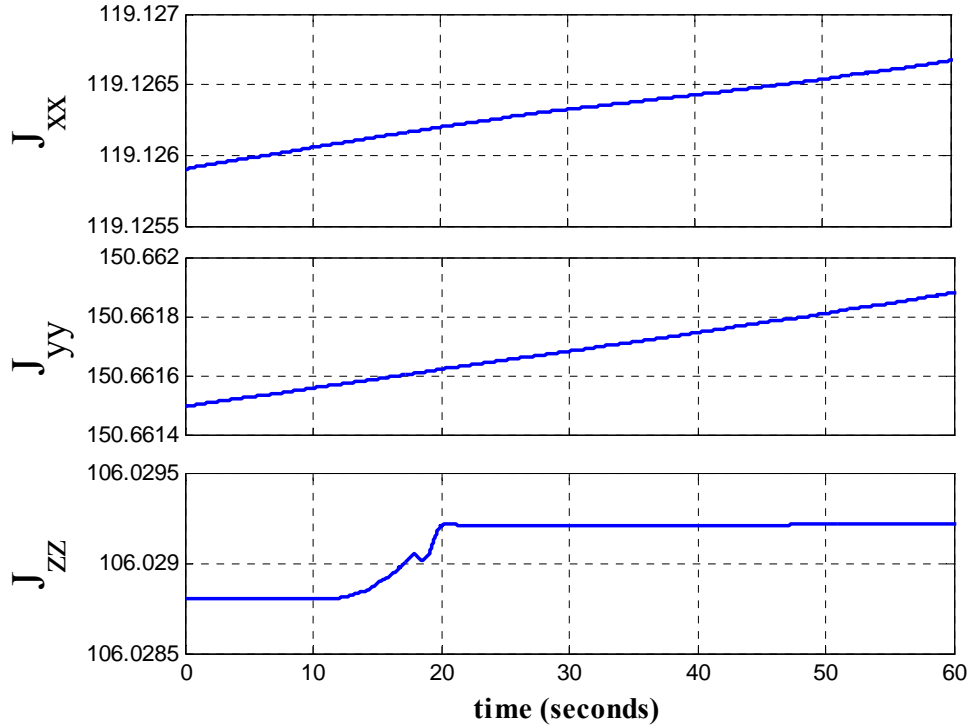
Figure 83 EXPERIMENT: Inertia estimation.
Inertia estimates using *Proposed3* adaptive feedforward $u_{ff} + u_{fb}$: $\Gamma=1$, $\lambda_{ff}=1$,Kp=100,Kd=200.

IV. DISCUSSION OF RESULTS

A. PERFORMANCE

1. Target Acquisition Maneuvers with CMGs

The research in this thesis clearly indicates that substantial singularity-free performance increase can be achieved using the 3/4 CMG skewed array utilizing a skew angle of 90°. This skew angle is designated the optimal singularity free skew angle. Singularity-free momentum is increased over 567% (from 0.15H to 1H normalized magnitude). Furthermore it is shown that the orientation of maximum momentum may be rotated using mixed skew angles to orient the maximum capability along a preferred slew direction. The remaining singular surfaces may be reduced by decoupling the control steering law. 1900% performance increase was shown in simulation and 1500% performance increase was experimentally verified using decoupled control steering. While decoupled steering is uniquely contributable to the proposed optimal singularity-free skew angle, a more generic singularity penetration algorithm was also presented. The singularity penetration algorithm was tested in simulation and verified experimentally with a difficult commanded trajectory that commands a reversal of direction just after penetrating a singular surface. The commanded return immediately penetrates the same singular surface again cleanly generating momentum without loss of attitude control.

2. Target Tracking with Adaptive Control

Adaptive control for spacecraft fine tracking results may be succinctly examined by narrowly focusing on the performance of simulations to reveal the expected dynamic behavior of the algorithms and comparing simulations to experimental verification. Simulations were performed for a rapid slew for target acquisitions, and quick settling followed by fine tracking of an uncooperative target. Simulations do not include noise or other imperfections except purposely under-modeled spacecraft inertia (10% and also 30%). Performing simulations for 10% and also for 30% allow subjective conclusions. Is a particular algorithm superior or inferior if initial inertia estimate is more accurate? Consider classical feedforward & PD feedback command as the baseline, since it is most

97

typically used for spacecraft missions. All simulations reveal that Slotine's method as modified by Fossen achieve substantial performance increase. Additionally, the method exhibits higher percent performance increase when the inertia is less accurately known (indicated by increased percent performance increase for 30% inertia error compared to 10% inertia error.

The commanded acquisitions, tracking, and fine pointing (ATP) trajectory was maintained identical in simulation and experimentation. Recall the roll axis commands represents sinusoidal target evasion with yaw axis representing the primary acquisition slew axis and target run.

Particularly notice no performance difference is seen comparing Slotine/Fossen's method neglecting inertia estimation effects (estimation dynamics negated by setting $\Gamma=0$). Technically, a non-zero difference does exist on the order of 10^{-9} degrees per tables 3&4. As an addendum to the proposed adaptive control algorithms, it is noted that estimation dynamics may be eliminated completely if further computational simplification is required. Reduced tracking error performance may still be achieved simply by generating the reference trajectory and adapting the feedforward command alone using this reference trajectory maintaining PD feedback.

60 Second ATP simulation 10% inertia error: Percent PERFORMANCE INCREASE			
Control Method (*baseline)	-% $\Delta\phi$	-% $\Delta\theta$	-% $\Delta\psi$
[Classical u_{ff} + $K_p=K_d=200$] *	0.00%	0.00%	0.00%
[Slotine/Fossen] $\lambda=1/2$, $\Gamma=1$	15.24%	96.12%	90.96%
[Slotine/Fossen] $\lambda=1/2$, $\Gamma=0$	15.24%	96.12%	90.96%
Derived6: $\lambda=1/2$, $\Gamma=1$	15.24%	96.12%	90.96%
Proposed6: $\lambda_{ff}=1$, $\Gamma=1$, $\lambda_{fb}=1/2$	17.95%	95.81%	91.73%
Proposed6: $\lambda_{ff}=1$, $\Gamma=0$, $\lambda_{fb}=1/2$	17.95%	95.81%	91.73%
Proposed3: $\lambda_{ff}=1$, $\Gamma=1$, $\lambda_{fb}=1/2$	-0.89%	41.73%	90.29%
Proposed3: $\lambda_{ff}=1$, $\Gamma=0$, $\lambda_{fb}=1/2$	-0.89%	41.73%	90.29%

Table 6 SIMULATION: 10% Inertia error percent performance increase.

60 Second ATP simulation 30% inertia error: Percent PERFORMANCE INCREASE			
Control Method (*baseline)	-% Δ φ	-% Δθ	-% Δψ
[Classical u_{ff} + K_p=K_d=200] *	0.00%	0.00%	0.00%
[Slotine/Fossen] λ=1/2, Γ=1	39.04%	96.19%	96.81%
[Slotine/Fossen] λ=1/2, Γ=0	39.04%	96.19%	96.81%
Derived6: λ=1/2, Γ=1	39.04%	96.19%	96.81%
Proposed6: $λ_{ff}$=1, Γ=1, $λ_{fb}$=1/2	40.99%	95.89%	97.08%
Proposed6: $λ_{ff}$=1, Γ=0, $λ_{fb}$=1/2	40.99%	95.89%	97.08%
Proposed3: $λ_{ff}$=1, Γ=1, $λ_{fb}$=1/2	27.44%	42.77%	96.57%
Proposed3: $λ_{ff}$=1, Γ=0, $λ_{fb}$=1/2	27.44%	42.77%	96.57%

Table 7 SIMULATION: 30% Inertia error percent performance increase.

60 second ATP Experiment	RMS $φ^o$ Error	RMS $θ^o$ Error	RMS $ψ^o$ Error
Classical u_{ff} + K_p=K_d=200	0.13440	0.15840	0.28190
[Slotine/Fossen] λ=1/2, Γ=1,K_d=200	0.14900	0.05800	0.24800
Proposed6: $λ_{ff}$=1, Γ=1,K_d=200, $λ_{fb}$=1/2	0.12400	0.00480	0.14500
Proposed3: $λ_{ff}$=1, Γ=1,K_d=200, $λ_{fb}$=1/2	0.10200	0.10300	0.14200
Proposed6: $λ_{ff}$=1, Γ=0,K_d=200, $λ_{fb}$=1/2	0.06080	0.03470	0.25170

Table 8 EXPERIMENT: RMS errors raw data

60 Second ATP experiment: Percent PERFORMANCE INCREASE			
Control Method (*baseline)	-% Δ φ	-% Δθ	-% Δψ
[Classical u_{ff} + K_p=K_d=200] *	0.0%	0.0%	0.0%
[Slotine/Fossen] λ=1/2, Γ=1,K_d=200	-10.9%	74.7%	25.2%
Proposed6: $λ_{ff}$=1, Γ=1,K_d=200, $λ_{fb}$=1/2	7.7%	114.3%	101.9%
Proposed3: $λ_{ff}$=1, Γ=1,K_d=200, $λ_{fb}$=1/2	24.1%	41.2%	104.1%
Proposed6: $λ_{ff}$=1, Γ=0,K_d=200, $λ_{fb}$=1/2	54.8%	92.0%	22.5%

Table 9 EXPERIMENT: percent performance increase in RMS errors.

a.   Alternative for Future Comparison: Projection Algorithm

Elimination of estimation is desirable due to the checkered history of adaptive control failures due to parameter drift. Model reference adaptive control (MRAC) methods were shown by Rohrs to be unstable for unmodeled flexible dynamics (e.g. a pair of high frequency unmodeled zeros). While MRAC adapted in gain, it did not

in phase permitting instability. Very recently, Cao and Havakimyan [55],[56] formulated modifications to the MRAC adaptive control to solve the issue. It is shown that for convex functions of estimation dynamics, the estimation rate may be modified to include a projection function that prevents parameter drift beyond a defined boundary. In this thesis estimate drift was addressed by striving to eliminate the estimation resulting in a robust feedforward control approach with PD feedback control. In instances where estimation must be maintained, this projection algorithm seems promising, but insufficient time was available to implement it here. The projection algorithm guarantees that the estimates will remain in a set: $\Omega = \{\Theta; f(\Theta) \leq 1\}$ where the convex function is

$$\frac{\Theta^T\Theta - \Theta_{max}^2}{\varepsilon_\Theta \Theta_{max}^2} = f(\Theta) \leq c \leq 1 \qquad (67)$$
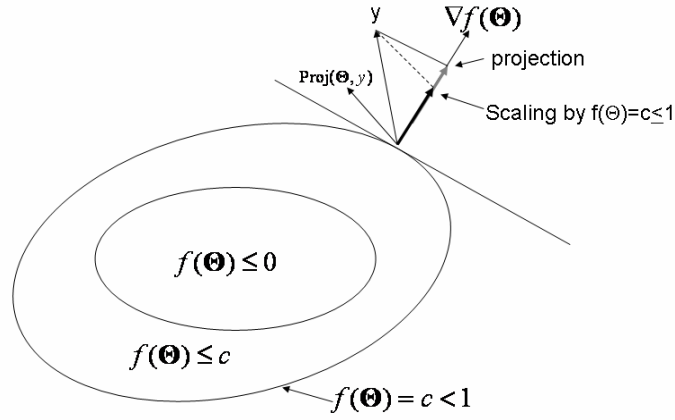
Figure 84 Illustration of the projection operator.

The estimation rate dynamics law then becomes:

$$\dot{\hat{\Theta}} = \text{Proj}(y, \Theta) \qquad (68)$$

$$\text{Proj}(\Theta, \mathbf{q}) \, \square \, \begin{cases} y \\ y \\ \frac{\nabla f}{\|\nabla f\|} \left\langle \frac{\nabla f^T}{\|\nabla f\|}, y \right\rangle f(\Theta) \end{cases} \qquad (69)$$

For a convex compact set with a smooth boundary condition given by $\Omega \square \left\{ \Theta \in \square^{n} \mid f(\Theta) \leq c \right\}, \ 0 \leq c \leq 1$. This projection algorithm allows estimates to wander until they hit the boundary where they stay.

B. IMPLEMENTATION ISSUES

1. Target Acquisition Maneuvers with CMGs

While the singularity penetration algorithm has been presented and demonstrated to be effective, the engineer is left with the task of deciding when to activate the singularity penetration algorithm. In this research, engagement was based on first simulating the planned trajectory and noting the value of det[**A**] when singularity-like behavior is observed. The singularity penetration is then set to engage prior to this critical value of det[**A**]. Since the value varies with planned maneuver, a more generic criteria is desired. Consider using two conditions: when det[**A**] reaches a low value (much looser than implemented here), and also when commanded gimbal rates reach saturation. As a CMG approaches an angle such that it can no longer generate momentum in a commanded direction, commanded gimbal rates increase. When saturation is reached, the det[**A**] value continues to decrease, but for all essentially purposes the array is singular since the gimbal rates have saturated.

2. Target Tracking with Adaptive Control

It has been discussed that real world issues (e.g., noise) complicate actual application of many promising advanced algorithms. Notice in all of the regression models used in the adaptive algorithms, angular rate measurements are differentiated. There is no such device that measures inertia angular acceleration, so the noisy rate gyro measurements must be computationally differentiated, an inherently noise-magnifying procedure. This is a fundamental weakness of the regression/estimation approach to adaptive control. Engineers typically use classical feedforward and feedback controls. This research suggests adapting the feedforward trajectory alone can improve system performance while reducing the amplification of noise in real world sensors and systems.

IV.

THIS PAGE INTENTIONALLY LEFT BLANK

V. CONCLUSIONS AND FUTURE WORKS

Target acquisitions, tracking and fine pointing (ATP) is a challenging mission for military spacecraft. Large-momentum slew maneuvers of spacecraft with short settling times while maintaining fine pointing requirements present considerable challenges to conventional spacecraft designs. The large slew acquisition maneuver often dictates utilizing control moment gyroscopes for momentum exchange (torque), but singularities complicate actual implementation. In this dissertation an alternative, actuator configuration is proposed yielding significant increase in singularity-free momentum generation. This alternative configuration is demonstrated to be the optimum CMG skew angle for singularity free momentum generation. This allows spacecraft to slew much more rapidly and settle faster with larger control torques available. Secondly, it is shown that the direction of maximum singularity-free momentum may be rotated to a desired direction using mixed skew angles. Even in the optimum configuration, some singularities still exist and are addressed in the third new contribution presented here. Thirdly, these remaining singularities may be reduced with a proposed decoupled control steering technique that is unique to the optimum singularity-free skew angle. Fourthly, a new singularity penetration algorithm is presented that has the potential to grant maximum array torque.

Following the rapid slew target acquisition maneuver, non-cooperative targets must be tracked with high pointing accuracy despite disturbances and un-modeled dynamics including poorly estimated inertia. During the demanding military mission, poorly modeled inertia limits tracking performance. One indirect adaptive control method has been suggested in the literature, but was derived in the inertial frame resulting in unwieldy computations. Additionally, the method was only compared to feedback control alone. An addendum suggested derivation in the body frame, but did not derive the method for spacecraft attitude control. The fifth contribution presented here derives the method for spacecraft attitude control and critically compares the results to typical feedforward + feedback control.

The sixth new contribution presented here introduces a new simpler, nonlinear, indirect adaptive feedforward control technique to estimate the actual inertia and reduce tracking errors. It is shown to grant superior performance to typical feedforward + feedback control as well as the adaptive control methods in the literature. Since nonlinear adaptive control methods can often become cumbersome, two additional new simplified techniques (reduced order) are shown to grant similar reduction in tracking errors presented as sixth and seventh suggested contributions. The ninth and final new development suggested here is an alternative reference trajectory robust fixed gain feedforward technique that does not require estimation, but retains target tracking performance increase. Stability analysis of this final technique remains a "future work." Taken together, military spacecraft have several new options available to address target acquisition, tracking and fine pointing.

Finally, it can not be understated that experimental verification is included for all new methods suggested here. Actual experimental implementation can often confound the most elegant mathematical formulations. In theory, it is shown that 15-91% performance increase is possible with -10% inertia error, and 39-97% performance increase is possible with -30% inertia error (for the case of the estimated inertia of the three-axis spacecraft simulator at the Naval Postgraduate School). In actual experiments, 7-114% performance increase was achieved noting the actual error in inertia estimates is unknown. Regarding large momentum acquisitions maneuvers, experimental verification is crucial since a singularity may result is complete loss of attitude control. Experimental results were presented verifying near-maximum momentum generation without loss of attitude control.

Future works also include implementation of these techniques on a flexible multi-body spacecraft. This research assumed a rigid spacecraft, while the current trend in spacecraft construction results in lighter, more flexible structures. As a matter of fact, current spacecraft have become so flexible, that their lowest natural frequency lies within the bandwidth of typical attitude controllers. This is referred to as controls-structures interaction, where simply commanding any maneuver is guaranteed to excite resonant vibration in the spacecraft. This is extremely challenging, and the advanced control techniques proposed here should be modified to account for structural interaction.

LIST OF REFERENCES

[1]   NASA Jet Propulsion Laboratory, 1 March 2007, "Mission and Spacecraft Library, JPL. Quicklook: Hubble Space Telescope": http://msl.jpl.nasa.gov/QuickLooks/hstQL.html

[2]   Public Broadcasting Service, 1 March 2007, "All About Hubble", http://www.pbs.org/deepspace/hubble/diagram.html

[3]   R.R. Burt, R.W. Loffi, "Failure analysis of International Space Station Control Moment Gyro," *Proceedings of the 10th European Space Mechanisms and Tribology Symposium*, ESA Publications Division, 13-15, ISBN 92-9092-834-4, 2003.

[4]   C.R. Sims, "International Space Station U.S. GN&C Momentum Manager Controller Design for Shuttle Thermal Protection System Repair," *Proceedings of AIAA GNC Conference*, 15-18 Aug 2005, AIAA 2005-5854.

[5]   Earth Observation Resources, "Skylab Space Station", 1 March 2007, : http://directory.eoportal.org/pres_SkylabSpaceStation.html

[6]   J. Paradiso, "A Search-based approach to steering single-gimbaled CMGs," CSDL-R-2261, 17,26, 1991.

[7]   D.J. Liska and Jacot Dean, "Control moment gyros," AIAA Second Annual Meeting Paper Preprint Number 65-405, July 1965.

[8]   B.D. Elrod, G.M. Anderson, "Equilibrium properties of the skylab CMG rotation law-Case 620," NASA-CR-126140 (Bellcomm TM-72-1022-2), 79, 1972.

[9]   H.F. Kennel, "Steering law for parallel mounted double-gimbaled control moment gyros," NASA-TM-X-64930, 34, 1975.

[10]   B.K. Colburn and L.R. White, "Computational considerations for a spacecraft attitude control system employing control moment gyro," Journal of Spacecraft, Vol. 14, No. 1, 40-42, 1977.

[11]   T. Yoshikawa, "A Steering law for three double gimbal control moment gyro system," NASA-TM-X-64926, 1975.

[12]   H.F. Kennel, "Steering law for parallel mounted double-gimbaled control moment gyros," NASA-TM-X-82390, 22, 1981.

[13]   Magulies and J.N. Aubrun, "Geometric theory of single-gimbal control moment gyro system," Journal of Astronautical Sciences, Vol. 26, No.2, 159-191, 1978.

[14]   E.N. Tokar, "Problems of gyroscopic stabilizer control," Cosmic Research, pp. 141-147, 1978 (original: Kosmicheskie Issledovaniya Vol. 16, No. 2, 179-187, 1978).

[15]   Haruhisa, Kirokawa, "A Geometric study of single gimbal control moment gyroscopes," Technical Report of Mechanical Engineering Lab No. 175, June 7, 1997.

[16]   D.E. Cornick, "Singularity avoidance control laws for single gimbal control moment gyros, Proceedings of AIAA Guidance and Control Conference 79-1968, 20-33, 1979 (Martin Marietta Corp.).

[17]   Bong Wie, Space Vehicle Dynamics and Control, 439, AIAA, 1998.

[18]   R.D. Hefner and C.H. McKenzie, "A Technique for maximizing the torque capability of control moment gyro systems," Astrodynamics Vol. 54 (Proceedings of AAS/AIAA Astrodynamics Conference Vol. 2), 905-920, 1983.

[19]   Kurokawa, N. Yajima, and S. Usui, "A CMG attitude control system for balloon use," Proceedings of 14th International Symposium on Space Technology and Science (ISTS), 1211-1216, 1984.

[20]   Kurokawa, N. Yajima, and S. Usui, "A New steering law of a single gimbal CMG system of pyramid configuration," Proceedings of IFAC Automatic Control in Space, 251-257, 1985.

[21]   S.R. Bauer, "Difficulties encountered in steering single gimbal CMGs," Space Guidance and Navigation Memo No. 10E-87-09, The Charles Stark Draper Laboratory, Inc.

[22]   NASA MSFC, "A Comparison of CMG steering laws for high energy astronomy observatories (HEAOS)," NASA TM X-64727, 127, 1972.

[23]   Bong Wie, "Singularity Robust Steering Logic for Redundant Single-Gimbal ControlMoment Gyros," Journal of Guidance, Control, and Dynaimcs, Vol. 24, No. 5, September-October 2001, 865-872.

[24]   N.S. Bedrossian, "Steering law design for redundant single gimbal control moment gyro systems," NASA-CR-172008 (M.S. Thesis of Massachusetts Institute of Technology, CSDL-T-965), 138, 1987.

[25]   N.S. Bedrossian, J. Paradiso, E.V. Bergmann, D. Rowell, "Steering law design for redundant single-gimbal control moment gyroscope," AIAA Journal of Guidance, Control, and Dynamics, Vol. 13, No. 6, 1083-1089, 1990.

[26]   G. Magulies and J.N. Aubrun, "Geometric theory of single-gimbal control moment gyro system," Journal of Astronautical Sciences, Vol. 26, No.2, 159-191, 1978.

[27]   Paradiso, "Global steering of single gimbaled control moment gyroscopes using a directed search," AIAA Journal of Guidance, Control, and Dynamics, Vol. 15, No. 5, 1236-1244, 1992

[28]   Paradiso, "A Search-based approach to steering single-gimbaled CMGs," CSDL-R-2261, 183, 1991.

[29]   S.R. Vadali, S. Krishnan, "Suboptimal command generation for control moment gyroscopes and feedback control of spacecraft," Proceedings of AIAA Guidance, Navigation, and Control Conference, 637-646, Aug 1994].

[30]   M. Romano, B.N. Agrawal, "Attitude Dynamics/Control of Dual-Body Spacecraft with Variable-Speed Control Moment Gyros," AIAA Journal of Guidance, Dynamics, and Control, vol.27, No. 4, 513-525, July-Aug 2004.

[31]   S.M. Seltzer, "CMG-induced LST dynamics," NASA-TM-X-64833, 80, 1974.

[32]   S.M. Seltzer, "Large space telescope oscillation induced by CMG friction," Journal of Spacecraft, Vol. 12, No. 2, 96-105, 1975.

[33]   S.M. Seltzer, "Limit cycle analysis of large space telescope with CMG nonlinearity," NASA-TM-X-64939, 20, 1975.

[34]   S.P. Linden, "Precision CMG control for high-accuracy pointing," Proceedings of AIAA Guidance and Control Conference, AIAA No. 73-871,7, 1973.

[35]   S.C. Rybak, "Achieving ultrahigh accuracy with a body pointing CMG/RW control system," Proceedings of AIAA Guidance and Control Conference AIAA No. 73-871, 7, 1973.

[36]   S.R. Vadali, H.S. Oh, and S.R. Walker, "Preferred gimbal angles for single gimbal control moment gyros," Journal of Guidance, Vol, 13, No. 6, 1090-1095, Nov-Dec 1990.

[37]   T.A. Sands, J.J. Kim, B.N. Agrawal, "2H Singularity-Free Momentum Generation with Non-Redundant Single Gimbaled Control Moment Gyroscopes," Proceedings of 45th IEEE Conference on Decision and Control (CDC), San Diego, CA, Dec. 2006, IEEE Paper # CDC06_1236_MS.

[38]   J. Ahmed, "Asymptotic Tracking of Spacecraft Attitude Motion with Inertia Identification," AIAA Journal of Guidance, Dynamics and Control, Sep-Oct 1998.

[39]   Cristi, Burl, Russo, "Adaptive Quaternion Feedback Regulation for Eigenaxis Rotation," *AIAA Journal of Guidance, Dynamics and Control*, Nov-Dec 1994.

[40]   A. Sanya, "Globally Convergent Adaptive Tracking of Spacecraft Angular Velocity with Inertia Identification," *Proceedings of IEEE Conference of Decision and Control*, 2003.

[41]   E.H. Anderson, "Adaptive Feedforward Control for Actively Isolated Spacecraft Platforms," *AIAA Structures, Structural Dynamics, and Materials Conference and Exhibit,* Kissimmee, Apr 7-10, 1997: AIAA-1997-1200.

[42]   G. Niemeyer and J.J.E. Slotine, "Performance in adaptive manipulator control," *Proceedings of 27th IEEE Conference on Decision and Control*, December, 1988.

[43]   J.J.E Slotine and M.D. Benedetto, "Hamiltonian Adaptive Control of Spacecraft," *IEEE Transactions on Automatic Control*, Vol. 35, 848-852, July 1990.

[44]   J.J.E. Slotine W. Li, *Applied Nonlinear Control*, Prentice-Hall, Upper Saddle River, NJ, 1991, 422-433.

[45]   H. Yoon and P. Tsiotras, "Spacecraft Adaptive Attitude and Power Tracking with Variable Speed Control Moment Gyroscopes," *Journal of Guidance, Control, and Dynamics*, Vol. 25, No.6, Nov-Dec 2002.

[46]   T. Fossen, "Comments on 'Hamiltonian Adaptive Control of Spacecraft,'" *IEEE Transactions on Automatic Control*, Vol. 38., No. 4, April 1993.

[47]   M. Cassutt, *Who's Who in Space*, Macmillion, 1993, 191-2.

[48]   North American X-15, 1 March 2001, http://xplanes.free.fr/x15/A.html

[49]   C.D. Perkins, AIAA 6th Annual Meeting and Technical Display, California, Oct 20-24, 1969, AIAA-1969-1137

[50]   M. Romano, B.N. Agrawal, "Acquisition, tracking, and pointing control of the bifocal relay mirror spacecraft," Acta Astronautica, Vol. 53., No.4, 2003, 509-519.

[51]   W. Kulick, "Development of a Control Moment Gyroscope Controlled, Three-Axis Satellite Simulator with Active Balancing for the Bifocal Relay Mirror Initiative," *Master's Degree Thesis,* Naval Postgraduate School, Monterey, California, December, 2004.

[52]   Experiments (generalized singularity-robust inverse *only* Figure 61-Figure 67) performed by NRC Postdocs Dr. Kim, Jong-Woo, and Dr. Kim, Jay June. The ineffectiveness of the SR-inverse was a motivating factor for my developments presented here, so their experiments are presented for comparison.

[53]   J.J. Kim, B.N. Agrawal, "Acquisition, Tracking, and Pointing of Bifocal Relay Mirror Spacecraft," Beacm Control Conference, 2006, March 20-24, Monterey, CA 2006.

[54]   C. Rohrs, L. Valavani, M. Athans, and G. Stein, "Robustness of continuous-time adaptive control algorithms in the presence of unmodeled dynamics," *IEEE Trans. Automatic Control*, 30(9): 881-889, Sept 1985.

[55]   C. Cao, N. Havakimyan, "Design and analysis of a novel L1 adaptive control architecture, Part I: Control signal and symptotic stability.," *Proc. of American Control Conference*, 3397-3402, 2006.

[56]   C. Cao, N. Havakimyan, "Design and analysis of a novel L1 adaptive control architecture, Part II: Guaranteed transient performance." *Proc. of American Control Conference*, 3403-3408, 2006.

APPENDIX

A. CMG SINGULARITY PLOT MATLAB CODE

1. MATLAB Program Plot Singular Surfaces

```
% 3/4 CMG Singularity Surfaces        TA Sands
% This file plots points at the magnitude of angular momentum at singular points
% The points form a singular surface
clear all;close all;clc;

% Enter skew angles of each CMG:  skew1, skew2, skew3.
CMGskew=54.73;                              % ENTER SKEW ANGLE HERE
skew=CMGskew*pi/180;                        %convert degrees to radians for computer calculation
skew1=skew;skew2=skew;skew3=skew;     %Assigns values for each individual CMG skew angle

% Create gimbal axis unit vectors each CMG
g1=[-sin(skew1) 0 -cos(skew1)]';    g2=[0 -sin(skew2) -cos(skew2)]';    g3=[sin(skew3) 0 -cos(skew3)]';

% Create matrix of singular vectors called "[normal]" varying 2 angles from 0 to 2pi covering 3D space
normal=discretize_function; %Surface created

% 2 possible singular points exist for each (+ or -) Singular (normal) vectors
%Establish vector directions for normal vectors (+++ or ---)
e1=-1; e2=-1; e3=-1;  Hs_plus_plus_plus=momentum_function(g1,g2,g3,e1,e2,e3,normal);
%Hs_plus_plus_plus=[Hs_plus_plus_plus(1,1:1000);Hs_plus_plus_plus(2,1:1000);Hs_plus_plus_plus(3,1:
1000)]
%Establish vector directions for normal vectors (+-+)
e1=1;  e2=-1; e3=1;  Hs_plus_minus_plus=momentum_function(g1,g2,g3,e1,e2,e3,normal);
%Establish vector directions for normal vectors (+--)
e1=1;  e2=-1; e3=-1;  Hs_plus_minus_minus=momentum_function(g1,g2,g3,e1,e2,e3,normal);
%Establish vector directions for normal vectors (++-);
e1=1;  e2=1;  e3=-1;  Hs_plus_plus_minus=momentum_function(g1,g2,g3,e1,e2,e3,normal);

% Plot Singular Surfaces for all 4 cases:  +++ or ---, +-+, +--, and ++-
PlotSingularSurfaces_function(Hs_plus_plus_plus,Hs_plus_minus_plus,Hs_plus_minus_minus,Hs_plus_pl
us_minus,CMGskew);
```

2. Discretization Function Code

```
function [normal] = discretize;
angle1=linspace(-pi,pi/2,101);    angle2=linspace(0,2*pi,101);       index=0;
for i=1:length(angle1);
   for j=1:length(angle2);        index=index+1;
      normal(:,index)=[cos(angle1(i))*cos(angle2(j));  cos(angle1(i))*sin(angle2(j));  sin(angle1(i))];
   end
end
```

3. Momentum Function Code

```
function [Hs] = momentum(g1,g2,g3,e1,e2,e3,normal)

for i=1:length(normal);
   %Cross product gimbal 1,2,3 unit vectors and singular (normal) vectors
```

```
        g1Xnormal=cross(g1,normal(:,i));                                    g2Xnormal=cross(g2,normal(:,i));
    g3Xnormal=cross(g3,normal(:,i));
    % Calculate the angular momentum (Hxs,Hys,Hzs) at each singular point
    Hs(:,i)=e1*(cross(g1Xnormal,g1)/sqrt(g1Xnormal'*g1Xnormal))                              +
e2*(cross(g2Xnormal,g2)/sqrt(g2Xnormal'*g2Xnormal))                              +
e3*(cross(g3Xnormal,g3)/sqrt(g3Xnormal'*g3Xnormal));
end
```

4.   Plot Singular Surfaces Function Code

```
function PlotSingularSurfaces(Hs_plus_plus_plus,Hs_plus_minus_plus,Hs_plus_minus_minus,Hs_plus_plus_minus,CMGskew);
CMGskewAngle=['CMG skew angle = ',num2str(CMGskew),'^o'];
figure(1);subplot(2,2,1);plot3(Hs_plus_plus_plus(1,:),Hs_plus_plus_plus(2,:),Hs_plus_plus_plus(3,:),'o','MarkerSize',0.1);
    axis([-3,3,-3,3,-3,3]);xlabel('x');ylabel('y');zlabel('z');   title('Singular Vectors for +++');text(-2.5,2.5,3,CMGskewAngle);
    subplot(2,2,2);plot3(Hs_plus_minus_plus(1,:),Hs_plus_minus_plus(2,:),Hs_plus_minus_plus(3,:),'o','MarkerSize',0.1);
    axis([-3,3,-3,3,-3,3]);xlabel('x');ylabel('y');zlabel('z');   title('Singular Vectors for + - +');text(-2.5,2.5,3,CMGskewAngle);
    subplot(2,2,3);plot3(Hs_plus_minus_minus(1,:),Hs_plus_minus_minus(2,:),Hs_plus_minus_minus(3,:),'o','MarkerSize',0.1);
    axis([-3,3,-3,3,-3,3]);xlabel('x');ylabel('y');zlabel('z');   title('Singular Vectors for + - -');text(-2.5,2.5,3,CMGskewAngle);
    subplot(2,2,4);plot3(Hs_plus_plus_minus(1,:),Hs_plus_plus_minus(2,:),Hs_plus_plus_minus(3,:),'o','MarkerSize',0.1);
    axis([-3,3,-3,3,-3,3]);xlabel('x');ylabel('y');zlabel('z');   title('Singular Vectors for ++ -');text(-2.5,2.5,3,CMGskewAngle);
figure(2);plot3(Hs_plus_minus_plus(1,:),Hs_plus_minus_plus(2,:),Hs_plus_minus_plus(3,:),'o','MarkerSize',0.1);hold on
    plot3(Hs_plus_minus_minus(1,:),Hs_plus_minus_minus(2,:),Hs_plus_minus_minus(3,:),'ro','MarkerSize',0.1);
    plot3(Hs_plus_plus_minus(1,:),Hs_plus_plus_minus(2,:),Hs_plus_plus_minus(3,:),'mo','MarkerSize',0.1);hold off
    xlabel('x');ylabel('y');zlabel('z');title('Internal Singular Surfaces for 3/4 CMG Array','fontsize',16);axis([-3,3,-3,3,-3,3]);text(-
1,1,3,CMGskewAngle);
figure(3);plot3(Hs_plus_plus_plus(1,:),Hs_plus_plus_plus(2,:),Hs_plus_plus_plus(3,:),'co','MarkerSize',0.1);hold on
    plot3(Hs_plus_minus_plus(1,:),Hs_plus_minus_plus(2,:),Hs_plus_minus_plus(3,:),'o','MarkerSize',0.1);
    plot3(Hs_plus_minus_minus(1,:),Hs_plus_minus_minus(2,:),Hs_plus_minus_minus(3,:),'ro','MarkerSize',0.1);
    plot3(Hs_plus_plus_minus(1,:),Hs_plus_plus_minus(2,:),Hs_plus_plus_minus(3,:),'mo','MarkerSize',0.1);
    xlabel('x');ylabel('y');zlabel('z');title('Singular HyperSurface for 3/4 CMG Array','fontsize',16);
                                            axis([-3,3,-3,3,-3,3]);text(-1,1,3,CMGskewAngle);hold off
```

B.   SKEW ANGLE INTERATED SINGULAR SURFACES

Internal Singular Surfaces for 3/4 CMG Array

CMG skew angle = 0°

Singular HyperSurface for 3/4 CMG Array

CMG skew angle β = 0°

Momentum Envelope...note only 2D with β=0°

Internal Singular Surfaces for 3/4 CMG Array

CMG skew angle = 5°

Singular HyperSurface for 3/4 CMG Array
z-axis zoomed for visualization

CMG skew angle = 5°

Momentum Envelope grows with β>0°

112

Internal Singular Surfaces for 3/4 CMG Array

CMG skew angle = 10°

Singular HyperSurface for 3/4 CMG Array

CMG skew angle = 10°

113

Internal Singular Surfaces for 3/4 CMG Array

CMG skew angle = 15°

Singular HyperSurface for 3/4 CMG Array

CMG skew angle = 15°

Internal Singular Surfaces for 3/4 CMG Array

CMG skew angle = 20°

Singular HyperSurface for 3/4 CMG Array

CMG skew angle = 20°

115

Internal Singular Surfaces for 3/4 CMG Array

CMG skew angle = 25°

Singular HyperSurface for 3/4 CMG Array

CMG skew angle = 25°

116

Internal Singular Surfaces for 3/4 CMG Array

CMG skew angle = 30°

Singular HyperSurface for 3/4 CMG Array

CMG skew angle = 30°

Internal Singular Surfaces for 3/4 CMG Array

CMG skew angle = 35°

Singular HyperSurface for 3/4 CMG Array

CMG skew angle = 35°

Internal Singular Surfaces for 3/4 CMG Array

CMG skew angle = 40°

Singular HyperSurface for 3/4 CMG Array

CMG skew angle = 40°

Internal Singular Surfaces for 3/4 CMG Array

CMG skew angle = 45°

Singular HyperSurface for 3/4 CMG Array

CMG skew angle = 45°

120

Internal Singular Surfaces for 3/4 CMG Array

Singular HyperSurface for 3/4 CMG Array
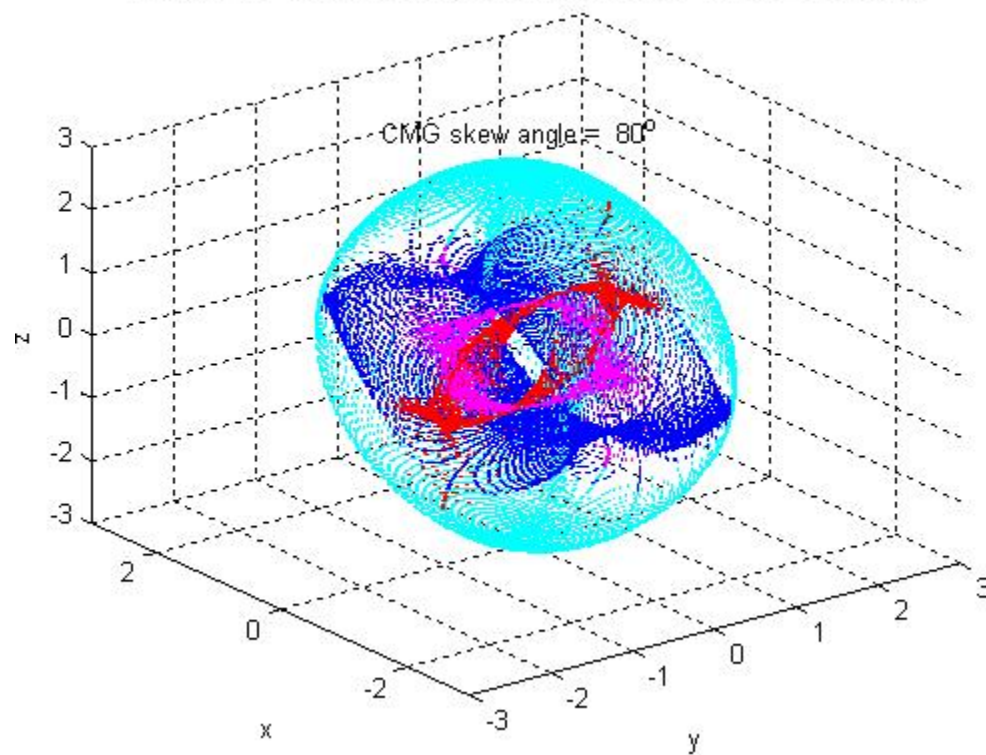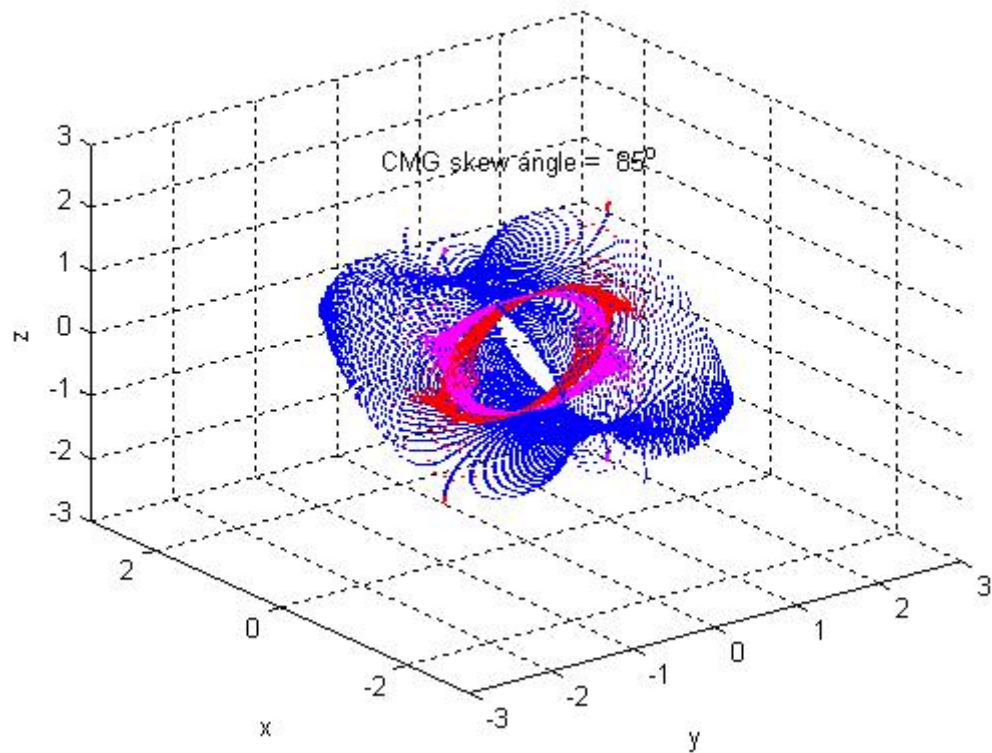

121

Internal Singular Surfaces for 3/4 CMG Array

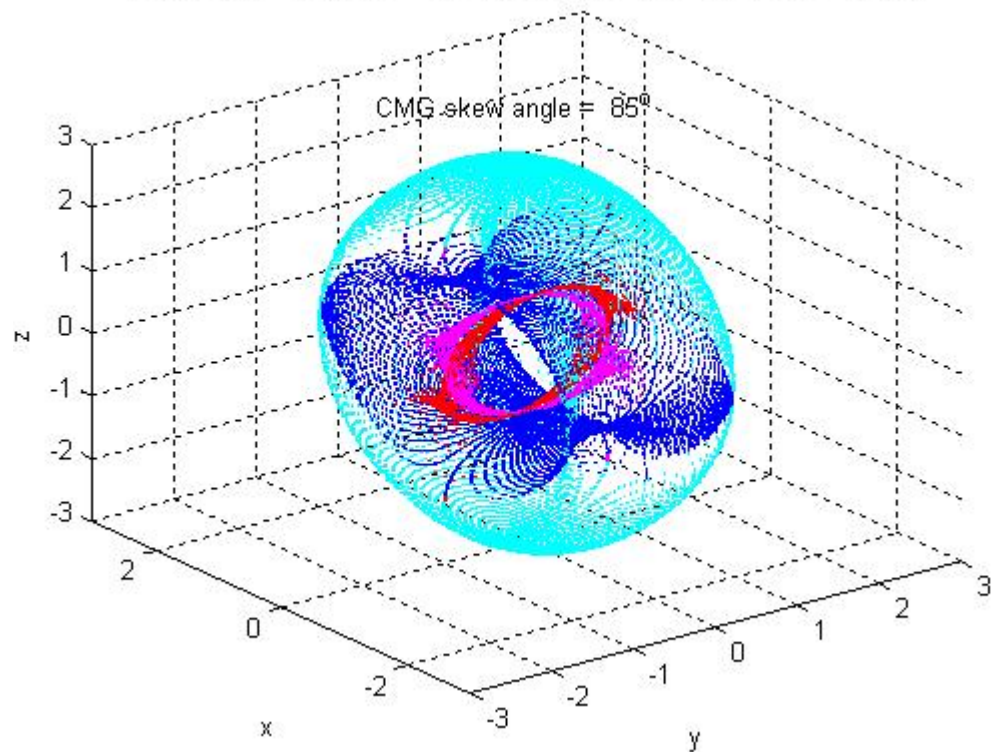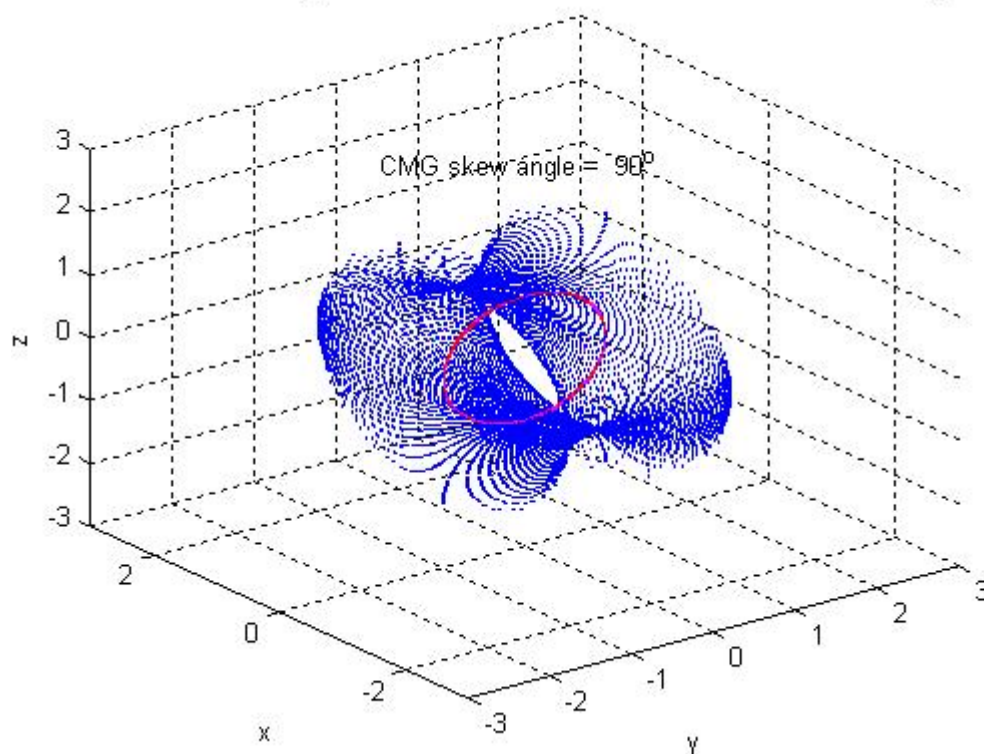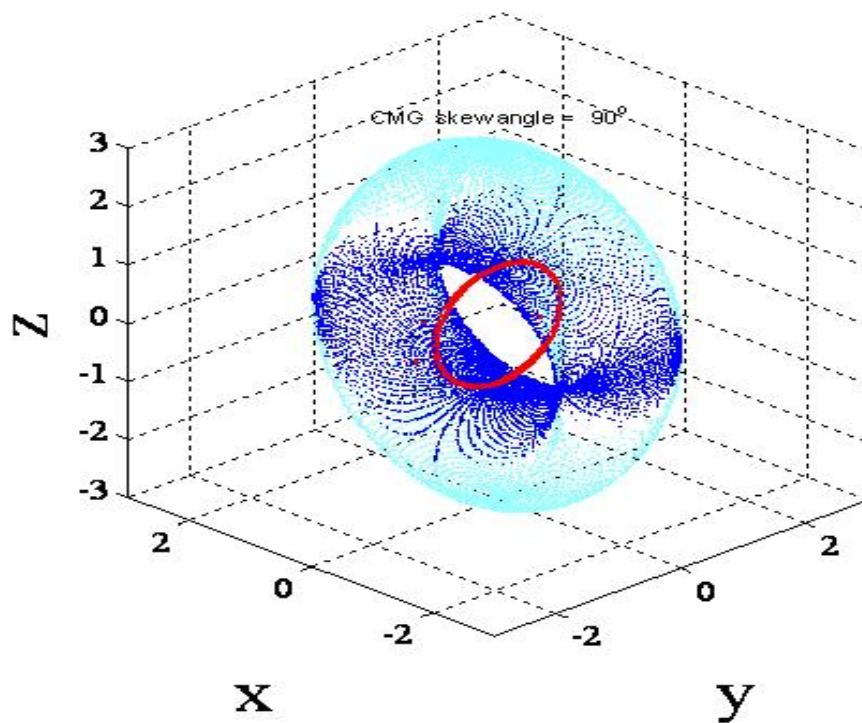CMG skew angle = 55°

Singular HyperSurface for 3/4 CMG Array

CMG skew angle = 55°

122

Internal Singular Surfaces for 3/4 CMG Array

CMG skew angle = 60°

Singular HyperSurface for 3/4 CMG Array

CMG skew angle = 60°

Internal Singular Surfaces for 3/4 CMG Array

CMG skew angle = 65°

Singular HyperSurface for 3/4 CMG Array

CMG skew angle = 65°

Internal Singular Surfaces for 3/4 CMG Array

CMG skew angle = 70°

Singular HyperSurface for 3/4 CMG Array

CMG skew angle = 70°

125

Internal Singular Surfaces for 3/4 CMG Array

CMG skew angle = 75°

Singular HyperSurface for 3/4 CMG Array

CMG skew angle = 75°

Internal Singular Surfaces for 3/4 CMG Array

CMG skew angle = 80°

Singular HyperSurface for 3/4 CMG Array

CMG skew angle = 80°

127

Internal Singular Surfaces for 3/4 CMG Array

CMG skew angle = 85°

Singular HyperSurface for 3/4 CMG Array

CMG skew angle = 85°

Internal Singular Surfaces for 3/4 CMG Array

CMG skew angle = 90°

Singular HyperSurface for 3/4 CMG Array

CMG skew angle = 90°

129

C. ADAPTIVE FEEDFORWARD CONTROL

Slotine's Regression matrix of "knowns" implemented in the inertial frame to be compared with Fossen's improvement in equation 32.

$\Phi(1,1) = J_{xx}$ Components of $[\Phi]\{\theta\}(1,1)$

$$\ddot{\phi} - \ddot{\psi}\sin\theta + \left(\cos\phi\dot{\phi}\tan\theta + \sin\phi\sec^2\theta\dot{\theta}\right) + \left[-\frac{\sin\theta(\cos\theta\cos\phi\dot{\phi} + \sin\phi\sin\theta\dot{\theta})\cos\phi}{\cos^2\theta(\sin\theta\sin\phi + \cos^2\phi)} + ...\right]\dot{\theta}$$

$$\left[... + (\sin\phi\sin\dot{\phi}\tan\theta + \cos\phi\sec^2\theta) - \frac{\sin\theta(-\cos\theta\sin\phi\dot{\phi} + \cos\phi\sin\theta\dot{\theta})\sin\phi}{\cos^2\theta(\sin\theta\sin\phi + \cos^2\phi)}\right]\dot{\theta}$$

$$+ \left[\frac{(\cos\phi\dot{\phi}\tan\theta + \sin\phi\sec^2\theta\dot{\theta})\sin\theta\cos\theta}{\sin\theta\sin\phi + \cos^2\phi} - \frac{\sin^2\theta(\cos\theta\cos\phi\dot{\phi} + \sin\phi\sin\theta\dot{\theta})}{\cos\theta(\sin\theta\sin\phi + \cos^2\phi)} + ...\right]\dot{\psi}$$

$$\left[... - \frac{(\sin\phi\dot{\phi}\tan\theta + \cos\phi\sec^2\theta)\cos\theta\cos\phi}{\sin\theta\sin\phi + \cos^2\phi} - \frac{\sin\theta(-\cos\theta\sin\phi\dot{\phi} + \cos\phi\sin\theta\dot{\theta})\cos\phi}{\cos\theta\left(\sin\theta\sin\phi + \cos^2\phi\right)}\right]\dot{\psi}$$

$\Phi(1,2) = J_{xy}$ Components of $[\Phi]\{\theta\}(1,1)$

$$\frac{\cos\phi\ddot{\theta} - \sin\theta\cos\theta\ddot{\psi}}{\sin\theta\sin\phi + \cos^2\phi} + \left[\frac{\cos\phi\sin\phi\dot{\phi} + \tan\theta(\cos\theta\cos\phi\dot{\phi} + \sin\phi\sin\theta\dot{\theta})}{(\sin\theta\sin\phi + \cos^2\phi)^2}\cos\phi + ...\right]\dot{\theta}$$

$$\left[... - \frac{\cos\phi\cos\theta\dot{\theta} - \tan\theta(-\cos\theta\sin\phi\dot{\phi} + \cos\phi\sin\theta\dot{\theta})}{\left(\sin\theta\sin\phi + \cos^2\phi\right)^2}\sin\phi\right]\dot{\theta}$$

$$+ \left[-\frac{\cos\phi\sin\phi\dot{\phi} + \tan\theta(\cos\theta\cos\phi\dot{\phi} + \sin\phi\sin\theta\dot{\theta})}{\left(\sin\theta\sin\phi + \cos^2\phi\right)^2}\sin\theta\cos\theta + ...\right]\dot{\psi}$$

$$\left[... + \frac{\cos\phi\cos\theta\dot{\theta} - \tan\theta(-\cos\theta\sin\phi\dot{\phi} + \cos\phi\sin\theta\dot{\theta})}{\left(\sin\theta\sin\phi + \cos^2\phi\right)^2}\cos\theta\cos\phi\right]\dot{\psi}$$

$$\Phi(1,3) = J_{xz} \text{ Components of } [\Phi]\{\theta\}(1,1)$$

$$\frac{\cos\theta\cos\phi\ddot{\psi}}{\sin\theta\sin\phi+\cos^2\phi} + \left[-\frac{\sin^2\phi\dot{\phi}\cos\phi+\dfrac{\cos^2\phi}{\cos\theta}(\cos\theta\cos\phi\dot{\phi}+\sin\phi\sin\theta\dot{\theta})}{(\sin\theta\sin\phi+\cos^2\phi)^2} + ... \right]\dot{\theta}$$

$$\left[+\frac{-\sin^2\phi\cos\theta\dot{\theta}+\dfrac{\sin\phi\cos\phi}{\cos\theta}(-\cos\theta\sin\phi\dot{\phi}+\cos\phi\sin\theta\dot{\theta})}{(\sin\theta\sin\phi+\cos^2\phi)^2} \right]\dot{\theta}$$

$$+\left[\frac{\sin^2\phi\dot{\phi}\sin\theta\cos\theta+\cos\phi\sin\theta(\cos\theta\cos\phi\dot{\phi}+\sin\phi\sin\theta\dot{\theta})}{\left(\sin\theta\sin\phi+\cos^2\phi\right)^2} + ... \right]\dot{\psi}$$

$$\left[...+\frac{-\sin\phi\cos^2\theta\cos\phi\dot{\theta}-\cos^2\phi(-\cos\theta\sin\phi\dot{\phi}+\cos\phi\sin\theta\dot{\theta})}{\left(\sin\theta\sin\phi+\cos^2\phi\right)^2} \right]\dot{\psi}$$

$$\Phi(1,4) = J_{yy} \text{ Components of } [\Phi]\{\theta\}(1,1) = 0$$

$$\Phi(1,5) = J_{yz} \text{ Components of } [\Phi]\{\theta\}(1,1) = 0$$

$$\Phi(1,6) = J_{zz} \text{ Components of } [\Phi]\{\theta\}(1,1) = 0$$

$$\Phi(1,7) = H_x \text{ Components of } [\Phi]\{\theta\}(1,1) = 0$$

$$\Phi(1,8) = H_y \text{ Components of } [\Phi]\{\theta\}(1,1) = \frac{\sin\phi\dot{\theta}-\cos\theta\cos\phi\dot{\psi}}{\sin\theta\sin\phi+\cos^2\phi}$$

$$\Phi(1,9) = H_z \text{ Components of } [\Phi]\{\theta\}(1,1) = \frac{\cos\phi\dot{\theta}+\sin\theta\cos\theta\dot{\psi}}{\sin\theta\sin\phi+\cos^2\phi}$$

$$\Phi(2,1) = J_{xx} \text{ Components of } [\Phi]\{\theta\}(2,1) = 0$$

$\Phi(2,2) = J_{xy}$ Components of $[\Phi]\{\theta\}(2,1)$

$$\frac{\cos\phi\ddot{\phi} - \cos\phi\sin\theta\ddot{\psi}}{\sin\theta\sin\phi + \cos^2\phi} + \left[\frac{(-\cos^2\phi - \cos^2\phi\sin\theta)(\cos\phi\dot{\phi}\tan\theta + \sin\phi\sec^2\theta\dot{\theta})}{\cos^2\theta(\sin\theta\sin\phi + \cos^2\phi)^2} + ...\right]\dot{\theta}$$

$$\left[... + \frac{\cos\phi\sin\phi(\sin\phi\dot{\phi}\tan\theta + \cos\phi\sec^2\theta)}{\cos^2\theta(\sin\theta\sin\phi + \cos^2\phi)^2} - \frac{\cos\phi\sin\theta\sin\phi(-\cos\theta\sin\phi\dot{\phi} + \cos\phi\sin\theta\dot{\theta})}{\cos^2\theta(\sin\theta\sin\phi + \cos^2\phi)^2}\right]\dot{\theta}$$

$$+\left[\frac{-\cos\phi\sin\theta\cos\theta - \cos\phi\sin^2\theta\cos\theta(\cos\phi\dot{\phi}\tan\theta + \sin\phi\sec^2\theta\dot{\theta})}{\cos^2\theta(\sin\theta\sin\phi + \cos^2\phi)^2} + ...\right]\dot{\psi}$$

$$\left[... + \frac{-\cos^2\phi\cos\theta(-\sin\phi\dot{\phi}\tan\theta + \cos\phi\sec^2\theta) - \cos^2\phi\cos\theta\sin\theta(-\cos\theta\sin\phi\dot{\phi} + \cos\phi\sin\theta\dot{\theta})}{\cos^2\theta(\sin\theta\sin\phi + \cos^2\phi)^2}\right]\dot{\psi}$$

$\Phi(2,3) = J_{xz}$ Components of $[\Phi]\{\theta\}(2,1)$

$$\frac{-\sin\phi\ddot{\phi} - \sin\phi\sin\theta\ddot{\psi}}{\sin\theta\sin\phi + \cos^2\phi} + \left[\frac{(\sin^2\phi\dot{\phi}\cos\phi - \sin\phi\sin\theta\cos\phi)(\cos\phi\dot{\phi}\tan\theta + \sin\phi\sec^2\theta\dot{\theta}) + ...}{\cos^2\theta(\sin\theta\sin\phi + \cos^2\phi)^2}\right]\dot{\theta}$$

$$\left[\frac{... - \sin^2\phi(\sin\phi\dot{\phi}\tan\theta + \cos\phi\sec^2\theta) + \sin^2\phi\sin\theta(-\cos\theta\sin\phi\dot{\phi} + \cos\phi\sin\theta\dot{\theta})}{\cos^2\theta(\sin\theta\sin\phi + \cos^2\phi)^2}\right]\dot{\theta}$$

$$+\left[\frac{(-\sin\phi\sin\theta\cos\theta + \sin\phi\sin^2\theta\cos\theta)(\cos\phi\dot{\phi}\tan\theta + \sin\phi\sec^2\theta\dot{\theta}) + ...}{\cos^2\theta(\sin\theta\sin\phi + \cos^2\phi)^2}\right]\dot{\psi}$$

$$\left[\frac{... + \sin\phi\cos\theta\cos\phi(-\sin\phi\dot{\phi}\tan\theta + \cos\phi\sec^2\theta) + \sin\phi\sin\theta\cos\theta\cos\phi(-\cos\theta\sin\phi\dot{\phi} + \cos\phi\sin\theta\dot{\theta})}{\cos^2\theta(\sin\theta\sin\phi + \cos^2\phi)^2}\right]\dot{\psi}$$

$\Phi(2,4) = J_{yy}$ Components of $[\Phi]\{\theta\}(2,1)$

$$\frac{\cos^2\phi\ddot{\theta} + \cos\phi\sin\theta\ddot{\psi}}{\sin\theta\sin\phi + \cos^2\phi} + \left[\frac{(\cos^3\phi\sin\phi\dot{\phi} + \cos^2\phi\sin\theta\cos\theta)(\cos\phi\dot{\phi}\tan\theta + \sin\phi\sec^2\theta\dot{\theta}) + ...}{\cos^2\theta(\sin\theta\sin\phi + \cos^2\phi)^3}\right]\dot{\theta}$$

$$\left[\frac{... - \cos^2\phi\cos\theta\dot{\theta}\sin\phi + \cos\phi\sin\theta\cos\theta\sin\phi(-\cos\theta\sin\phi\dot{\phi} + \cos\phi\sin\theta\dot{\theta})}{\cos^2\theta(\sin\theta\sin\phi + \cos^2\phi)^3}\right]\dot{\theta}$$

132

$$+\left[\frac{\cos^2\phi\sin\phi\dot\phi\sin\theta\cos\theta+\cos\phi\sin^2\theta\cos^2\theta(\cos\phi\dot\phi\tan\theta+\sin\phi\sec^2\theta\dot\theta)+...}{\cos^2\theta(\sin\theta\sin\phi+\cos^2\phi)^3}\right]\dot\psi$$

$$\left[\frac{...+\cos^3\phi\cos^2\theta\dot\theta-\cos^2\phi\sin\theta\cos^2\theta(-\cos\theta\sin\phi\dot\phi+\cos\phi\sin\theta\dot\theta)}{\cos^2\theta(\sin\theta\sin\phi+\cos^2\phi)^3}\right]\dot\psi$$

$\Phi(2,5)=J_{yz}$ Components of $[\Phi]\{\theta\}(2,1)$

$$\frac{-2\sin\phi\cos\phi\ddot\theta+(-\sin\phi\sin\theta\cos\theta+\cos^3\phi\cos\theta)\ddot\psi}{\sin\theta\sin\phi+\cos^2\phi}+\left[\frac{-\sin^2\phi\cos^2\phi\dot\phi-\cos^2\phi\cos^2\phi\dot\phi+...}{\cos^2\theta(\sin\theta\sin\phi+\cos^2\phi)^3}\right]\dot\theta$$

$$\left[\frac{...+(-\sin\phi\sin\theta\cos\theta\cos\phi+\cos^3\phi\cos\theta)(\cos\phi\dot\phi\tan\theta+\sin\phi\sec^2\theta\dot\theta)\sin^2\phi\cos\phi\cos\theta\dot\theta+\cos\phi\cos\theta\dot\theta\sin\phi+...}{\cos^2\theta(\sin\theta\sin\phi+\cos^2\phi)^3}\right]\dot\theta$$

$$\left[\frac{...+(-\sin^2\phi\sin\theta\cos\theta+\cos^3\phi\cos\theta\sin\phi)(-\cos\theta\sin\phi\dot\phi+\cos\phi\sin\theta\dot\theta)}{\cos^2\theta(\sin\theta\sin\phi+\cos^2\phi)^3}\right]\dot\theta$$

$$+\left[\frac{-\sin^2\phi\cos\phi\dot\phi\sin\theta\cos\theta-\cos\phi\sin\phi\dot\phi\sin\theta\cos\theta+...}{\cos^2\theta(\sin\theta\sin\phi+\cos^2\phi)}\right]\dot\psi$$

$$\left[\frac{...-(\sin\phi\sin^2\theta\cos^2\theta+\cos\phi\cos^2\theta\cos\phi\sin\theta)(\cos\phi\dot\phi\tan\theta+\sin\phi\sec^2\theta\dot\theta)-\sin\phi\cos^2\phi\cos^2\theta\dot\theta+...}{\cos^2\theta(\sin\theta\sin\phi+\cos^2\phi)}\right]\dot\psi$$

$$\left[\frac{...+(-\sin\phi\sin\theta\cos\theta+\cos^2\phi\cos\theta)(-\cos\theta\sin\phi\dot\phi+\cos\phi\sin\theta\dot\theta)(\cos\theta\cos\phi)}{\cos^2\theta(\sin\theta\sin\phi+\cos^2\phi)}\right]\dot\psi$$

$\Phi(2,6)=J_{zz}$ Components of $[\Phi]\{\theta\}(2,1)$

$$\frac{\sin^2\phi\ddot\theta-\sin\phi\cos\theta\cos\phi\ddot\psi}{\sin\theta\sin\phi+\cos^2\phi}+\left[\frac{(\sin^3\phi\dot\phi\cos\phi-\sin\phi\cos\theta\cos^2\phi)(\cos\phi\dot\phi\tan\theta+\sin\phi\sec^2\theta\dot\theta)+...}{\cos^2\theta(\sin\theta\sin\phi+\cos^2\phi)^3}\right]\dot\theta$$

$$\left[\frac{...-\sin^3\phi\cos\theta\dot\theta-\sin^2\phi\cos\theta\cos\phi(-\cos\theta\sin\phi\dot\phi+\cos\phi\sin\theta\dot\theta)}{\cos^2\theta(\sin\theta\sin\phi+\cos^2\phi)^3}\right]\dot\theta$$

$$+\left[\frac{\sin^3\phi\dot\phi\cos\phi-\sin\theta\cos\theta\cos^2\phi(\cos\phi\dot\phi\tan\theta+\sin\phi\sec^2\theta\dot\theta)+...}{\cos^2\theta(\sin\theta\sin\phi+\cos^2\phi)^3}\right]\dot\psi$$

$$\left[\dfrac{\ldots-\sin^2\phi\cos^2\theta\dot\theta\cos\phi+(\sin\phi\cos^2\theta\cos^2\phi)(-\cos\theta\sin\phi\dot\phi+\cos\phi\sin\theta\dot\theta)}{\cos^2\theta(\sin\theta\sin\phi+\cos^2\phi)^3}\right]\dot\psi$$

$\underline{\Phi(2,7)=H_x}$ Components of $[\Phi]\{\theta\}(2,1)=\dfrac{\sin\phi\sin\theta\cos\theta-\cos^2\phi\cos\theta\dot\psi}{\left(\sin\theta\sin\phi+\cos^2\phi\right)^2}$

$\underline{\Phi(2,8)=H_y}$ Components of $[\Phi]\{\theta\}(2,1)=\dfrac{-\sin\phi\dot\phi+\sin\phi\cos\theta\dot\psi}{\sin\theta\sin\phi+\cos^2\phi}$

$\underline{\Phi(2,9)=H_z}$ Components of $[\Phi]\{\theta\}(2,1)=\dfrac{-\cos\phi\dot\phi+\cos\phi\sin\theta\dot\psi}{\sin\theta\sin\phi+\cos^2\phi}$

$\underline{\Phi(3,1)=J_{xx}}$ Components of $[\Phi]\{\theta\}(3,1)$

$$-\sin\phi\ddot\phi-\sin^2\theta\ddot\psi+\left[\dfrac{\sin\theta(\cos\phi\dot\phi\tan\theta+\sin\phi\sec^2\theta\dot\theta)\sin\phi\dot\phi\cos\phi+\sin\theta(\cos\theta\cos\phi\dot\phi+\sin\phi\sin\theta\dot\theta)\cos\phi+\ldots}{\cos^2\theta(\sin\theta\sin\phi+\cos^2\phi)}\right]\dot\theta$$

$$\left[\dfrac{\ldots+\sin\theta(-\sin\phi\dot\phi\tan\theta+\cos\phi\sec^2\theta)\cos\theta\dot\theta\sin\phi+\sin\theta(-\cos\phi\dot\phi+\cos\phi\sin\theta\dot\theta)}{\cos^2\theta(\sin\theta\sin\phi+\cos^2\phi)}\right]\dot\theta$$

$$+\left[\dfrac{\sin\theta(\cos\phi\dot\phi\tan\theta+\sin\phi\sec^2\theta\dot\theta)\sin\theta\cos\theta-\sin\theta(\cos\theta\cos\phi\dot\phi+\sin\phi\sin\theta\dot\theta)\sin\theta\cos\theta+\ldots}{\cos^2\theta(\sin\theta\sin\phi+\cos^2\phi)}\right]\dot\psi$$

$$\left[\dfrac{\sin\theta(-\sin\phi\dot\phi\tan\theta+\cos\phi\sec^2\theta)\cos^2\theta\dot\theta\cos\phi+\sin^2\theta(-\cos\phi\dot\phi+\cos\theta\dot\theta)}{\cos^2\theta(\sin\theta\sin\phi+\cos^2\phi)}\right]\dot\psi$$

$\underline{\Phi(3,2)=J_{xy}}$ Components of $[\Phi]\{\theta\}(3,1)$

$$\dfrac{\sin\theta\cos\theta\ddot\phi-\sin\theta\cos\phi\ddot\theta+(\cancel{\sin^2\theta\cos\theta}-\cancel{\sin^2\theta\cos\theta})\ddot\psi}{\sin\theta\sin\phi+\cos^2\phi}+\ldots$$

$$+\left[-\dfrac{\sin\theta\cos\theta(\cos\phi\dot\phi\tan\theta+\sin\phi\sec^2\theta\dot\theta)\sin\phi\dot\phi\cos\phi-\sin\theta\cos^2\phi\sin\phi\dot\phi+\ldots}{\cos^2\theta(\sin\theta\sin\phi+\cos^2\phi)^2}\right]\dot\theta$$

$$\left[\dfrac{\ldots+(-\cancel{\sin^2\theta\cos\theta}+\cancel{\sin^2\theta\cos\theta})\cos\theta\cos\phi\dot\phi+\sin\phi\sin\theta\dot\theta\cos\phi+\ldots}{\cos^2\theta(\sin\theta\sin\phi+\cos^2\phi)^2}\right]\dot\theta$$

$$\left[\frac{...+\sin^2\theta\cos\theta(-\sin\phi\dot\phi\tan\theta+\cos\phi\sec^2\theta)\dot\theta-\sin\theta\cos\phi\cos\theta\dot\theta+...}{\cos^2\theta(\sin\theta\sin\phi+\cos^2\phi)^2}\right]\dot\theta$$

$$\left[\frac{...+(-\sin\theta\cos\theta(-\sin\phi\dot\phi\tan\theta+\cos\phi\sec^2\theta)-\sin\theta\cos\phi)\cos\theta\dot\theta\sin\phi+...}{\cos^2\theta(\sin\theta\sin\phi+\cos^2\phi)^2}\right]\dot\theta$$

$$\left[\frac{...+(-\cancel{\sin^2\theta\cos\theta}+\cancel{\sin^2\theta\cos\theta})(\cos\phi\dot\phi+\cos\phi\sin\theta\dot\theta)}{\cos^2\theta(\sin\theta\sin\phi+\cos^2\phi)^2}\right]\dot\theta$$

$$+\left[\frac{-\sin^2\theta\cos^2\theta(\cos\phi\dot\phi\tan\theta+\sin\phi\sec^2\theta\dot\theta)-\sin^2\theta\cos\phi\sin\phi\dot\phi\cos\theta+...}{\cos^2\theta(\sin\theta\sin\phi+\cos^2\phi)^2}\right]\dot\psi$$

$$\left[\frac{(\cancel{\sin^2\theta\cos\theta}-\cancel{\sin^2\theta\cos\theta})(\cos\theta\cos\phi\dot\phi+\sin\phi\sin\theta\dot\theta)\sin\theta\cos\theta}{\cos^2\theta(\sin\theta\sin\phi+\cos^2\phi)^2}\right]\dot\psi$$

$$\left[\frac{...-\sin\theta\cos^2\theta\dot\theta(-\sin\phi\dot\phi\tan\theta+\cos\phi\sec^2\theta)-\sin\theta\cos\phi\cos\theta\dot\theta}{\cos^2\theta(\sin\theta\sin\phi+\cos^2\phi)^2}\right]\dot\psi$$

$$\left[\frac{(-\cancel{\sin^2\theta\cos\theta}+\cancel{\sin^2\theta\cos\theta})(-\cos\theta\sin\phi\dot\phi+\cos\phi\sin\theta\dot\theta)}{\cos^2\theta(\sin\theta\sin\phi+\cos^2\phi)^2}\right]\dot\psi$$

$\Phi(3,3)=J_{xz}$ Components of $[\Phi]\{\theta\}(3,1)$

$$\frac{\cos\theta\cos\phi\ddot\phi-\sin\theta\sin\phi\ddot\theta+(-\cos\theta\cos\phi\sin\theta-\sin\phi\cos\theta\cos\phi)\ddot\psi}{\sin\theta\sin\phi+\cos^2\phi}+...$$

$$+\left[\frac{-\cos\theta\cos^2\phi(\cos\phi\dot\phi\tan\theta+\sin\phi\sec^2\theta\dot\theta)\sin\phi\dot\phi\cos\phi-\cos\theta\cos^3\phi\sin\phi\dot\phi+\sin\theta\sin^2\phi\dot\phi\cos\phi+...}{\cos^2\theta(\sin\theta\sin\phi+\cos^2\phi)^2}\right]\dot\theta$$

$$\left[\frac{...+(-\cancel{\cos\theta\cos^2\phi\sin\theta}+\cancel{\sin\theta\cos\theta\cos^2\phi})\cos\theta\cos\phi\dot\phi+\sin\phi\sin\theta\dot\theta+...}{\cos^2\theta(\sin\theta\sin\phi+\cos^2\phi)^2}\right]\dot\theta$$

$$\left[\frac{...+\cos^2\theta\cos\phi\dot\theta\sin\phi(-\sin\phi\dot\phi\tan\theta+\cos\phi\sec^2\theta)\dot\theta-\sin\theta\cos\phi\cos\theta\dot\theta\sin\phi+...}{\cos^2\theta(\sin\theta\sin\phi+\cos^2\phi)^2}\right]\dot\theta$$

$$\left[\frac{...+(-\cancel{\cos\theta\cos\phi\sin\theta}+\cancel{\sin\theta\cos\theta\cos\phi})(-\cos\theta\sin\phi\dot\phi+\cos\phi\sin\theta\dot\theta)}{\cos^2\theta(\sin\theta\sin\phi+\cos^2\phi)^2}\right]\dot\theta$$

$$+\left[\frac{-\cos^3\theta\cos^2\phi(-\sin\phi\dot\phi\tan\theta+\cos\phi\sec^2\theta)-\sin\theta\cos^2\theta\dot\theta\cos\phi+...}{\cos^2\theta(\sin\theta\sin\phi+\cos^2\phi)^2}\right]\dot\psi$$

$$\left[\frac{(-\cos\theta\cos\phi\sin\theta-\sin\theta\cos\theta\cos\phi)(-\cos\phi\sin\phi\dot\phi+\cos\phi\sin\theta\dot\theta)}{\cos^2\theta(\sin\theta\sin\phi+\cos^2\phi)^2}\right]\dot\psi$$

$\Phi(3,4)=J_{yy}$ Components of $[\Phi]\{\theta\}(3,1)$

$$\frac{\sin\theta\cos\theta\cos\phi\ddot\theta+\dfrac{\sin^2\theta\cos^2\theta}{\sin\theta\sin\phi+\cos^2\phi}\ddot\psi}{\sin\theta\sin\phi+\cos^2\phi}+...$$

$$+\left[\frac{-\sin\theta\cos\theta\sin\phi\dot\phi\cos\phi-\sin^2\theta\cos^2\theta(\cos\theta\cos\phi\dot\phi+\sin\phi\sin\theta\dot\theta)\cos\phi+\sin\theta\cos^2\theta\cos\phi\dot\theta\sin\phi+...}{\cos^2\theta(\sin\theta\sin\phi+\cos^2\phi)^3}\right]\dot\theta$$

$$\left[\frac{...-\sin\theta\sin\phi\sin\theta\cos\theta(-\cos\theta\sin\phi\dot\phi+\cos\phi\sin\theta\dot\theta)}{\cos^2\theta(\sin\theta\sin\phi+\cos^2\phi)^3}\right]\dot\theta$$

$$+\left[\frac{\sin^2\theta\cos^2\theta\cos\phi\sin\phi\dot\phi-\sin^3\theta\cos^3\theta(\cos\theta\cos\phi\dot\phi+\sin\phi\sin\theta\dot\theta)+\sin\theta\cos^3\theta\cos^2\phi\dot\theta+...}{\cos^2\theta(\sin\theta\sin\phi+\cos^2\phi)^3}\right]\dot\psi$$

$$\left[\frac{\sin^2\theta\cos^2\theta(-\cos\theta\sin\phi\dot\phi+\cos\phi\sin\theta\dot\theta)}{\cos^2\theta(\sin\theta\sin\phi+\cos^2\phi)^3}\right]\dot\psi$$

$\Phi(3,5)=J_{yz}$ Components of $[\Phi]\{\theta\}(3,1)$

$$\frac{(\cos\theta\cos^2\phi-\sin\theta\cos\theta)\ddot\theta+(\cos^2\theta\cos\phi\sin\theta+\sin\theta\cos^2\theta\cos\phi)\ddot\psi}{\sin\theta\sin\phi+\cos^2\phi}+...$$

$$+\left[\frac{\cos\theta\cos^3\phi\sin\phi\dot\phi-\sin\theta\cos\theta\sin\phi\dot\phi\cos\phi-\cos^2\theta\cos^2\phi\sin\theta(\cos\theta\cos\phi\dot\phi+\sin\phi\sin\theta\dot\theta)+...}{\cos^2\theta(\sin\theta\sin\phi+\cos^2\phi)^3}\right]\dot\theta$$

$$\left[\frac{-\sin\theta\cos^2\theta\cos^2\phi(\cos\theta\cos\phi\dot\phi+\sin\phi\sin\theta\dot\theta)+\cos^2\theta\cos^2\phi\dot\theta\sin\phi-\sin\theta\cos^2\theta\sin^2\phi\dot\theta+...}{\cos^2\theta(\sin\theta\sin\phi+\cos^2\phi)^3}\right]\dot\theta$$

$$\left[\frac{...+(\cos^2\theta\cos^2\phi\sin\theta+\sin\theta\cos^2\theta\cos^2\phi)(-\cos\theta\sin\phi\dot\phi+\cos\phi\sin\theta\dot\theta)}{\cos^2\theta(\sin\theta\sin\phi+\cos^2\phi)^3}\right]\dot\theta$$

136

$$+\left[\frac{\cos^2\theta\cos\phi\sin\phi\dot\phi-\sin^2\theta\cos^2\theta\sin^2\phi\dot\phi-\cos^3\theta\cos\phi\sin^2\theta(\cos\theta\cos\phi\dot\phi+\sin\phi\sin\theta\dot\theta)+...}{\cos^2\theta(\sin\theta\sin\phi+\cos^2\phi)^3}\right]\dot\psi$$

$$\left[\frac{...+\cos^3\theta\cos^3\phi\dot\theta+\cos^2\theta\cos\phi\sin\theta(-\cos\theta\sin\phi\dot\phi+\cos\phi\sin\theta\dot\theta)}{\cos^2\theta(\sin\theta\sin\phi+\cos^2\phi)^3}\right]\dot\psi$$

$\Phi(3,6)=J_{zz}$ Components of $[\Phi]\{\theta\}(3,1)$

$$\frac{\cos\theta\cos\phi\sin\phi\ddot\theta+\cos^2\theta\cos^2\phi\ddot\psi}{\sin\theta\sin\phi+\cos^2\phi}+...$$

$$+\left[\frac{\cos\theta\cos^2\phi\sin^2\phi\dot\phi-\cos^2\theta\cos^3\phi(\cos\theta\cos\phi\dot\phi+\sin\phi\sin\theta\dot\theta)-\cos^2\theta\cos\phi\sin^2\phi\dot\theta+...}{\cos^2\theta(\sin\theta\sin\phi+\cos^2\phi)^3}\right]\dot\theta$$

$$\left[\frac{...+\cos^2\theta\cos^2\phi(-\cos\theta\sin\phi\dot\phi+\cos\phi\sin\theta\dot\theta)}{\cos^2\theta(\sin\theta\sin\phi+\cos^2\phi)^3}\right]\dot\theta$$

$$+\left[\frac{-\cos^2\theta\cos\phi\sin^2\phi\dot\phi\sin\theta-\cos^3\theta\cos^2\phi\sin\theta(\cos\theta\cos\phi\dot\phi+\sin\phi\sin\theta\dot\theta)+...}{\cos^2\theta(\sin\theta\sin\phi+\cos^2\phi)^3}\right]\dot\psi$$

$$\left[\frac{...+\cos^3\theta\cos^2\phi\sin\phi\dot\theta+\cos^2\theta\cos^2\phi(-\cos\theta\sin\phi\dot\phi+\cos\phi\sin\theta\dot\theta)}{\cos^2\theta(\sin\theta\sin\phi+\cos^2\phi)^3}\right]\dot\psi$$

$\Phi(3,7)=H_x$ Components of $[\Phi]\{\theta\}(3,1)$

$$\frac{-\cos\theta\cos^2\phi-\sin\theta\cos\theta\sin\phi\dot\theta+(\cos\theta\cos\phi\sin\theta\cos\theta+\sin\theta\cos^2\theta\cos\phi)\dot\psi}{(\sin\theta\sin\phi+\cos^2\phi)^2}$$

$\Phi(3,8)=H_y$ Components of $[\Phi]\{\theta\}(3,1)$

$$\frac{\cos\theta\cos\phi\dot\phi-\sin\theta\dot\theta+(-\cos\theta\cos\phi\sin\theta+\sin\theta)\dot\psi}{\sin\theta\sin\phi+\cos^2\phi}$$

$\Phi(3,9) = H_z$ Components of $[\Phi]\{\theta\}(3,1)$

$$\frac{-\sin\theta\cos\theta\dot{\phi} - \sin\theta\cos\theta\dot{\theta} + (\sin^2\theta\cos\theta + \sin^2\theta\cos\theta)\dot{\psi}}{\sin\theta\sin\phi + \cos^2\phi}$$

INITIAL DISTRIBUTION LIST

1.   Defense Technical Information Center
        Ft. Belvoir, Virginia

2.   Dudley Knox Library
        Naval Postgraduate School
        Monterey, California

3.   Spacecraft Research and Design Center, Mail Code ME/Ag
        Naval Postgraduate School
        Monterey, California